National Library of Canada

Bibliothèque nationale du Canada

Canadian Theses Service

Service des thèses canadiennes

Ottawa, Canada
K1A 0N4

NOTICE

The quality of this microform is heavily dependent upon the quality of the original thesis submitted for microfilming. Every effort has been made to ensure the highest quality of reproduction possible.

If pages are missing, contact the university which granted the degree.

Some pages may have indistinct print especially if the original pages were typed with a poor typewriter ribbon or if the university sent us an inferior photocopy.

Reproduction in full or in part of this microform is governed by the Canadian Copyright Act, R.S.C. 1970, c. C-30, and subsequent amendments.

AVIS

La qualité de cette microforme dépend grandement de la qualité de la thèse soumise au microfilmage. Nous avons tout fait pour assurer une qualité supérieure de reproduction.

S'il manque des pages, veuillez communiquer avec l'université qui a conféré le grade.

La qualité d'impression de certaines pages peut laisser à désirer, surtout si les pages originales ont été dactylographiées à l'aide d'un ruban usé ou si l'université nous a fait parvenir une photocopie de qualité inférieure.

La reproduction, même partielle, de cette microforme est soumise à la Loi canadienne sur le droit d'auteur, SRC 1970, c. C-30, et ses amendements subséquents.

NL-339 (r. 88/04) c

Canada

UNIVERSITY OF ALBERTA

DESIGN, DEVELOPMENT AND CONSTRUCTION OF R.F. ANTENNA FOR NMR IMAGING AND SPECTROSCOPY OF THE HUMAN BREAST

BY

IAN THOMAS ©

A THESIS
SUBMITTED TO THE FACULTY OF GRADUATE STUDIES AND RESEARCH
IN PARTIAL FULFILMENT OF THE REQUIREMENTS FOR THE DEGREE
OF MASTER OF SCIENCE.

DEPARTMENT OF APPLIED SCIENCES IN MEDICINE.

EDMONTON, ALBERTA
SPRING 1990.

National Library of Canada
Canadian Theses Service
Ottawa, Canada
K1A 0N4

Bibliothèque nationale du Canada
Service des thèses canadiennes

NOTICE

The quality of this microform is heavily dependent upon the quality of the original thesis submitted for microfilming. Every effort has been made to ensure the highest quality of reproduction possible.

If pages are missing, contact the university which granted the degree.

Some pages may have indistinct print especially if the original pages were typed with a poor typewriter ribbon or if the university sent us an inferior photocopy.

Reproduction in full or in part of this microform is governed by the Canadian Copyright Act, R.S.C. 1970, c. C-30, and subsequent amendments.

AVIS

La qualité de cette microforme dépend grandement de la qualité de la thèse soumise au microfilmage. Nous avons tout fait pour assurer une qualité supérieure de reproduction.

S'il manque des pages, veuillez communiquer avec l'université qui a conféré le grade.

La qualité d'impression de certaines pages peut laisser à désirer, surtout si les pages originales ont été dactylographiées à l'aide d'un ruban usé ou si l'université nous a fait parvenir une photocopie de qualité inférieure.

La reproduction, même partielle, de cette microforme est soumise à la Loi canadienne sur le droit d'auteur, SRC 1970, c. C-30, et ses amendements subséquents.

ISBN 0-315-60228-7

NL-339 (r. 88/04) c

Canada

THE UNIVERSITY OF ALBERTA

RELEASE FORM

NAME OF AUTHOR: IAN THOMAS

TITLE OF THESIS: DESIGN, DEVELOPMENT AND CONSTRUCTION OF R.F. ANTENNA FOR NMR IMAGING AND SPECTROSCOPY OF THE HUMAN BREAST.

DEGREE: MASTER OF SCIENCE

YEAR THIS DEGREE GRANTED: 1990

Permission is herby granted to THE UNIVERSITY OF ALBERTA LIBRARY to reproduce single copies of this thesis and to lend or sell such copies for private, scholarly or scientific research purposes only. The author reserves other publication rights, and neither the thesis nor extensive extracts from it may be printed or otherwise reproduced without the author's written permission.

....

Department of Physics, Faculty of Science,
Khon Kaen University, Khon Kaen,
40002, Thailand.

Date:

THE UNIVERSITY OF ALBERTA

FACULTY OF GRADUATE STUDIES AND RESEARCH

The undersigned certify that they have read, and recommend to the Faculty of Graduate Studies and Research for acceptance a thesis entitled DESIGN, DEVELOPMENT AND CONSTRUCTION OF R.F. ANTENNA FOR NMR IMAGING AND SPECTROSCOPY OF THE HUMAN BREAST submitted by IAN THOMAS in partial fulfilment of the requirements for the degree of MASTER OF SCIENCE.

P. S. Allen
(supervisor)

Richard E. Snyder

D G Hughes

Date:

Dedicated to my parents, John and Grace Thomas.

ABSTRACT

A conical helix coil has been designed for Nuclear Magnetic Resonance (NMR) imaging, proton spectroscopy and phosphorus spectroscopy of the human female breast. The three-turn coil was designed to give a high degree of magnetic field homogeneity over the inside of the coil. A switched capacitor allowed the coil to be tuned for either proton or phosphorus NMR in a 1.5 T Philip's Gyroscan spectrometer.

Images of the breasts of normal volunteers were taken, and all the images were seen to contain two distinct regions, having high and low signal intensity on the $T_E = 50$ ms, $T_R = 580$ ms spin echo images. The percentage of low-intensity region in the gland, measured from the images, was found to correlate with the menopausal status of the woman: nulliparous premenopausal, multiparous premenopausal, lactational and postmenopausal.

Proton spectroscopy using the conical helix breast coil was performed on 13 volunteers, and areas of water and fat spectral peaks were correlated with the ratio of low to high-intensity region measured over the same volume in the images. The positive correlation implies that the low-intensity region is mainly water and the high-intensity region mainly fat.

Phosphorus NMR spectra from a 45 mm slice through the breast, parallel to the chest wall, demonstrated the presence of phosphomonoesters (PME), phosphodiesters (PDE), adenosine triphosphate (ATP) and inorganic phosphate within the breast. The NMR signal from these metabolites was found to correlate with the volume of low-intensity region in the same slice, measured from the images.

This indicates that the phosphorus metabolites are concentrated in the low-intensity region on the images, identified as the parenchyma of the breast.

This correlation of phosphorus signal to parenchyma indicates that NMR imaging may be used to predict the phosphorus signal expected from the normal breast, and this may help in assessing breast cancer treatment.

ACKNOWLEDGEMENTS

My thanks must firstly go to my supervisor Dr. Peter Allen for giving me the opportunity to study at the University of Alberta, and for his continued support and confidence during my time in Edmonton.

I received much useful comment from my examination committee: Dr. P. Allen, Dr. D.Fenna, Dr. D.G.Hughes, Dr. A.McEwan and Dr. R.Snyder. They all made significant contributions to my understanding of the thesis material and gave thoughtful and constructive criticism.

I am indebted to the staff of the Clinical NMR Unit and the Animal Unit for keeping the equipment running smoothly and for teaching me about their operation and use, especially Mr. D.Ellinger, Mr. D.Georghiu, Mrs. I.Ho and Mr. D.Doran.

In the volunteer trials I worked in collaboration with Dr. Scott Ernst of the Cross Cancer Institute, who taught me much about the breast and whose company while gathering data has been a real pleasure.

My interest in image processing was stirred by the determined teaching of Dr. Z.Koles.

Dr. Chunpen S.Thomas and Dr. Chris Hanstock provided encouragement and many helpful discussions which enabled me to see NMR from another perspective.

For the statistical analysis and much else, thanks to George Sexsmith, doctor extraordinaire.

I was lucky enough to have a loving home while studying, provided by Sarah and Chunpen Thomas.

TABLE OF CONTENTS

page
Chapter 1 General Introduction. 1

- 1.1 The need for the study. 1
- 1.2 NMR imaging. 2
  - 1.2.1 Use in diagnosis. 2
  - 1.2.2 Imaging of the breast. 3
- 1.3 NMR spectroscopy. 3
- 1.4 Surface coils for the human breast. 4
- 1.5 Objectives and scope of the study. 5

Chapter 2 The human female breast. 7

- 2.1 Anatomy. 7
- 2.2 Histology. 10
- 2.3 Development. 11
- 2.4 The breast during pregnancy and lactation. 12
- 2.5 Breast energy metabolism. 12
- 2.6 Cancer of the breast. 16

Chapter 3 Some Principles of NMR. 17

- 3.1 Background to NMR. 17
  - 3.1.1 Spin and the nuclear magnetic moment. 20
  - 3.1.2 Nuclear interactions. 21
    - 3.1.2.1 Magnetic dipole-dipole interaction. 21
    - 3.1.2.2 Chemical shift. 22
    - 3.1.2.3 Scalar coupling. 24
  - 3.1.3 Relaxation and its mechanisms. 25
  - 3.1.4 NMR spectra. 26
- 3.2 NMR Techniques. 28
  - 3.2.1 Pulse sequences. 28

3.2.3 Spatial localization. 31
3.2.3.1 Image-selected *in vivo* spectroscopy. 32
3.3 The NMR spectrometer. 33
3.3.1 Introduction. 33
3.3.2 The Philips Gyroscan. 37

Chapter 4 Approaches to NMR surface coil design. 39

4.1 Introduction. 39
4.1.1 The purpose of a surface coil. 39
4.1.2 Some practical surface-coil design considerations. 40
4.2 The Biot-Savart Law. 41
4.3 Numerical integration. 43
4.4 Spherical harmonic analysis. 45
4.4.1 Resolution of a magnetic field into spherical harmonic components. 46
4.4.2 Field design using spherical harmonic analysis. 46
4.5 Signal-to-noise ratio. 47

Chapter 5 A Mathematical Analysis of the Magnetic Field from Circular Coils. 51

5.1 Introduction. 51
5.1.1 The Legendre polynomials. 52
5.1.2 The spherical harmonics. 56
5.2 A circular coil centered on the origin. 56
5.3 Circular coil displaced from origin along the axis of symmetry. 64
5.4 Coil coordinate transformation for series convergence. 68
5,5 Multi-loop coil field determination. 70

Chapter 6 The Design of the Breast Coil. 74

6.1 Field calculation and the COIL program. 74
6.2 Example of coil field calculation using the program COIL. 75
6.3 Using COIL to design the breast coil. 79
6.4 Testing the breast coil. 85
    6.4.1 Phantom imaging. 85
    6.4.2 Comparison of the breast coil with the body coil. 85

Chapter 7 The Normal Volunteer Breast Trials. 89

7.1 Selection of the volunteers. 89
7.2 Examination procedure. 89
7.3 The imaging method. 91
7.4 The spectroscopy method. 92
    7.4.1 Proton spectroscopy. 93
    7.4.2 Phosphorus spectroscopy. 94

Chapter 8 NMR Imaging of the Breast. 95

8.1 Images from normal volunteers. 95
8.2 Numerical data from the images. 102
8.3 Preliminary interpretation of image data. 105
8.4 A possible breast image correction technique. 108

Chapter 9 Spectroscopy of the Breast. 114

9.1 Proton spectroscopy. 114
    9.1.1 Spectra from normal volunteers. 114
    9.1.2 Correlation of spectra with images. 116

9.1.3 Preliminary interpretation of spectral data. 118
9.2 Phosphorus spectroscopy. 118
9.2.1 Spectra from normal volunteers. 118
9.2.2 Correlation of spectra with breast characteristics. 120
9.2.3 Preliminary interpretation of spectral data. 124

Chapter 10 Conclusions. 127

References 130

Appendix A The COIL program. 137

Appendix B Correction of spectra. 145

Appendix C 16 bit to 8 bit image conversion program. 162

Appendix D Image correction programs. 164

Appendix E Image transfer. 174

Appendix F Legendre transform program. 174

Appendix G Normal volunteer consent form. 184

Appendix H Multi-loop coil field calculation using spherical harmonic series. 187

LIST OF TABLES

page

Table 3.1.2.2 Chemical shifts observed in high resolution and *in vivo* spectroscopy. 24

Table 5.1.1.1 Comparison of the values of Legendre polynomials between those calculated in MacPascal on the Macintosh microcomputer and those from a mathematical handbook 55

Table 6.4.2.1 Comparison of the signal-to-noise ratios and ghosting levels of breast and body coils. 87

Table 8.2.1 Data measured from normal volunteer images. 106

Table 8.3.1 Analysis of variance and Scheffe's test on imaging data. 107

Table 9.1.2.1 Data from imaging and proton spectroscopy 117

Table 9.2.2.1 Imaging and spectral data from breasts filling the breast coil cups. 124

LIST OF FIGURES

page

Figure 2.1.1 The female breast . 8
Figure 2.1.2 Lymphatic drainage. 9
Figure 2.5.1 Simplified metabolic pathways. 14

Figure 3.1.1 Distribution of nuclear moments in (a) no external field and (b) external field cases. (c) shows the orientation of the perturbing magnetic field B_1. 18
Figure 3.1.2.1 Energy level diagrams for two-spin system interacting by (a) secular and (b) non-secular terms of the dipolar-dipolar interaction Hamiltonian. 23
Figure 3.1.3.1 The relaxation of the macroscopic magnetization following a 180^o pulse. 27
Figure 3.2.1.1 90^o - acquire pulse sequence. 28
Figure 3.2.1.2 Spin echo sequence. 30
Figure 3.2.3.1 A one-dimensional ISIS experiment. 32
Figure 3.2.3.2 Three-dimensional ISIS localization sequence. 34
Figure 3.3.1.1 Block diagram of a basic pulsed NMR spectrometer. 36
Figure 3.3.2.1 Block diagram of Philips Gyroscan spectrometer. 38

Figure 4.2.1. Variables used in the Biot-Savart equation. 42
Figure 4.2.2 The axial field along the axis of a circular coil radius a = 1m, with a current of 1A. 43
Figure 4.3.1 Dividing a current loop (a) into linear elements (b) to calculate the flux density **B** at point P. 44
Figure 4.3.2 Geometry for field from straight wire segment. 45
Figure 4.5.1 The surface coil geometry . 47
Figure 4.5.2 Signal from a circular surface coil. 48
Figure 4.5.3 SNR of circular surface coil as a function of coil radius 50

Figure 5.1.1.1 Zeroth order Legendre functions n=0 to 6. 53
Figure 5.1.1.2 First order Associated Legendre functions n=1 to 6. 53

Figure 5.1.1.3 Example of a curve fit using Legendre polynomials. 55

Figure 5.2.1 Definition of coordinates used in the derivation of the field from a circular coil centered at the origin. 56

Figure 5.2.2 The total transverse field from a circular surface coil calculated by numerical integration. 61

Figure 5.2.3 The plane over which the field from the circular coil was calculated. 62

Figure 5.2.4 The field from a surface coil calculated from the spherical harmonic expansion, 62

Figure 5.2.5 The field separations of B_r and B_θ into the coefficients of $P_n(\cos\theta)$ and $P_n^1(\cos\theta)$ respectively in equation (5 - 16). 63

Figure 5.3.1 Coordinates for the case of a circular coil shifted away from the origin. 64

Figure 5.4.1 Coil coordinate transformation to accelerate series convergence. 69

Figure 5.4.2 The transverse field $B_\perp$ calculated from spherical harmonics, but using the transformation of the point at which the field is calculated back to the xz plane. 69

Figure 5.5.1 The transverse field (xy plane) from a circular coil axial with the y axis but displaced from the origin. 71

Figure 5.5.2 A three loop coil approximating a conical helix. 71

Figure 5.5.3 Transverse field (xy plane) from the three loop coil approximating the conical helix coaxial with the y axis. 72

Figure 6.2.1 The definition of the circular coil file. 75

Figure 6.2.2 The calculated B_y component of the field along the axis of a 1m circular coil at discrete points. 76

Figure 6.2.3 The transverse field $B_\perp$ in the xy plane for the circular coil. 77

Figure 6.2.4 Tip angle contour plot for circular coil for section parallel to B_0 field. 77

Figure 6.2.5 Tip angle contour plot for circular coil for section perpendicular to the B_0 field. 78

Figure 6.3.1 Some coil geometries considered for the breast coil. 80

Figure 6.3.2 Comparison of fields from different breast coil geometries. 80
Figure 6.3.3 Improved field uniformity by non-linear turns spacing. 81
Figure 6.3.4 The three-turn modified conical helix used as the breast coil 82
Figure 6.3.5 Patient bed used to mount breast coils. 83
Figure 6.3.6 The breast coil electrical circuit. 83
Figure 6.4.1.1 Images taken with (a) the breast coil and (b) the body coil. Field of view is 100 x 100 mm and slice thickness is 2 mm. 86

Figure 7.3.1 Imaging coordinate system. 91
Figure 7.4.1 Spectroscopy coordinate system. 93

Figure 8.1.1 Fat types seen in images of the breast. 97
Figure 8.1.2 (a) blood vessels and (b) ducts can be readily identified on images of the breast. 99
Figure 8.1.3 (a) premenopausal and (b) lactational breasts. 100
Figure 8.1.4 (a) pre and postmenopausal breasts. 101
Figure 8.1.5 (a) normal and (b) obese premenopausal breasts. 103
Figure 8.1.6 (a) left and (b) right breasts of a 24-year-old nulliparous woman. 104
Figure 8.2.1 Volumes over which high/low intensity ratio measured. 106
Figure 8.3.1 Correlation of low intensity regions in breast images as percentage of total breast with menstrual status of women. 107
Figure 8.4.1 The plane through the breast coil used for calculated field sensitivity maps. 110
Figure 8.4.2 The calculated sensitivity maps for the breast coil when the field at the centre is different fractions of B_{90}. 112
Figure 8.4.3 Application of correction to a region of the image, to reduce the effects of surface coil inhomogeneity. 110
Figure 8.4.4 (a) uncorrected and (b) corrected image using the image correcting technique. 113

Figure 9.1.1 Proton spectra of (a) lactational and (b) post-menopausal breasts. The water peak is on the left, and the fat peak on the right. 115

Figure 9.1.2.1 Correlation of imaging and proton spectroscopy data from the same volume of gland. 117

Figure 9.2.1 Unlocalized ^{31}P spectrum of the breast. 119

Figure 9.2.2 The selected slice for ^{31}P spectroscopy. 119

Figure 9.2.3 Localized ^{31}P spectrum of the breast. 120

Figure 9.2.2.1 Correlation of total phosphorus peak area with volume of low intensity region from equivalent volume in images. 122

Figure 9.2.2.2 Correlation of total phosphorus peak area with volume of high intensity region from equivalent volume in images. 122

Figure 9.2.2.3 Correlation of ATP peak areas with volume of low intensity region from equivalent region in images. 123

Figure 9.2.2.4 Correlation of area of the ATP peaks with volume of high intensity region from the equivalent region in images. 123

Figure 9.2.2.5 Correlation of areas of phospholipid peak areas with volume of low intensity region from equivalent volume in images. 125

Figure 9.2.2.6 Correlation of phospholipid peak areas with volume of high intensity region from equivalent volume in images. 125

Figure AppB.1 The field data was calculated for the xy plane (a), and this data was used to find the field in an arbitrary plane through the origin (b) using the algorithm above. 148

Figure AppB.2 Geometry for signal component evaluation 150

Figure AppB.3 Demonstrating the discrepancy between the profile band maximum and the true 90° tip angle position. 151

Figure AppB.4 The relationship between the peak of the 90° band observed from a profile and the true position of the 90° tip angle. 153

Figure AppB.5 The use of the Correction Factor programme. 155

Figure AppD.1 Parameters used in the Image Correction programme. 165

LIST OF SYMBOLS AND ABBREVIATIONS

a	The radius of the coil.
acetyl CoA	Acetyl coenzyme A.
ADC	Analogue-to-digital converter.
ADP	Adenosine diphosphate.
ATP	Adenosine triphosphate.
B	Magnetic flux density.
b	Magnetic field per unit current.
B_0	The external magnetic field.
B_1	The RF magnetic field.
B_{90}	The field required to cause 90° tip-angle.
c	The speed of light.
dl	An element of wire.
DRESS	Depth-resolved surface-coil spectroscopy.
e	The electronic charge.
f	Distance from the origin to a wire element.
FAD	Flavine-adenine dinucleotide.
FAD_{ox}	Oxidised flavine-adenine dinucleotide.
FAD_{red}	Reduced flavine-adenine dinucleotide.
FID	Free induction decay.
I	Electric current, nuclear spin.
ISIS	Image-selected *in vivo* spectroscopy.
J	Total angular momentum.
L	Angular momentum.

M	Magnetization.
m	Mass
m_e	The electron mass.
M_{xy}	The transverse magnetization.
N	Number of magnetic moments per unit volume.
NAD	Nicotinamide-adenine dinucleotide.
NAD_{ox}	Oxidised nicotinamide-adenine dinucleotide.
NAD_{red}	Reduced nicotinamide-adenine dinucleotide.
NMR	Nuclear magnetic resonance.
PCr	Phosphocreatine.
$P_n^m(\cos\theta)$	Associated Legendre function.
$P_n(\cos\theta)$	Legendre function.
$P_n(x)$	Legendre polynomial.
ppm	Parts per million.
PSD	Phase sensitive detector.
Q	The coil quality factor.
r	Distance.
RF	Radio frequency.
S	Intrinsic angular momentum or spin.
SD	Standard deviation.
SNR	Signal-to-noise ratio.
SPARS	Spatially resolved spectroscopy.
STEAM	Stimulated-echo acquisition mode.
T	Temperature.
T_1	The spin-lattice relaxation time.

T_2	The spin-spin relaxation time.
T_E	Echo time.
T_R	Repetition time.
V	Volume.
VSE	Volume-selective excitation.
x, y, z	Cartesian coordinates.
x_ρ, y_ρ, z_ρ	Rotating-frame Cartesian coordinates.
τ	Torque.
ρ	Distance.
γ	The gyromagnetic ratio.
$\hat{e}$	A unit vector.
μ	Magnetic moment.
μ_0	The permeability of free space.
ω_0	The Larmor frequency.
θ	Angle, the polar angle.
ϕ	Angle, the azimuthal angle.
$\hbar$	Planck's constant divided by 2π.

CHAPTER 1

GENERAL INTRODUCTION

The application of the natural sciences in medicine requires cooperation between trained scientists and medical doctors. It also requires scientists to learn some medicine. This thesis represents the application of nuclear magnetic resonance to determine the biochemical metabolite distribution in the female human breast. This involved the design and construction of a special purpose coil to enable the best images and spectra from the breast to be obtained from the Philips Gyroscan NMR spectrometer of the Alberta Heritage Foundation for Medical Research. It also required the interpretation of these results to produce a simple model of the female human breast. In this introductory chapter an outline and literature review of the project subject matter is given.

1.1 The Need for the study.

About 4,000 Canadian women die from breast cancer every year [Statistics Canada, 1988]. Both NMR imaging and spectroscopy have been used to study breast cancer in the past, and, while NMR imaging is capable of showing tumours and measuring some of their NMR properties, *in vivo* NMR spectroscopy has not yet been able to demonstrate clearly the energy metabolism of breast tumours. One reason for this is experimental; the signal-to-noise ratio of spectroscopy of the breast has not been high, and some researchers have reported being unable to distinguish the phosphorus spectrum from the noise. A higher signal-to-noise ratio would enable greater precision in the measurement of metabolite concentrations, and thus enable more definite conclusions to be drawn from the experimental data.

While some workers have shown that some breast tumour phosphorus spectra have certain characteristics, there is still insufficient knowledge of the phosphorus spectrum to be expected from a healthy breast. A knowledge of the spectrum expected from a particular woman would be helpful in determining whether or not the woman has a tumour, the type of tumour and the condition of that tumour.

Thus there is need both for an NMR coil giving a high signal-to-noise ratio for phosphorus spectroscopy and for a baseline study of the normal female breast.

1.2 NMR imaging.

1.2.1 Use in diagnosis.

NMR imaging for medical use was developed in the early 1970s [Lauterbur, 1973; Mansfield and Grannel, 1973]. It has advantages over other imaging modalities in that it does not rely on the attenuation of a beam, with the associated problems of diffraction and absorption. The first NMR images of the whole body were made in the late 1970s; the resolution was of the order of 1 cm. Resolution of the order of 1 mm is possible with present-day imaging machines such as the Philips Gyroscan used in this study. Images which are weighted to emphasize T_1 and T_2 relaxation times are of particular diagnostic use, and T_1 has been shown to change during tumour growth and regression. This change in T_1 is thought to be due to redistribution of water and fat between different tissue environments [Kroeker *et al.*, 1988].

1.2.2 Imaging of the breast.

With breast cancer so prevalent among women, there have been many studies to assess NMR imaging for diagnosis, staging or treatment monitoring of breast cancer.

For diagnosis, Dash *et al* . [1986] reported that NMR imaging was superior to mammography for differentiating solid from cystic lesions, and Partain *et al.* [1986 p292] concluded that NMR imaging is "the most sensitive modality for the identification of breast lesions". NMR imaging is suitable for use in regions close to the chest wall and to prostheses [Heywang *et al.*, 1986; Partain *et al.*, 1986; Stelling *et al.*, 1985] and it provides information about the internal structure of breast masses, which makes it useful for identifying a breast mass. Most researchers conclude that NMR imaging cannot compete with X-ray mammography for speed and economy, but that it is a useful adjunct modality for the evaluation of breast lumps.

NMR imaging of the breast can clearly distinguish subcutaneous veins, pectoral muscle and the prepectoral fascial plane [Stelling *et al.*, 1985]. That this is so can be seen from the imaging results of this study which appear in Chapter 8.

1.3 NMR spectroscopy

In vivo NMR spectroscopy was first reported in 1973 [Moon and Richards, 1973] when a ^{31}P NMR spectrum was obtained from intact red blood cells. Phosphorus NMR has continued to be important for animal studies and clinical applications while ^{13}C NMR is widely used for the determination of biochemical pathways [Morris, 1988]. *In vivo* proton NMR spectroscopy has suffered from the problem of high concentrations of water (~100 M) masking the presence of low concentrations of metabolites (< 1 mM). Apart from the water, the -CH_2- resonance of lipids (~1 M) also needs to be suppressed in order to measure metabolite concentrations [Morris, 1988]. Spectral editing techniques, which selectively excite certain metabolite peaks in the NMR spectrum, are now enabling proton NMR to be used to measure metabolite concentrations.

Techniques using surface coils, distorting the B_0 magnetic field as in topical magnetic resonance [Gordon, Harley and Shaw, 1982], using selective excitation pulses and magnetic gradients such as in the work of Garroway, Grannel and Mansfield [1974], in Depth-Resolved Surface-coil Spectroscopy (DRESS) [Bottomley, Foster and Darrow, 1984] or the Image Selective *In vivo* Spectroscopy (ISIS) of Ordidge, Connelly and Lohman [1986], provide methods of localizing the signal obtained from NMR spectroscopy to a region of tissue under investigation.

Proton and phosphorus spectra from the normal human breast appear in Chapter 9 of this thesis

1.4 Surface coils for the human breast

Surface coils are useful for superficial parts of the body, where the proximity of the coil to the tissue under study results in improved signal-to-noise ratio (see Chapter 4). If the same coil is used for transmitting and receiving, the radiation absorbed by the body can be reduced and localized. The breast, lying close to the skin, is a suitable organ for study by surface coil.

The simplest surface coil, a single-turn circular coil, was used by Dash *et al.*[1985], Heywang *et al.*[1986] and Wiener *et al.*[1986] for imaging studies on the breast. The coil was placed coaxial with the gland. The non-uniformity of the magnetic field over the breast exhibits itself in the images as a roll-off of intensity towards the nipple and the chest wall, while the sides of the breast close to the coil show a higher intensity. A theoretical analysis of the field from a circular coil is given in Chapter 5 and a technique for correcting images is described in Section 8.4.

Some researchers have attempted to improve the images obtainable with surface coils. Wolfman *et al.*[1986] designed a surface coil consisting of an array of tubes which enables imaging of both breasts simultaneously, and gives greater uniformity over the breasts. McOwan and Redpath [1987] also image both breasts simultaneously, but this time using tapered saddle coils. Another design used for the breast is the loop-gap resonator [Hornak, Szumowski and Bryant, 1987] which achieves more uniform excitation and a lower radio-frequency (RF) dose to the patient.

1.5 Objectives and scope of the study.

The scope of the present study encompasses the design, construction and testing of the breast coil, but also includes trials of the equipment and technique on normal, healthy volunteers. These trials demonstrate that the breast coil design is suitable for future work on the breast. The study is reported in this thesis in Chapters 4 to 9, with the earlier chapters being introductory and the final chapter a conclusion.

This thesis begins with a review of the breast (Chapter 2) and of nuclear magnetic resonance (Chapter 3) on which the following chapters are built. Chapter 4 brings together some aspects of the design of surface coils; these are dealt with in greater depth in Chapters 5 and 6, in which two possible approaches to the design of surface coils are explored. These are spherical harmonic analysis in Chapter 5, and numerical integration in Chapter 6. In this study, the coil geometry decided upon was more suited to the numerical integration approach, so this was used to calculate the field distribution of the breast coil. Spherical harmonic analysis, which is more suitable for coil geometries having cylindrical symmetry, was used to approximate the magnetic field distribution of the breast coil as a check of the numerical integration method. The last two sections of Chapter 5, which describe an algorithm for calculating spherical harmonic field expansions, are original, while the earlier sections comprise the theoretical foundation for what follows. Chapter 6 describes the design of the coil, and a phantom study to compare it with the normal body coil. The computer programs of Chapters 5 and 6, both of which can be used for coil design, are original. Chapter 7 describes how the breast coil was used in trials on the breasts of normal volunteers. These trials comprised imaging, proton spectroscopy and phosphorus spectroscopy. The imaging results are reported in Chapter 8, with some quantitative analysis of the images. The spectroscopy parts of these trials are reported in Chapter 9, in which some correlation is made between the spectroscopic results and the image data of Chapter 8. Chapter 10 reviews the results and makes recommendations for future work.

CHAPTER 2

THE HUMAN FEMALE BREAST.

The female breast is unusual in that it takes years to develop to the point of being potentially functional. Even then it usually remains inactive for most if not all of the time. Whereas most organs are operational at birth, the breast remains undeveloped until puberty, and from then on develops for over twenty years until the woman is in her mid-thirties. Its development is not continuous, but is cyclic with periods of growth and regression. Towards the end of each menstrual cycle development is at a maximum, and just after menstruation regression is maximal. The purpose of this chapter is to act as an introduction to the anatomy and metabolism of the breast and to assist with the interpretation of images and spectra in Chapters 8 and 9.

2.1 Anatomy

The anatomy of the breast is described in Vorherr [1974 p20] and Rehman [1978 p3]. The breast is normally situated between the second or third rib superiorly and the sixth or seventh rib inferiorly. It extends from the sternum medially out to a variable position laterally. The tissue of the mammary gland may spread over a wider area. The tail of Spence is an elongation of the gland which passes through the axillary fascia and ends near the axillary lymph nodes. The gland averages 10 to 12 cm from top to bottom, and 3 to 5 cm in thickness, weighing around 200 g [Rehman, 1978 p5]. The size and shape of the breast varies considerably, with race as well as age being important. Figure 2.1.1 gives a schematic view of the breast.

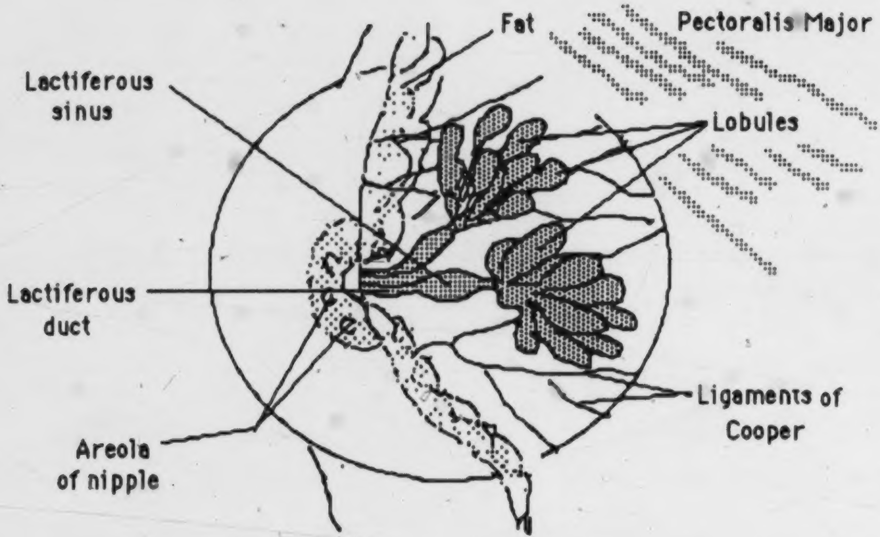
Fat
Pectoralis Major
Lactiferous sinus
Lobules
Lactiferous duct
Ligaments of Cooper
Areola of nipple

Figure 2.1.1 The female breast (adapted from Wilson [1987 p293]).

The skin of the breast, like skin elsewhere, has a layer of subcutaneous fat. The breast lies between the skin and the fascias of the pectoralis major and the seratus anterior muscles, to which it is attached by connective tissue. This connective tissue supports the gland, and forms a structure between the skin and the fascia of the muscles behind. The parts of the gland are supported in a lattice of supportive connective tissue (ligaments of Cooper) and fat, of varying thickness, called the stroma.

The breast is supplied medially by the internal mammary artery, inferiorly by the intercostal artery and laterally by the lateral thoracic artery. It is drained of blood by the internal mammary vein, the axillary vein and others.

The breast drains into several lymph nodes, including the axillary lymph nodes, the internal mammary nodes and the abdominal lymphatics (Figure 2.1.2).

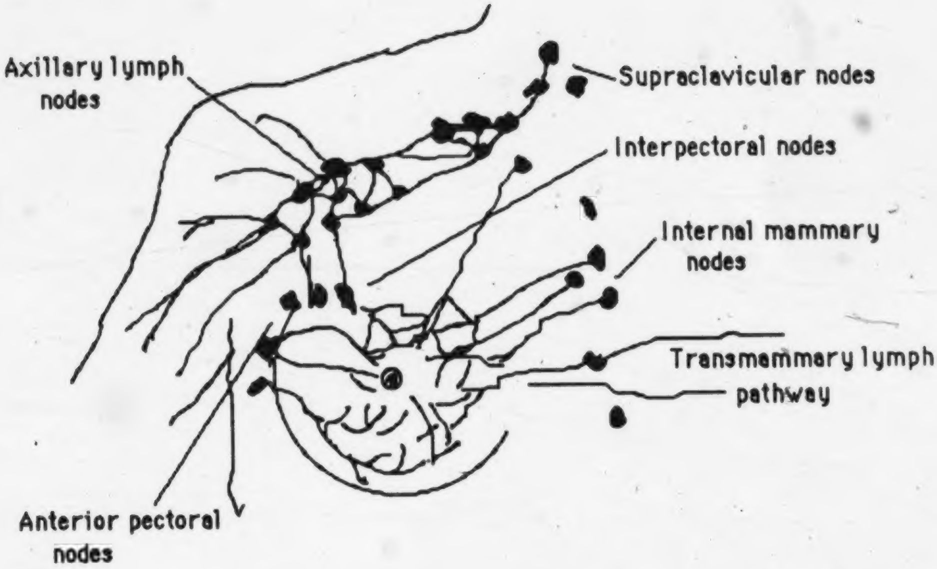
Axillary lymph nodes
Supraclavicular nodes
Interpectoral nodes
Internal mammary nodes
Transmammary lymph pathway
Anterior pectoral nodes

Figure 2.1.2 Lymphatic drainage

[adapted from Rehman, 1978 p10; Wilson, 1987 p294; Vorherr 1974 p33]

The simplest breakdown of the breast tissue is into the two tissue types, stroma and parenchyma. Russo and Russo [1987] showed that the ratios between these tissue types varies from about 9:1 (stroma:parenchyma) at puberty to 3:1 postpuberty. In pregnancy it decreases to 2:3 in early pregnancy and to 1:4 by the end. Post-menopause the ratio would be expected to rise as the gland tissue is deleted.

The stroma consists of adipose cells and connective tissue, their blood supply, nerves and lymphatics. Stroma can be subdivided into two types: interlobular and intralobular. The interlobular is formed from the fat pad into which the ducts grow following puberty. The intralobular separates the lobules and supports their vascular and lymph supplies. The intralobular stroma contains a higher density of vascular and lymph supplies, since it is supporting the gland cells, whereas the interlobular stroma has, apart from large vessels, supplies for itself alone.

Russo and Russo [1987 p98] measured the amounts of different types of stroma for various women, and found a ratio of 5:1 (interlobular:intralobular) at puberty, decreasing to 3:1 for parous women. In pregnancy the ratio drops further to 1:1 at the start, increasing to 3:1 by the end.

The parenchyma consists of the ducts and lobes of the mammary gland. The amount of duct tissue does not increase much after puberty, but the amount of gland tissue does. There is also a change in the type of tissue, with a trend towards smaller alveoli as the gland develops. The ratio of lobes to ducts starts at about 8:1 at puberty, and increases to about 20:1 in the parous woman. In pregnancy this increases to 30:1 early and about 40:1 later.

2.2 Histology

The histology of the breast is described in Vorherr [1974 p22 *et seq.*]. The gland consists of small sac-like alveoli which feed into lactiferous ducts. The alveoli are grouped into lobules, and the lobules into lobes. There are 15-20 lobes, each consisting of 20-40 lobules, with each of these having 10-100 alveoli. A fully developed lobule consists of a cluster of alveoli which opens into the terminal ducts. The terminal ducts converge and eventually lead to the primary duct of the lobe, the lactiferous duct, which expands into a lactiferous sinus as it passes towards the nipple. Each lobe is surrounded by fat which contains the blood supply, nerves and lymphatics for that lobe. The skin is often attached to the ducts, but there is freedom between the rear of the gland and the pectoralis major and seratus anterior muscles, allowing the breast to move.

The nipple is the termination of the lactiferous sinuses. When the muscles in the nipple and surrounding areola contract, the nipple becomes erect and the lactiferous sinuses are emptied.

2.3 Development

At birth the breast consists of ducts, with some short ductules, attached to the nipple [Russo and Russo, 1987 p67]. The ducts are embedded in a pad of fat and connective tissue which serves to support the ducts. In the first 10 years of life the development of the breast follows the development of the rest of the body, but without any functional development.

At the onset of puberty the ducts grow and divide; after the first menstruation, alveolar buds begin to appear. After one or two years these alveolar buds form the type-1 lobules which are predominant in the breasts of nulliparous women. Development following menstruation is cyclic, with periods of increased production of alveolar buds near the end of each menstrual cycle, and periods of cell deletion early in the cycle. Since the deletion loss is less than the cell production, the overall effect is a steady increase in the size of the breast, and increasing numbers of type-1 lobules, until the age of about 35.

As the ovaries begin to decline before the menopause, the lobules shrink and collapse, and there are reductions in the structural tissue, accompanied by increased fat deposit. The post-menopause breast consists of fat and connective tissue almost exclusively. There is a homogenization of the stroma, which previously could be differentiated as interlobular or intralobular.

2.4 The Breast during pregnancy and lactation

During pregnancy the breasts develop to their full extent [Russo and Russo, 1987 p81]. During the first half the ducts develop new branches, new lobules are created, and existing lobules increase the number of buds they contain. While the number of buds increases, the size of each bud decreases, but the overall size of the lobule increases. In a fully developed lobule, these buds become the acini which produce milk. By the second half of pregnancy the ductal structure is almost complete, and the development of acini predominates. The luminae of the acini begin to fill with colostrum, a special form of milk.

Colostrum is delivered during the first week after birth, and three or four weeks after birth mature milk begins. Almost as long as the milk is removed from the breast the production continues. When the child is weaned, the accumulation of milk in the luminae and epithelial cells of the acini causes cessation of production and involution of the gland. Lobules begin to atrophy, and fat begins to be deposited in the stroma once more.

The breast following pregnancy does not return completely to its pre-pregnancy state, but continues to have a higher proportion of glandular tissue than the virginal breast.

2.5 Breast metabolism

The metabolism of breast tissue is basically the same as the metabolism of tissue elsewhere in the body [Durham, 1989 p124, Tortora, 1987 p 633].

Energy metabolism is the group of biological processes by which energy is liberated from organic molecules by their breakdown into smaller molecules, or is used up in the synthesis of larger molecules. Catabolism and anabolism describe reactions which release and consume energy respectively.

The breakdown of organic molecules such as glucose, fatty acids and amino acids to produce ATP is known as cellular respiration. When oxygen is used as the final electron acceptor the process is called aerobic cell respiration, whereas when the electrons are accepted by NAD_{ox} and transferred to pyruvic acid to form lactic acid, the process is said to be anaerobic.

Glucose is converted into ATP through glycolysis and the Krebs' cycle. Glycolysis produces pyruvic acid, which passes through the mitochondrial membrane, within which it is converted into acetic acid and combines with a co-enzyme to form acetyl co-enzyme A (acetyl CoA) which then enters the Krebs' cycle. This is a cycle since the acetyl CoA is combined with oxaloacetic acid, and then carbon dioxide is removed, with the liberation of energy until oxaloacetic acid is left to re-enter the cycle.

Fatty acids are liberated from fat in adipose tissue by lipase enzymes. In the process of β-oxidation, units two carbon atoms long ($-CH_2-CH_2-$) are repeatedly broken off the fatty acids, resulting in the formation of acetyl CoA which is then used in the Krebs' cycle.

Amino acids can be used for energy by removing amine groups and excreting the amine groups as urea in the urine. The remaining keto group is used in the Krebs' cycle. The keto acids are pyruvic acid and the Krebs' cycle acids.

The three principal chemicals involved in the process of extracting energy from the breakdown of glucose, fatty acids and proteins are NAD, FAD and ATP. Both NAD and FAD exist in two forms: NAD_{red} & NAD_{ox}, FAD_{red} & FAD_{ox}. These chemicals are used in the reduction and oxidation reactions. In reduction reactions NAD_{OX} and FAD_{OX} strip hydrogen atoms from complex molecules. ATP is used to absorb the energy produced by the catabolism of larger molecules. This is done by attaching the phosphate group to ADP to produce the unstable and high-energy molecule ATP, in which form the energy can be easily transferred to fuel muscles and other cells.

The blood supplies energy sources to the cells in the body. Since there are several types of energy sources in the blood which can be used (glucose, ketone bodies, fatty acids, etc.,) different organs select preferentially different energy sources.

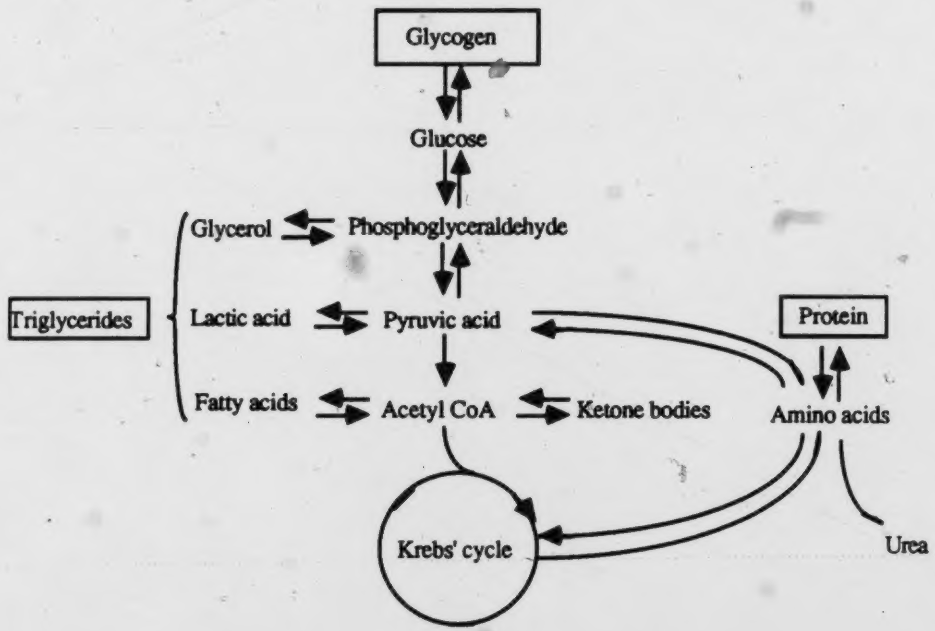
Glycogen
Glucose
Glycerol
Phosphoglyceraldehyde
Triglycerides
Lactic acid
Pyruvic acid
Protein
Fatty acids
Acetyl CoA
Ketone bodies
Amino acids
Krebs' cycle
Urea

Figure 2.5.1 Simplified metabolic pathways (adapted from Fox [1984])

The various steps in the transfer of energy from large molecules to ATP, NAD and FAD are catalyzed by the enzymes and use co-factors. In glycolysis the enzymes and cofactors are Mg^{++}, ATP, NAD, Mn^{++} and K^{+}. Accumulating ATP also has a negative feedback effect by inhibiting the operation of the enzyme phosphofructokinase. The Krebs' cycle produces ATP, NAD_{red} and FAD_{red} as energy carriers, and CO_2 as waste product. In the process of oxidative phosphorylation NAD_{red} and FAD_{red} give up their energy to create ATP .

Phospholipid metabolism in cells involves anabolic and catabolic pathways which maintain cell membranes. There are two main pathways which synthesize phospholipids in the breast and most other tissue [Daly *et al*, 1987]:- from choline to phosphatidylcholine and from ethanolamine to phosphatidylethanolamine. Phosphocholine and phosphoethanolamine are intermediaries in these pathways, and are visible in phosphorus NMR spectra as phosphomonoester peaks. The degradation pathways to choline and ethanolamine pass through glycerophosphorylcholine and glycerophosphorylethanolamine, which are visible in phosphorus NMR spectra as the phosphodiester peaks.

Metabolic regulation is affected by the action of various hormones. These affect the metabolism of carbohydrates, lipids and proteins, as well as the level of glucose in the blood. Glucagon and insulin operate in a negative feedback loop to keep the level of glucose in the blood at a constant level.

2.6 Cancer of the breast

The upper and central part of the mammary gland is mostly glandular tissue, and is the area where breast cancers often occur. Suspensory ligaments of Cooper tend to be shortened with breast carcinomas, causing dimpling of the skin. The tail of Spence passes through the axillary fascia and is in contact with the axillary lymph nodes. Since lymph nodes tend to filter out carcinomatous material from the lymph, cancer may occur secondarily, or metastasize, in lymph nodes. Breast carcinomas often spread to axillary and internal mammary lymph nodes which thus must be removed along with the breast in radical mastectomy. However, there may be invasion of the pectoral muscle and the pleura and apart from spread by the lymph, the cancer cells may enter the blood and spread to the bones, especially lumbar and thoracic vertebrae.

Breast carcinomas can be divided into types, according to the part of the breast where they occur (medullary, lobular, intraductal, papillary, etc.), and by the nature of the carcinoma (colloid, multinodular, mucinous, etc.). Other carcinomas which can occur elsewhere in the body can occur in the breast also— e.g. sweat gland carcinomas, epitheliomas and melanomas.

Various benign diseases have symptoms similar to those found in carcinomas, e.g. lumps in the breast, swelling of the lymph nodes, nipple discharge, etc.[Gallagher *et al*, 1978 p61].

CHAPTER 3

SOME PRINCIPLES OF NMR

In this chapter some of the principles of NMR relevant to this thesis are presented. Space limits the extent of the treatment of this deep and wide subject, so reference is made to standard texts on the subject for further reading. This chapter focusses on the principles used to make the measurements in Chapters 8 and 9.

Section 3.1 introduces the theoretical principles underlying the use of NMR in imaging and spectroscopy. Section 3.2 examines some techniques used in NMR spectroscopy and imaging, and Section 3.3 describes the NMR instrument.

3.1 Background to NMR

Bulk matter consists of very large numbers of nuclei and some of these nuclei possess nuclear spins which, in the absence of an external magnetic field, will be oriented in random directions (Figure 3.1.1(a)). When an external magnetic field B_0 is applied, a spin is forced to precess about the B_0 field by the torque produced by the interaction between its nuclear magnetic moment and the B_0 field. Quantum mechanics allows only two orientations of the precessing spin, for the case of protons and phosphorus nuclei considered in this study, which both have nuclear spin quantum numbers of 1/2. The population of the two states depends on the temperature and strength of the applied external magnetic field. Since the interaction energy is slightly lower in the state in which the spins are aligned parallel to the B_0 field, this state normally has more spins in it than that with spins aligned antiparallel, resulting in a net magnetization in the B_0 direction (Figure 3.1.1(b)).

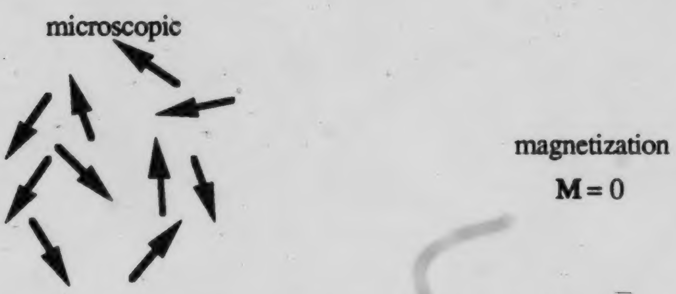
microscopic
magnetization
M = 0

(a) random orientation of nuclear spins produces zero net magnetization.

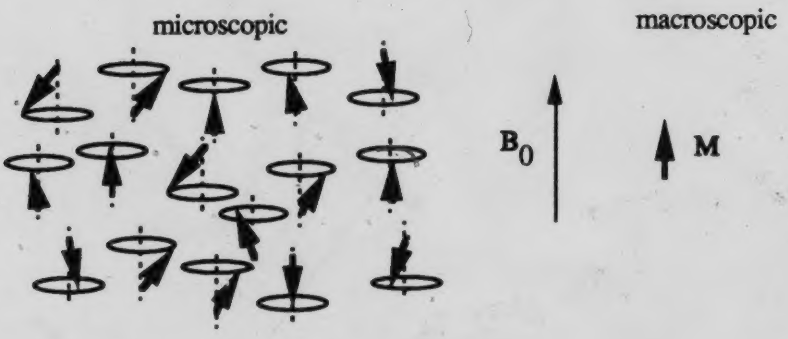
microscopic
macroscopic
B_0
M

(b) application of external magnetic field B_0 causes net magnetization.

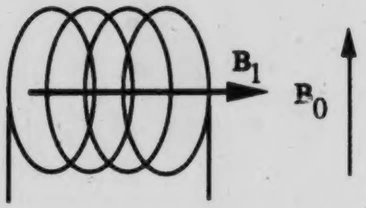

(c) perturbing magnetic field B_1 orthogonal to B_0.

Figure 3.1.1 Distribution of nuclear moments in (a) no external field and (b) external field cases. Figure (c) shows the orientation of the perturbing magnetic field B_1.

The frequency of precession of the spins about the B_0 field is called the Larmor frequency, and is given by

$$\omega_0 = \gamma B_0$$

where B_0 is the flux density of the external field, and γ is the gyromagnetic ratio, i.e. the ratio of magnetic moment to angular momentum, and is a characteristic constant of a particular nucleus.

In order to measure the characteristics of the nuclear spin system, a perturbation is applied to disturb the equilibrium. This is done by applying a radio frequency (RF) magnetic field which is at the Larmor frequency, and which is applied in the plane perpendicular to B_0 (Figure 3.1.1(c)). The length of time that this RF magnetic field is applied is critical. If it is applied for just long enough to invert the populations of the two spin states, it is termed a 180° pulse. A 90° pulse is half as long as this 180° pulse, and leaves the spins equally distributed between the two states. The macroscopic magnetization in the B_0 direction is thus zero, but there is a macroscopic magnetization in the plane perpendicular to the B_0 field.

The return of the spins to their equilibrium state is governed by chemical and magnetic properties of their surroundings, and the weak signal detected as they lose energy to their surroundings is recorded and processed to provide either an NMR spectrum with peaks indicating different nuclear species, or an NMR image showing the spatial distribution of nuclear spins. Sections 3.1.1 to 3.1.4 describe in more detail the processes by which spins return to equilibrium, and the observation of this return.

3.1.1 Spin and the nuclear magnetic moment.

Nuclear spin is a property which some nuclei possess, and which is responsible for the magnetic moment observed in hydrogen, phosphorus and other nuclei. While it acts in a similar way to angular momentum, it is a quantum mechanical attribute.

The relationship between angular momentum and magnetic moment can be seen from the case of the orbiting electron. The electron experiences a central force, and thus its angular momentum **L** is a constant of motion. The magnetic moment caused by the orbiting electron charge e is found to be $\mu = \frac{e}{2m_ec}$ **L** where m_e is the electron mass and c the speed of light. The spin **S** of the electron couples to its orbital angular momentum to give the total angular momentum **J** = **L** + **S**. Since **L** and **S** are both quantized, the magnetic moment has multiple possible values, causing a fine structure in optical spectra taken in the presence of an external magnetic field.

In the case of the nucleus, there is no orbital angular momentum, but the spin causes a magnetic moment. However since nucleons (protons or neutrons) fill shells within the nucleus, the magnetic moment depends on the nuclear spin **I** rather than the sum of the spins of the individual nucleons. For example, a phosphorus nucleus with 15 protons and 16 neutrons has filled neutron shells but is one proton short of filling proton shells, so exhibits a spin of $\frac{1}{2}$, the same as a hydrogen nucleus with just one proton.

The magnetic moment for a nucleus is given by $\boldsymbol{\mu} = \gamma \mathbf{I} \hbar$, where $\hbar$ is Planck's constant divided by 2π. The magnetic moment of the proton is 4.84 nuclear magnetons, and that of phosphorus 1.96 nuclear magnetons. This leads to the Larmor frequency of protons being approximately 2.5 times higher than phosphorus in the same external magnetic field.

3.1.2 Nuclear interactions.

There are several interactions between particles which are responsible for the complexity of NMR spectra and the relaxation of nuclei. An introduction to the interactions is given in Farrah and Becker [1971, p52 *et seq.*]. Not all of these interactions, however, are important in the present study in which the nuclei of interest have spin $\frac{1}{2}$, so only three are considered here: the magnetic dipole-dipole interaction, the chemical shift and the scalar coupling interaction. These three are responsible for most relaxation (see Section 3.1.3) in organic liquids, and for the separable peaks seen in ^{1}H and ^{31}P spectra.

3.1.2.1 Magnetic dipole-dipole interaction.

The magnetic dipole-dipole interaction is not a scalar interaction since its magnitude depends of the orientation of the interacting nuclei relative to the external magnetic field [Abragam, 1961 p216]. Quantum mechanical analysis of a two-spin system reveals that the secular part of the dipolar interaction Hamiltonian leads to a splitting of energy levels of the two-spin system, and thus splitting in the spectral line of the nucleus. Transitions are allowed only as shown on the energy diagram in Figure 3.1.2.1; transitions involving the singlet are forbidden. The separation of the spectral lines is given [Abragam, 1961 p217] by

$$\Delta\omega = \frac{3}{2}\frac{\gamma^2\hbar^2}{r^3}(1 - 3\cos^2\theta),$$

where θ is the angle between the line joining the nuclei and the B_0 field direction, r is the internuclear distance, and γ the gyromagnetic ratio .

This kind of splitting is observed in crystalline hydrates, but in liquids, where the nuclei are moving rapidly with respect to each other, the time average of $\Delta\omega$ is zero, and thus there is no splitting.

In contrast, the non-secular terms in the dipolar interaction Hamiltonian can cause transitions even in the presence of the tumbling motion of spins found in liquids. In fact, transitions can only be caused if the tumbling motion causes frequency components in the interaction at ω_0 or $2\omega_0$. The transitions occurring due to the non-secular terms of the dipole-dipole interaction Hamiltonian are shown in Figure 3.1.2.1. These transitions are caused by the thermal motions of the nuclei, and thus the transitions will occur most readily when the motion of the nuclei causes maximum interaction frequency components at or around ω_0 or $2\omega_0$.

3.1.2.2 Chemical shift.

The magnetic field experienced by the nucleus of an atom in a molecule is not normally the same as the magnetic field experienced by the nucleus in a free atom when both are subject to the same external field B_0. The variations in the field are caused by the electrons which surround the nucleus, and which cause either an increase or decrease in the experienced field. This effect is called shielding, and its extent depends on the molecule and position within that molecule at which the nucleus finds itself. In an NMR spectrum this shielding causes a shift in the peak corresponding to the free atomic nucleus, and different positions in a molecule can produce different peak positions [Bovey, 1969 p55]. This is the chemical shift, measured by dividing the shift in frequency of the peak by the peak frequency and expressing as parts per million (ppm). Table 3.1.2.1 indicates some of the chemical shifts observed in NMR spectroscopy, along with some values observed in *in vivo* NMR spectroscopy [Jardetzky and Roberts, 1981 p27].

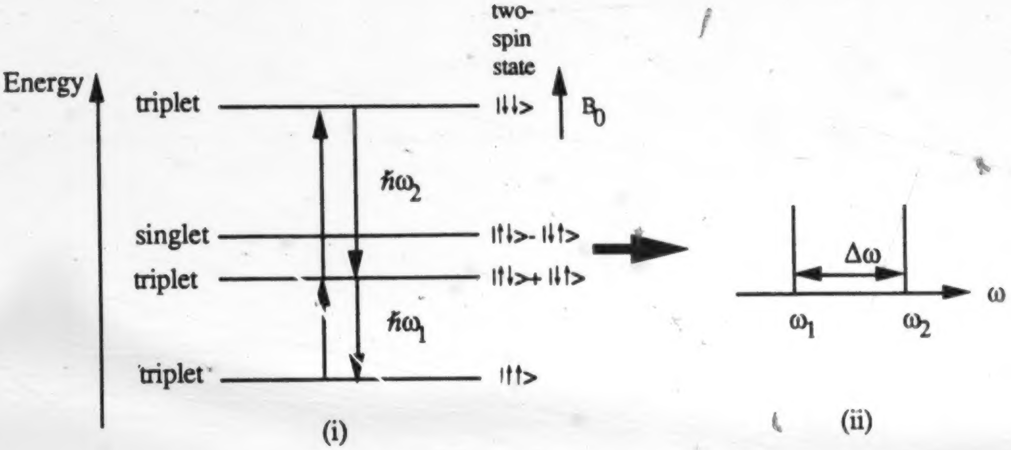
Energy
two-spin state
triplet
singlet
triplet
triplet
|↓↓>
|↑↓>- |↓↑>
|↑↓>+ |↓↑>
|↑↑>
B_0
$\hbar\omega_2$
$\hbar\omega_1$
$\Delta\omega$
ω
ω_1
ω_2
(i)
(ii)

(a) energy-level diagram (i) and resulting spectrum (ii) from the secular parts of the dipole-dipole interaction Hamiltonian.

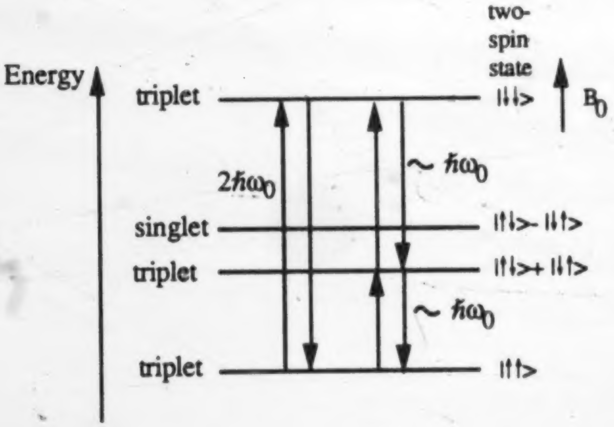
Energy
two-spin state
triplet
singlet
triplet
triplet
|↓↓>
|↑↓>- |↓↑>
|↑↓>+ |↓↑>
|↑↑>
B_0
$2\hbar\omega_0$
$\sim \hbar\omega_0$
$\sim \hbar\omega_0$

(b) energy-level diagram from the non-secular parts of the dipole-dipole interaction Hamiltonian.

Figure 3.1.2.1 Energy-level diagrams for two-spin system interacting by (a) secular and (b) non-secular terms of the dipole-dipole interaction Hamiltonian.

Nucleus	Chemical shift range (ppm) in high resolution spectra	Approximate chemical shift range (ppm) in *in vivo* spectra.
^{1}H	12	8
^{13}C	350	200
^{19}F	500	
^{31}P	700	30

Table 3.1.2.2 Chemical shifts observed in high-resolution and *in vivo* spectroscopy.

3.1.2.3 Scalar coupling.

Scalar, or spin-spin, coupling is, as its name suggests, independent of the direction of the interaction in the magnetic field, unlike dipolar-dipolar coupling in Section 3.1.2.1. The mechanism for scalar coupling is the spin pairing of each nucleus to electrons in bonds joining it to other nuclei [Jardetzky and Roberts, 1981 p37]. Two nuclei can thus interact through electron bonds, with the magnitude of the interaction dependent upon the number of electron bonds between them. This coupling can lead to complex splittings of peaks when nuclei are close together on a molecule. This splitting is of use to the chemist in the determination of chemical structure. By selectively irradiating particular peaks in the NMR spectrum, those nuclei can be spoiled from interacting by scalar coupling, and thus multiple peaks which are seen to change their splitting are known to be neighbours of the irradiated peak.

In the NMR spectrum, a peak is attributable to a single nucleus or group of magnetically equivalent nuclei. A nucleus or group of equivalent nuclei affected by a single neighbouring nucleus will produce a doublet. If the neighbour is a group of two equivalent nuclei, a triplet results. For example, an ethyl group (CH_2 - CH_3) will exhibit two peaks in a proton NMR spectrum, a quartet from the CH_2 group and a triplet from the CH_3 group.

The areas of the peaks in the multiplet follow a binomial sequence: 1:1 for a doublet, 1:2:1 for a triplet etc.. The spacing between the peaks is governed by the energy of the interaction, and is described by the parameter J, the scalar coupling constant.

3.1.3 Relaxation and its mechanisms.

The way that nuclei in liquids return to their equilibrium state following a perturbing RF pulse is characterized by their relaxation rates [Jardetzky and Roberts, 1981 p52]. There are two time constants for the nuclear relaxation: T_1 and T_2. The former is the spin-lattice relaxation time constant which is affected by thermal motion of molecules causing magnetic field fluctuations at the Larmor frequency ω_0 and $2\omega_0$. The latter, T_2, is the spin-spin relaxation time constant which is sensitive to low frequency fluctuations as well as those at ω_0 and $2\omega_0$.

T_1 reflects the rate at which the component of the magnetization parallel to the B_0 field, M_z, returns to its equilibrium value following a perturbation. T_2 describes the relaxation of the component of the magnetization perpendicular to the B_0 field. This transverse magnetization M_{xy} has an equilibrium value of zero and decays by the dephasing of spins due to B_0 inhomogeneity and coupling with other spins.

The dipole-dipole and possibly the anisotropic chemical shift interactions are responsible for T_1 and T_2 relaxation in biological systems, as these are the strongest interactions occurring [Fullerton, 1988 p37]. They are both mechanisms by which a fluctuating magnetic field can be induced at a nucleus by the motion of a neighbouring nucleus. In some non-viscous liquids T_1 and T_2 become equal.

The T_1 relaxation time can be understood from a semi-classical picture of the motion of the microscopic nuclear magnetic moments and the macroscopic magnetization. In this picture the z component of the magnetic moment parallel to the external magnetic field is quantized (for protons and phosphorus into two levels), while the magnetic moments are still viewed as vectors rotating about the B_0 direction. The relaxation of the magnetization following a 180^o pulse can be explained by quantum transitions of the spins, as shown in Figure 3.1.3.1.
The T_2 relaxation time cannot be as easily demonstrated using a semi-classical picture; for a true picture quantum mechanics needs to be used [Abragam, 1961 p305].

3.1.4 NMR spectra.

NMR spectra provide information about nuclei and their environments. As described in Section 3.1.2.2, the position of peaks is related to the position of nuclei on molecules. The splitting observed in peaks is defined by the neighbours of nuclei on molecules, as discussed in Section 3.1.2.3. The width of peaks is related to both the inhomogeneity of the external magnetic field and the T_2 relaxation rate. The shift of peaks, observed when other nuclei come into the neighbourhood of the nucleus under investigation, can be used as an indication of chemical concentrations and pH [Moon and Richards, 1973].

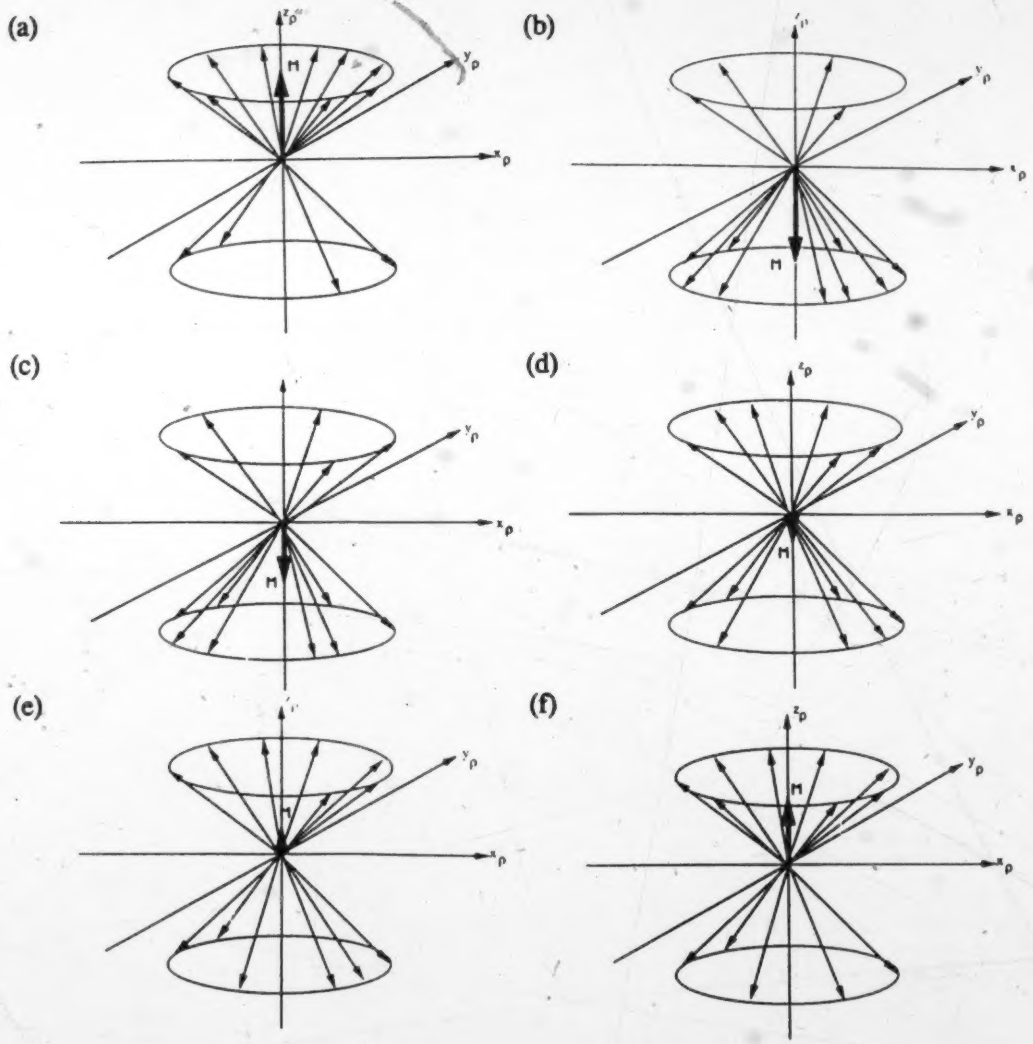
(a)
z_ρ
M
y_ρ
x_ρ
(b)
y_ρ
x_ρ
M
(c)
y_ρ
x_ρ
M
(d)
z_ρ
y_ρ
x_ρ
M
(e)
y_ρ
x_ρ
M
(f)
z_ρ
M
y_ρ
x_ρ

Figure 3.1.3.1 The relaxation of the macroscopic magnetization following a 180° pulse. In (a) the population of the two states is weighted towards the +z direction. After the 180° pulse (b) the populations are inverted. As spins undergo transitions back to their equilibrium values (c), (d), (e) and (f) the macroscopic magnetization is seen to relax back towards its equilibrium value in (a).

3.2 NMR techniques.

All NMR experiments use RF pulses to cause transitions of nuclear spins between spin states. The two principal RF pulse sequences used in NMR imaging and spectroscopy, 90°-acquire and spin-echo, are described in Section 3.2.1. NMR imaging using the spin-echo sequence is described in Section 3.2.2. When performing NMR spectroscopy it is usually necessary to define the region from which you wish to receive the NMR signal. Techniques for doing this are outlined in Section 3.2.3.

3.2.1 Pulse Sequences.

The simplest pulse sequence consists of a 90° pulse followed by a period of data acquisition during the free induction decay of the NMR signal as shown in Figure 3.2.1.1.

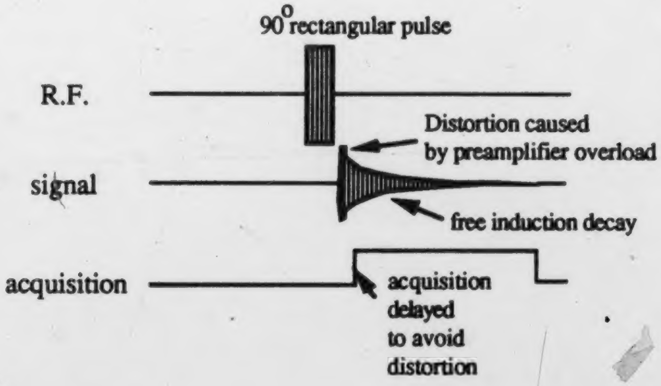

90° rectangular pulse
R.F.
Distortion caused by preamplifier overload
signal
free induction decay
acquisition
acquisition delayed to avoid distortion

Figure 3.2.1.1 90°-acquire pulse sequence.

The simple rectangular 90° pulse, which tips the macroscopic magnetization into the transverse plane, can be used to generate an NMR signal. The magnetization tip-angle caused by the pulse is governed by the product of the amplitude of the RF pulse and the duration of the pulse. A short pulse has a large bandwidth in the frequency domain and so is normally used in order that there be as little variation as possible in the excitation across the bandwidth required for the experiment . Generally the frequency spread must be greater than the width of the NMR spectrum expected in order to excite equally all the nuclei. A long pulse is sometimes used in order to selectively stimulate a particular peak in the NMR spectrum, as for example in solvent suppression.

When truly uniform excitation across some region of a spectrum and nowhere else is required, the RF pulse must be shaped in some way. A sinc-modulated RF pulse [Morris, 1988 p18] will give uniform excitation since its Fourier transform is a top-hat function. In this way the effect of the pulse is made independent of frequency.

When using a surface coil with an inhomogeneous field intensity another problem which arises is the variation of tip angle with position in the sample. This problem is overcome by the use of adiabatic pulses. Bendall and Pegg [1986] and Ugurbil, Garwood and Bendall [1987] have described pulses in which the magnitude of the RF pulse is modulated as a sine wave, while the frequency is swept also. The pulses show great tolerance to field inhomogeneity and are thus suitable for work with a surface coil.

Another problem with the 90^o-acquire sequence is that the NMR signal must be acquired immediately after the 90^o pulse, which often leads to distortion of the beginning of the free induction decay (FID) as the magnetization returns to its equilibrium value. Hahn [1950] found that, when a 90^o pulse was shortly followed by a 180° pulse, the spins which had dephased in the transverse plane after the 90° pulse could be rephased to give an echo signal which was not affected by the presence of a large RF pulse close to it (see Figure 3.2.1.2).

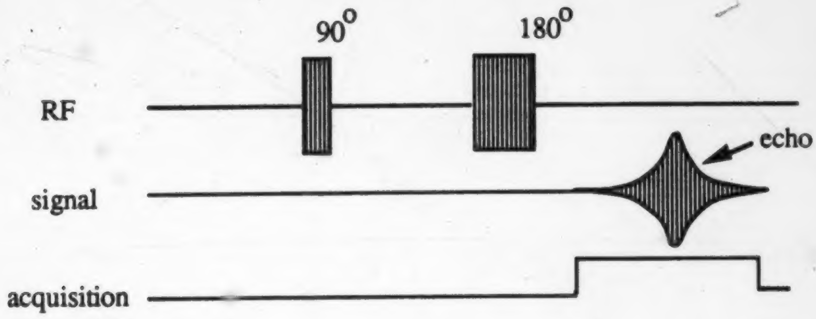

Figure 3.2.1.2 Spin-echo pulse sequence.

3.2.2 NMR Imaging.

The pulse sequences of Section 3.2.1 do not provide any information about the position within the sample from which the NMR signal originates. In order to do this, the external magnetic field B_0 must be modified by the use of field gradients. These gradients are produced by a set of gradient coils which are able to provide a linear change in the B_0 field with the three orthogonal Cartesian directions. These gradients cause the Larmor frequency to vary with position within the sample. A frequency-selective pulse, such as the sinc pulse, can thus be used to excite some selected region of the sample. One way to make an image is to destroy the signal from unwanted regions using oscillating gradients, and to move the point selected in this way through the image plane [Hinshaw,1974,1976]. However, the use of Fourier transforms enables the spatial information to be encoded into the NMR signal using switched gradients, and then later recovered by the Fourier transform. When a two-dimensional image is required, one gradient is used to localize the signal to a slice, and the other two are used to encode the spatial dependency of the sample into the NMR signal, and an image produced through the application of a two-dimensional Fourier transform. This type of two-dimensional Fourier transform imaging, or spin-warp imaging, was proposed by Hutchison's group [Edelstein *et al.*, 1980; Johnson *et al.*, 1983]. The principles of this technique and other imaging methods are covered in the literature [Ernst *et al.*, 1987 p554; Wehrli, 1988 p9; Hendrick, 1988 p67].

Two time parameters are important when performing imaging; T_E, the time between the 90° pulse and the echo (see Figure 3.2.1.2), and T_R, the time between repeated spin echo sequences. Decreasing or increasing T_E can be used to emphasize or suppress the signal from tissue with a particular T_2 relaxation time respectively. T_R should be sufficient to allow the spins to return to their equilibrium state between excitation, and should thus be greater than T_1. During T_R, when the spins in one image slice are relaxing, another image slice can be selected and excited. In this way many images can be taken in the time that it takes to make one image. This is the principle of multi-slice imaging used in this study, in which 6 images were taken simultaneously, with $T_E = 50$ ms and $T_R = 580$ ms.

3.2.3 Spatial localization.

There are many techniques available to the spectroscopist for spatial localization. Among them are depth-pulse localization [Bendall and Gordon,1983], SPARS (SPAtially Resolved Spectroscopy) [Luyten and den Hollander, 1986], STEAM (STimulated-Echo Acquisition Mode) [Haas and Frahm, 1985] and VSE (Volume-Selective Excitation) [Garroway, Grannel and Mansfield, 1974, Aue et al, 1984]. However, the technique which is used in this work is called ISIS, an acronym for Image-Selected *In vivo* Spectroscopy.

3.2.3.1 Image-selected *in vivo* spectroscopy (ISIS)

The ISIS technique developed from a one-dimensional localization technique suggested by Tycko and Pines [1984]. Ordidge, Connelly and Lohman [1986] used a hyperbolic secant pulse in combination with a gradient to selectively invert the spins in one slice of the sample. When this inversion is performed before the 90° pulse in an experiment, the FID resulting will contain a positive contribution from spins outside the slice, and a negative contribution from spins within the slice. When two experiments are performed, one with the inversion pulse and one without, the FIDs can be combined to cancel the signal from the spins outside the slice, leaving only the signal from within the slice, as shown in Figure 3.2.3.1.

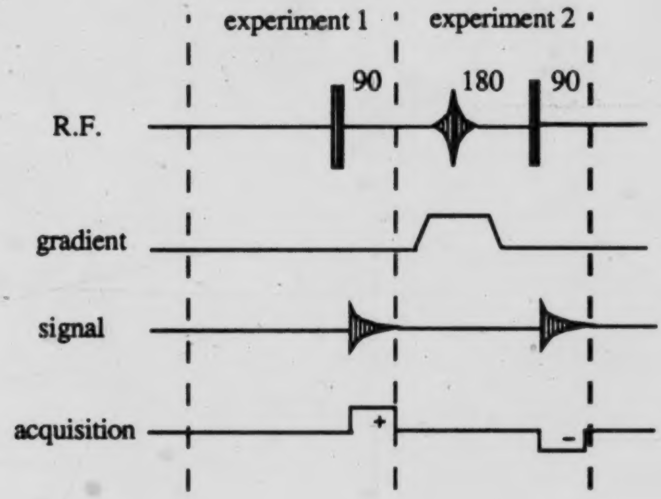

Figure 3.2.3.1 A one-dimensional ISIS experiment.

Note that this technique relies on good repeatability of the experiment for cancellation of the signal from the unselected region and good definition of the selected region by the inversion pulse. Also note that the signals in steps 1 and 2 are considerably larger than those after subtraction, requiring good dynamic range in the receiver.

Three-dimensional ISIS requires eight experiments in order to subtract out the signal from the unselected region. This is done with gradients and selective inversion pulses as shown in Figure 3.2.3.2.

One source of artefact signals in spectra obtained using the ISIS technique is the subtraction error which occurs when subtracting out the volumes from which signals are not required. Subtraction errors are caused by the volume-selection pulse failing to excite all the selected volume equally in the different experiments in the sequence and T_1 relaxation during the interpulse delays. If the subtraction is not perfect there will be a signal coming from these outer volumes, which will be indistinguishable from the signal obtained from the volume selected. This problem is acute when the sample volume is large, and the localized volume small, since a 0.1% error in a one-litre-volume subtraction could result in a signal comparable with a 1 cm^3 localized volume.

3.3 The NMR spectrometer

The NMR spectrometer takes several forms, depending on whether it is being used to probe molecular structure, study biology *in vitro* or diagnose human ailments. The structure of the instrument remains similar, however, and is described in Section 3.3.1. The instrument used in this study is described in Section 3.3.2.

3.3.1 Introduction to the instrument.

The basic pulsed NMR spectrometer consists of a radio-frequency (RF) oscillator, gated to produce short pulses of RF signal, which are amplified by an

RF amplifier to give B_1 fields of the order of 0.01 T across a sample placed in a very

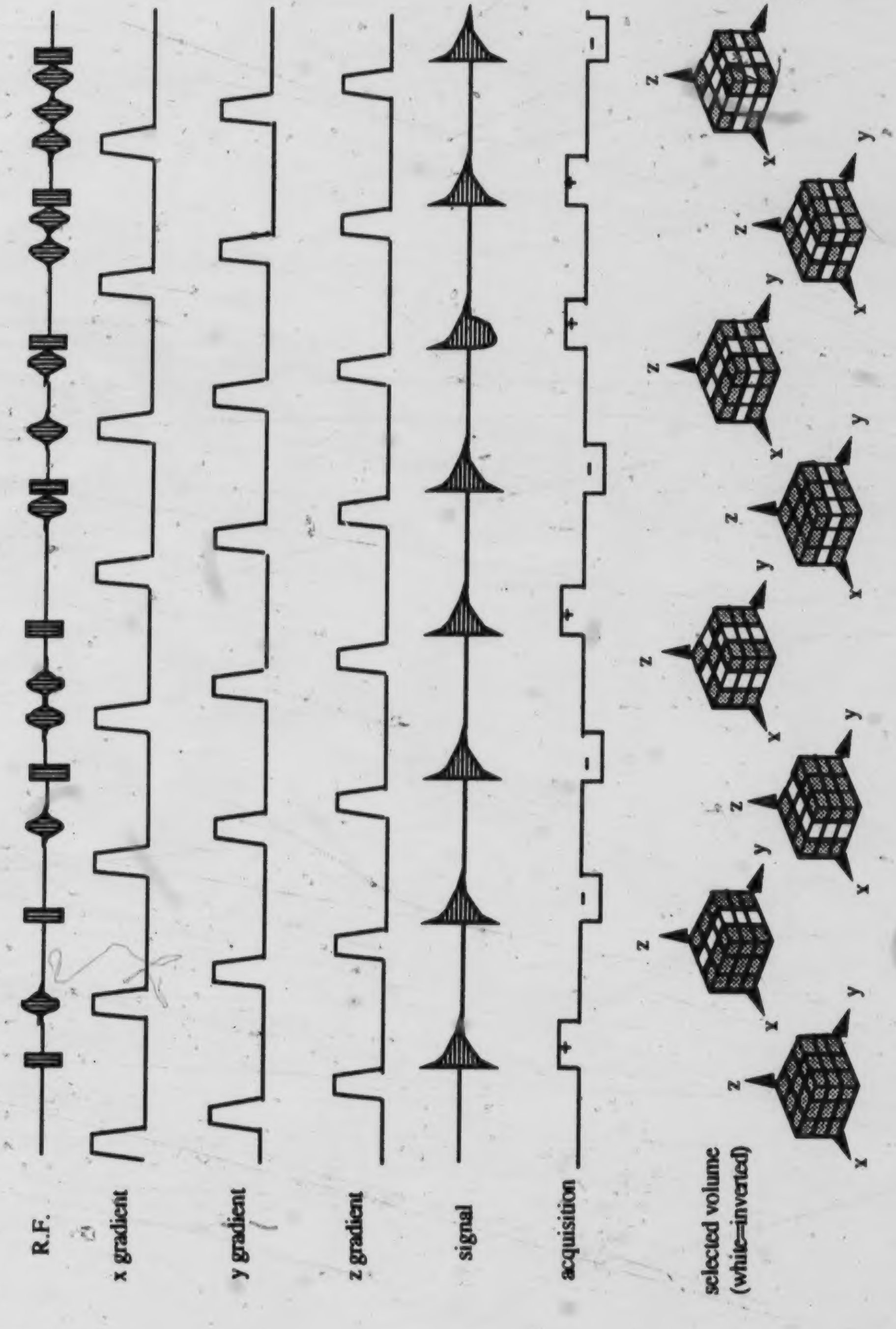
R.F.
x gradient
y gradient
z gradient
signal
acquisition
selected volume
(white=inverted)
+
-
x
y
z

Figure 3.2.3.2 Three dimensional ISIS localization sequence.

constant B_0 magnetic field in the range 0.25-5 T. Two separate coils act as transmitter and receiver, and the received signal is detected in a phase-sensitive detector (PSD) with reference to the phase of the RF oscillator. The two outputs from the PSD are converted to digital signals in two analogue-to-digital converters (ADC), and form the real and imaginary parts of the time-domain data, which are converted to frequency data by a Fourier transform performed by computer. The synchronization of the transmitter pulses and data collection is performed by the pulse programmer. Figure 3.3.1.1 shows a block diagram of a basic pulsed NMR spectrometer.

The transmitter and receiver parts of the circuit must be kept separate and isolated so that there is no leakage of the high power RF signal into the receiver, since this would be interpreted as a signal by the receiver, and thus give erroneous spectra.

The requirements for the parts of a pulsed NMR spectrometer are described in detail in Farrar and Becker [1971 p36].

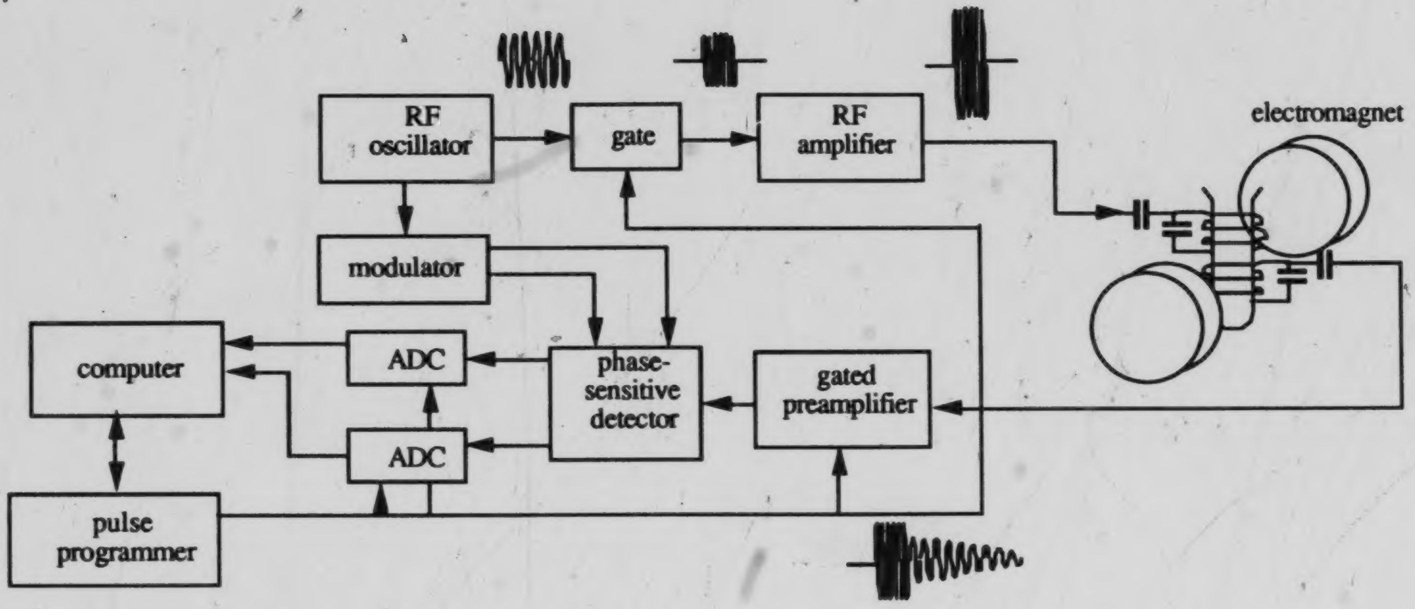
RF oscillator
gate
RF amplifier
electromagnet
modulator
computer
ADC
phase-sensitive detector
gated preamplifier
ADC
pulse programmer

Figure 3.3.1.1 Block diagram of a basic pulsed NMR spectrometer.

3.3.2 The Philips Gyroscan spectrometer.

The Philips Gyroscan spectrometer was designed primarily for routine clinical diagnostic proton imaging at 1.5 Tesla. It contains a superconducting magnet with a bore of 68 cm after insertion of the gradient and shim coils. The computer is a VAX 11/750, which has an AP500 array processor to increase its throughput (see Figure 3.3.2.1). Up to 2000 images can be stored on disk. Images can be made using many sequences, including spin-echo and inversion recovery. The minimum slice thickness is 2 mm and the minimum pixel size is 0.15 x 0.15 mm when performing a 512 x 512 image at a field of view of 80 mm.

The patient-handling system consists of a motorized patient table which can be raised and lowered as well as translated to move the patient into the bore of the magnet. Light beams assist in accurate patient positioning, and an automatic system moves the part of the patient marked with the light beam to the centre of the magnet.

Automatic tuning and matching of the head and body coils reduces preparation time. The bore of the body coil is 50 cm, and of the head coil 32 cm.

The Philips Gyroscan system contains a spectroscopy package, but spectroscopy in the Clinical NMR Unit of the University of Alberta is normally performed using the LACTATE program designed by Dr.C.H.Hanstock, and implemented by Mr.D.Georghiu, both of the Dept. of Applied Sciences in Medicine of the University of Alberta. This program is very flexible, and can be used to construct a great many pulse sequences.

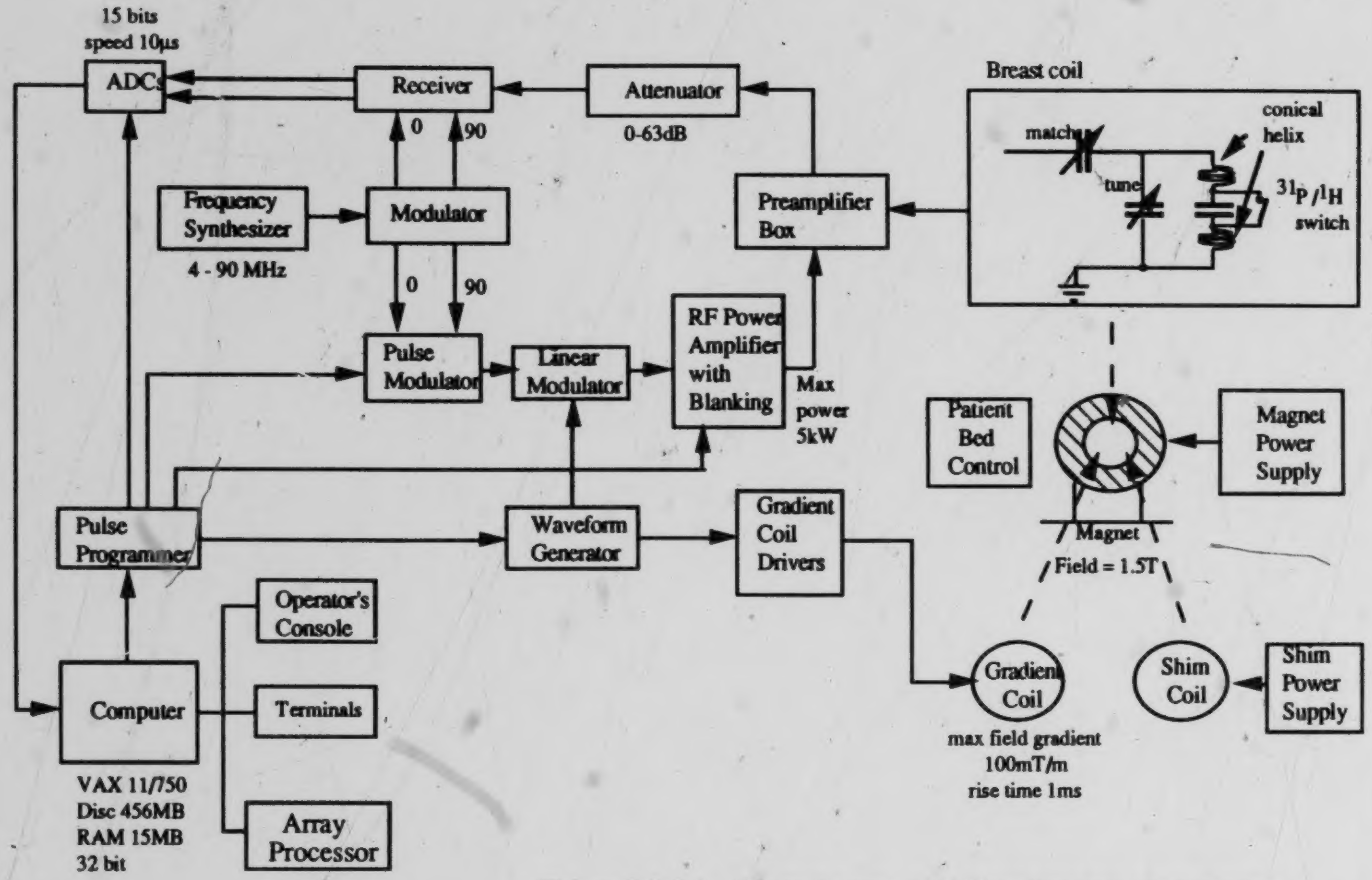
15 bits
speed 10µs
ADCs
Receiver
Attenuator
0-63dB
Breast coil
match
tune
conical
helix
31P/1H
switch
0
90
Frequency Synthesizer
4 - 90 MHz
Modulator
Preamplifier Box
0
90
Pulse Modulator
Linear Modulator
RF Power Amplifier with Blanking
Max
power
5kW
Patient Bed Control
Magnet Power Supply
Magnet
Field = 1.5T
Pulse Programmer
Waveform Generator
Gradient Coil Drivers
Operator's Console
Computer
Terminals
Array Processor
VAX 11/750
Disc 456MB
RAM 15MB
32 bit
Gradient Coil
max field gradient
100mT/m
rise time 1ms
Shim Coil
Shim Power Supply

Figure 3.3.2.1 Block diagram of Philips Gyroscan spectrometer.

CHAPTER 4

APPROACHES TO NMR SURFACE COIL DESIGN

The surface coil is in general use in the imaging and spectroscopy of superficial parts of the body, such as the knee, calf muscle, spine, temporomandibular joint, eye and breast. In this chapter some different aspects and approaches to NMR surface coil design are brought together, and these lead into the detailed design methods described in Chapters 5 and 6.

4.1 Introduction.

4.1.1 The purpose of the surface coil.

The amplitude of the NMR signal from some small region in the sample is given by

$$\text{signal amplitude} \propto Q\,\omega_0 \frac{B}{I}. \qquad (4 - 1)$$

in which Q is the quality factor of the NMR coil , ω_0 is the resonant frequency of the coil and B/I is the coil sensitivity [Hoult and Richards, 1976] given by the ratio of local flux density (B) to the current flowing in the coil (I) to produce it.

The resonant frequency of the coil is matched to the Larmor frequency of the nuclei, and is thus fixed for a particular magnetic field. The coil sensitivity decreases generally with distance from the wire used to make the coil, so the maximum signal is obtained from a high Q surface coil as close as possible to the sample under investigation. The Q of a parallel LC circuit, with inductance L having resistance R, tuned to frequency ω_0 is

$$Q = \frac{\omega_0 L}{R},$$

so for high Q a coil should have a large inductance and a small internal resistance.

For the case of the human body, imaging is normally performed with a saddle coil wrapped on a cylinder of diameter approximately 60 cm. At the centre of the coil B/I is low, and where a high signal-to-noise ratio is required, as in high resolution imaging or spectroscopy, a surface coil is preferred. The high signal-to-noise ratio provides images of higher resolution, or shorter acquisition times in imaging. In spectroscopy a high signal-to-noise ratio gives either better defined spectra or shorter acquisition times.

4.1.2 Some practical surface-coil design considerations.

Equation (4-1) demonstrates that a large signal can be obtained from an NMR experiment if the Q of the coil is high, a large B_0 field is used and the coil is highly sensitive. However, in practice there are constraints limiting the maximum signal obtainable with a surface coil. In this section some of these constraints are listed.

1) Optimally the surface coil should surround the sample in order to maximise the coil sensitivity. Where this is not possible the coil should be close to the sample. How this is achieved in the case of the breast coil is described in Section 6.3.
2) The high quality factor requirement indicates the use of a high-inductance coil made of low-resistance wire, such as large diameter silver wire.
3) The coil must be tunable to the Larmor frequency of the nuclei, and thus must have a variable capacitor connected in parallel with it (see Figure 3.3.2.1). Since practically tuning capacitors and their leads cannot be made with capacitances less than about 0.5 pF at usual NMR frequencies, this places a maximum limit on the coil inductance.

4) The coil should be matched to the coaxial cable connecting it to the pre-amplifier (see Figure 3.3.2.1). This imposes a further restriction on the inductance of the coil.
5) With high voltages being present on the coil during an experiment, all parts of the coil and matching circuit must be well isolated electrically from the patient.
6) If the patient is to lie in the NMR spectrometer for a long time, the coil should be as comfortable as possible for the patient.
7) The coil sensitivity should be uniform over the sample, so that the signal is received equally from all parts of the sample. This is not normally achievable with a surface coil, but the field may be made homogeneous over a portion of the sample (see Figures 5.5.3 and 8.4.2 for the breast coil).
8) The signal-to-noise ratio should be as high as possible. This is considered in Section 4.5.

Some of considerations above are mutually exclusive, so surface coil design is necessarily a compromise.

4.2 The Biot-Savart law

The magnetic field from an infinitely thin current-carrying wire may be calculated using the Biot-Savart law [Lorrain, Corson and Lorrain, 1987 p327]. This law relates the magnetic flux density to the current flowing in the wire and the geometry of the coil.

$$\mathbf{B}(\mathbf{r}) = \frac{\mu_0 I}{4\pi} \int_{\text{wire}} \frac{d\mathbf{l} \times (\mathbf{r}-\mathbf{f})}{|\mathbf{r}-\mathbf{f}|^3} \qquad \text{(SI units)}$$

in which the wire extends from A to B, has a current I flowing in it, **r** is the vector from the origin to the point where the magnetic flux density is to be measured, **f** is the vector from the origin to the centre of the wire element **dl** as shown in Figure 4.2.1.

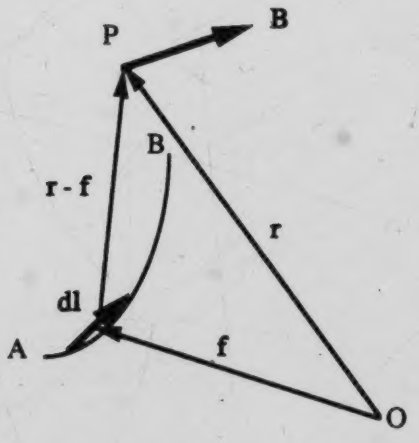

Figure 4.2.1. Variables used in the Biot-Savart equation.

For simple geometries the magnetic flux density is found analytically, but for cases when the coil is difficult to describe algebraically, or when the coil is located asymmetrically with the chosen coordinate system, the analytical method is very involved. As an example, for a simple circular coil in the xz plane with its centre at the origin, the on-axis magnetic flux density is found [Lorrain, Corson and Lorrain, 1987 p331] to be

$$B_y = \frac{\mu_o I a^2}{2(a^2+y^2)^{3/2}} \text{, along the y-axis.}$$

This function is shown in Figure 4.2.2.

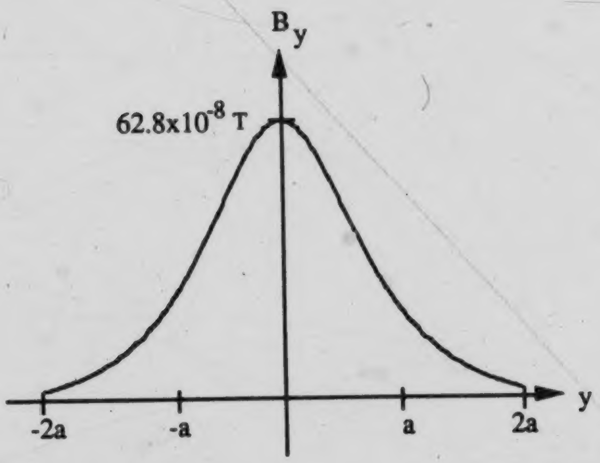

Figure 4.2.2 The axial field along the axis of a circular coil radius a = 1 m, carrying a current of 1 A.

4.3 Numerical integration

The fields from coils may be calculated using the Biot-Savart law and numerical integration. The field from an arbitrary current loop can be calculated by splitting up the loop into a series of short straight elements and summing the resulting fields at some point (Figure 4.3.1).

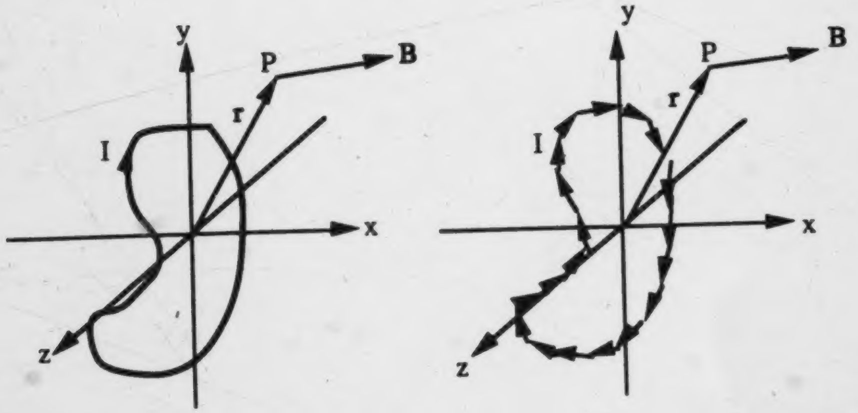

Figure 4.3.1 Dividing a current loop (a) into linear elements (b) to calculate the flux density **B** at point P.

The following theory is used to calculate the field from each segment.

Consider a straight length of wire AB (with geometry as depicted in Figure 4.3.2), from which we calculate the field **B** at P, in coordinates with origin at O.

Then, $$\mathbf{B} = \frac{\mu_o}{4\pi} I_{AB} \int_A^B \frac{\mathbf{dl} \times \mathbf{r}}{r^3} = \hat{e}_\perp \frac{\mu_o}{4\pi} I_{AB} \int_{\phi_1}^{\phi_2} \frac{r^2 \, d\phi}{r^3}$$

in which ϕ is the angle between the perpendicular from the point P to the line AB and the line from the wire segment **dl** to the point P.

However, $\cos\phi = \rho/r$, so $$\mathbf{B} = \hat{e}_\perp \frac{\mu_o}{4\pi} \frac{I_{AB}}{\rho} \int_{\phi_1}^{\phi_2} \cos\phi \, d\phi = \hat{e}_\perp \frac{\mu_o}{4\pi} \frac{I_{AB}}{\rho} (\sin\phi_1 - \sin\phi_2)$$

where $\hat{e}_\perp$ is the unit vector perpendicular to the plane of **r** and **dl**.

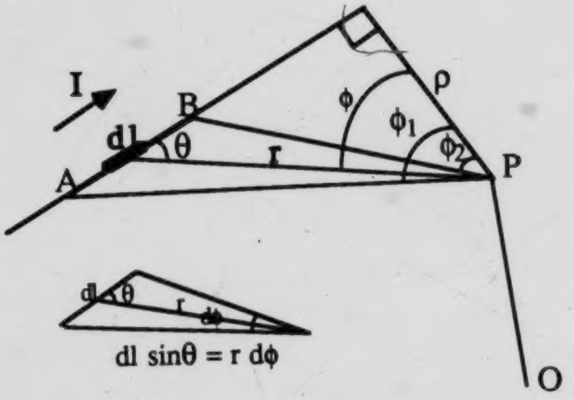

Figure 4.3.2 Geometry for calculating the magnetic field due to a straight wire segment.

In this way the problem of calculating the field due to a piece of straight wire with a current flowing through it is reduced to finding the angles of different points on the wire relative to the line perpendicular to the wire through the point where we wish to calculate the field. The fields at a number of points (e.g. 1600 for the field plot in Figure 6.2.3) are calculated for each line segment in turn, and the total field accumulated as the line segment is moved along the line. Each line segment is further divided into sub-segments for the purposes of the calculation using the method above. The breast coil design in Chapter 6 uses this method to calculate the field.

4.4 Spherical harmonic analysis.

Another method which can be used to design a surface coil is to use an analytic description of the field in terms of the coil parameters. The advantages of this method would be that the coil field could be optimized algebraically. To express the vector field of the flux density **B** in terms of the coil parameters is complex, so it is usual to find a scalar field to express. Romeo and Hoult [1984] have used the magnetic scalar potential (V) from a circular coil and expanded it in a series of spherical harmonics, whereas Turner [1986] has used an expansion of the axial component of the flux density (B_z) from a current distribution flowing on the surface of a cylinder in terms of the modified Bessel functions. Romeo and Hoult were also mainly concerned with B_z, but the magnetic scalar potential can be differentiated to give other components of the flux density, such as B_r and B_θ. The spherical harmonic method is thus suitable for use with surface coils.

4.4.1 Resolution of a magnetic field into spherical harmonic components.

Any scalar magnetic potential may be expressed in terms of spherical harmonics, which have three separable parts in spherical coordinates. The radial dependency is a power of the distance from the origin, the azimuthal dependency is a Legendre function and the polar dependency is a cosine or sine function. If the coil is symmetrical about the axis of symmetry of the coordinate system then the field is also symmetrical, and there is no polar dependency term, which makes the spherical harmonic expansion simpler.

The magnetic scalar potential expansion generally has two distinct regions, with different boundary conditions. In the region far from the coil the potential must go to zero as the radial ordinate (r) increases, and thus there are only terms in r^{-n}. Close to the coil centre the scalar magnetic potential goes to a constant value, so for a coil centered at the origin there are only terms in r^n.

4.4.2 Field design using spherical harmonic analysis.

Romeo and Hoult [1984] have used the spherical harmonic expansion for designing coil systems for NMR field shimming. This has been possible because the regions they have considered, near the origin, have all been in the parts of the field in which the spherical harmonic series of the individual loops are converging (terms in r^n as $r \rightarrow 0$). Similarly it is possible to design coil systems with particular spherical harmonic components far from the coils. However, when the distance from the origin is of the order of the distance of the coil wire from the origin, the series do not converge, and it is very difficult to design coil geometries for a particular scalar potential. Spherical harmonic expansions are described in more detail in Chapter 5.

4.5 Signal-to-noise ratio

The signal-to-noise ratio (SNR) of a circular surface coil which is in close contact with a lossy conducting sample on one side, and which has nothing on its other side is considered in this section. This enables the calculation of an optimal size for a circular coil to be determined for use at a particular depth. The expression for the signal comes from Hoult and Richards [1976] and that for the noise from Harpen [1987].

Consider a volume V_s in a conducting sample located at a depth y from a circular surface coil, and along its axis, as shown in Figure 4.5.1.

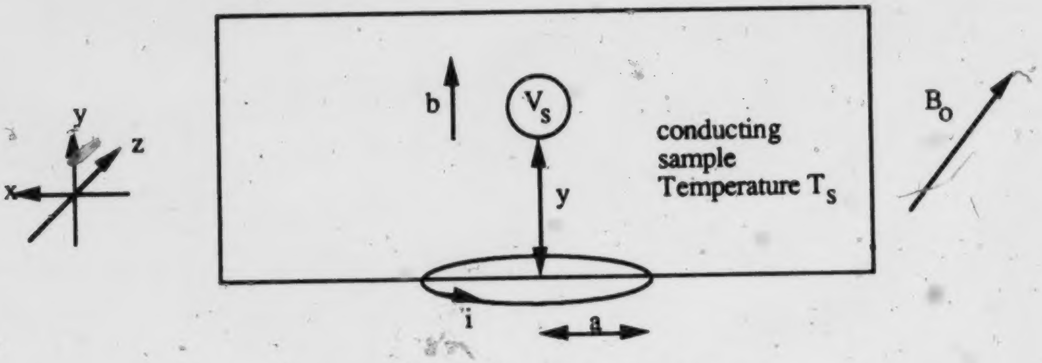

Figure 4.5.1 The surface coil geometry .

The rms voltage induced in the coil by the oscillating magnetization in the volume V_s is given [Hoult and Richards, 1976] by

$$\xi \propto \frac{\omega_0^2 b V_s N}{T_s} \qquad (4 - 2)$$

in which, ω_0 is the Larmor frequency, b is the xy-plane component of the field produced at V_s by unit current in the coil, N is the number of magnetic moments per unit volume, T_s is the sample temperature and a the coil radius.This voltage is plotted in Figure 4.5.2 as a function of coil radius.

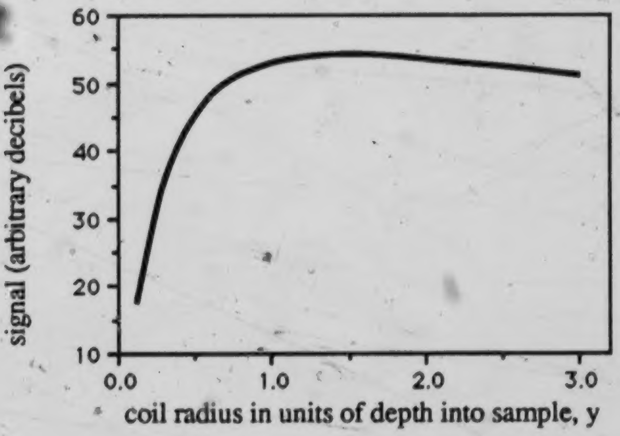

Figure 4.5.2 Signal from a circular surface coil

The noise induced in a circular surface coil by temperature fluctuations in the conducting sample is given by [Harpen, 1987]

$$\text{noise} \propto \omega_0 \sqrt{T_s a^3} \qquad (4 - 3)$$

The signal-to-noise ratio of the experiment which is localizing to the volume V_s is thus given by dividing (4 - 2) by (4 - 3), to give

$$\mathrm{SNR} \propto \frac{\omega_0 b V_s N}{\sqrt{T_s^3 a^3}} \qquad (4 - 4)$$

Now for a circular surface coil the on-axis magnetic field is given by

$$\mathrm{B} = \frac{\mu_0 i a^2}{2(y^2+a^2)^{3/2}} \hat{e}_y \qquad (4 - 5)$$

where $\hat{e}_y$ is perpendicular to the plane of the coil and i is the current flowing in the coil.

Substituting (4 - 5) in (4 - 4) gives a relation for the SNR of the circular surface coil.

$$\mathrm{SNR} \propto \frac{\omega_0 a^2 N V_s}{\sqrt{T_s^3 a^3}\,(y^2+a^2)^{3/2}} \qquad (4 - 6)$$

Now, if the depth of the localized volume, y, is kept constant whilst the radius of the coil is varied, a graph of SNR against a can be plotted, as shown in Figure 4.5.3, which exhibits a peak at coil radius of about 0.5 y.

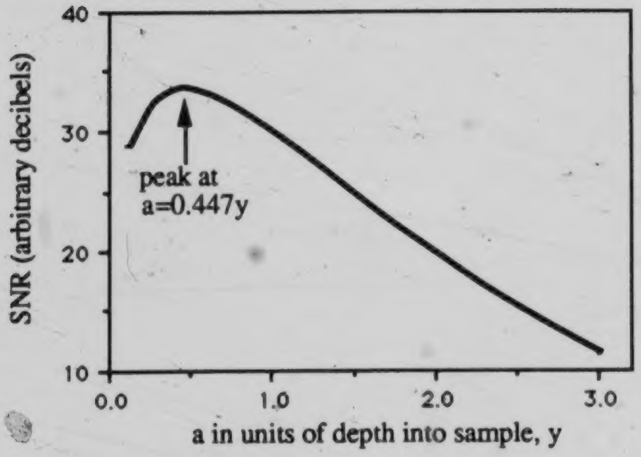

Figure 4.5.3 SNR of circular surface coil as a function of coil radius

Equation (4 - 6) can be differentiated with respect to a to find the position of the peak, giving

$$\frac{d(SNR)}{da} \propto \frac{(1/2(y^2+a^2)-3a^2)}{a^{1/2}(y^2+a^2)^{5/2}}.$$

Hence for max SNR,

$$\frac{d(SNR)}{da} = 0, \text{ or } \; y^2 - 5a^2 = 0,$$

which gives $a = 0.447y$, showing that the best SNR for a circular surface coil is found when the localized volume is at a depth slightly larger than the diameter of the coil.

A similar calculation could be performed for other coil geometries to find the optimal coil size.

CHAPTER 5

A MATHEMATICAL ANALYSIS OF THE MAGNETIC FIELD FROM CIRCULAR COILS.

Decomposition of a magnetic field into the coefficients of an orthogonal series of functions is one method that can be used for the design of coil geometries. Turner [1986] has described the use of Fourier-Bessel functions in the design of gradient coils for the NMR spectrometer. Romeo and Hoult [1984] have described a decomposition in terms of spherical harmonics for a similar purpose. They were mostly concerned with the component of the magnetic field in the direction of the B_0 field. This analysis in spherical harmonics extends their work. In the case of magnetic fields, the use of this description facilitates the design of multicoil systems with particular field distributions.

The purpose of this chapter is to use spherical harmonics in a description of the magnetic scalar potential from a circular coil, and hence of the components B_r and B_θ of the magnetic flux density. This analysis is then used to calculate the field from a composite system of three circular coils, approximating the breast coil described in Chapter 6.

5.1 Introduction

The spherical harmonics are a set of orthogonal functions which can be used as a basis for the description of a cylindrically symmetric three-dimensional function. They are closely related to the Legendre functions, which are described here first.

5.1.1 The Legendre polynomials

The Legendre polynomials $P_n(x)$ form a set of polynomials which are orthogonal over the interval $x = 1$ to $x = -1$. They are increasingly complex with increasing n; the first few are

$$\begin{array}{ll} P_0(x) = 1 & P_3(x) = \frac{1}{2}(5x^3 - 3x) \\ P_1(x) = x & P_4(x) = \frac{1}{8}(35x^4 - 30x^2 + 3) \qquad (5 - 1) \\ P_2(x) = \frac{1}{2}(3x^2 - 1) & P_5(x) = \frac{1}{8}(63x^5 - 70x^3 + 15x) \end{array}$$

It is important to note that the value of $P_n(x)$ is bounded by 1 and -1.

The fact that Legendre polynomials are orthogonal over the interval $x = 1$ to $x = -1$ makes them suitable for use in cylindrically symmetric systems, since x may be replaced by $\cos\theta$, and the orthogonality is now over the interval $\theta = 0$ to $\theta = \pi$.

When x in the the Legendre polynomials is replaced with $\cos\theta$, the Legendre functions are formed, as shown in Figure 5.1.1.1 over the interval $\theta = 0$ to $\theta = \pi$. Note that they consist of even and odd functions of θ with respect to $\theta = \pi/2$. In contrast, $\sin N\theta$ and $\cos N\theta$ are respectively odd and even functions of θ, and so both must be used to represent an arbitrary function, as in Fourier analysis.

The Associated Legendre functions, used in the analysis of the B_θ field later in this chapter, are generated from the Legendre functions by

$$P_n^m(\cos\theta) = (1-\cos^2\theta)^{m/2} \frac{d^m}{d(\cos\theta)^m} P_n(\cos\theta) \qquad (5 - 2)$$

The Associated Legendre functions are also orthogonal over the interval $x = -1$ to $x = 1$, but their value is no longer bounded by 1 and -1. Any function can be

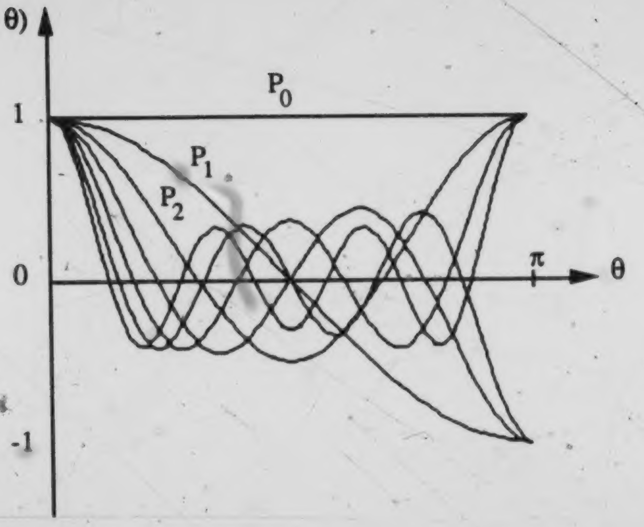

Figure 5.1.1.1 Zeroth-order Legendre functions n = 0 to 6.

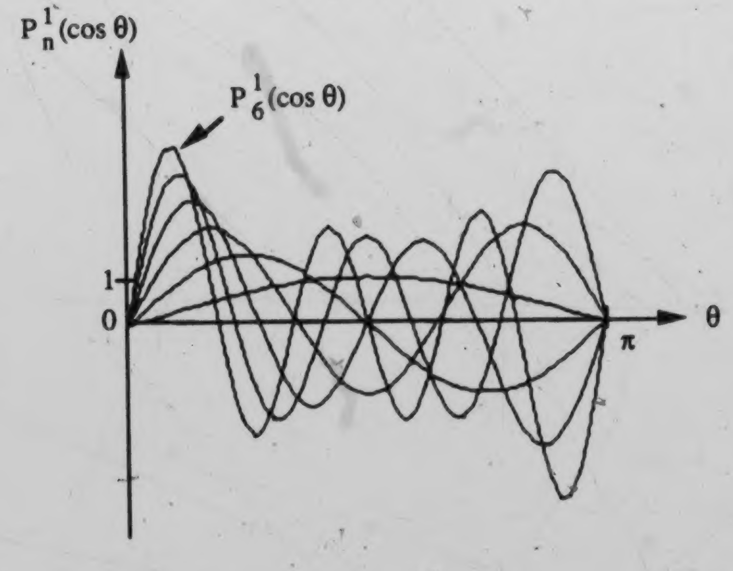

Figure 5.1.1.2 First-order Associated Legendre functions n = 1 to 6.

expressed in terms of Associated Legendre functions. Some of the Associated Legendre functions are shown in Figure 5.1.1.2.

Legendre polynomials can be used for fitting a polynomial to a function. They have the orthogonality conditions,

$$\int_{-1}^{1} P_n(x)P_m(x)dx \;\left|\; \begin{array}{l} = 0 \text{ for } n \neq m \\ \\ = \dfrac{2}{(2n+1)} \text{ for } n = m \end{array}\right. \qquad (5 - 3)$$

Any function y of x can be written $y = \sum_{n=0}^{\infty} A_n P_n(x)$, (5 - 4)

the coefficients A_n being found by evaluating

$$A_n = \frac{(2n+1)}{2} \int_{-1}^{1} y\,P_n(x)\,dx \qquad (5 - 5)$$

This technique enables a finite polynomial series to be fitted to a function $y = f(x)$ over the interval $x = -1$ to $x = 1$ without the iteration normally required by polynomial fitting methods. Equation (5 - 5) demonstrates that multiplication of the function by the appropriate Legendre polynomial and integration over the interval $x = -1$ to $x = 1$ is all that is necessary to find the coefficients of the polynomials of (5 - 1) in the expansion (5 - 4). This is easily performed by computer. An example is shown in Figure 5.1.1.3.

The Legendre polynomials used in this thesis to verify and illustrate the theory were generated by microcomputer. The program was written in Pascal, and is given in Appendix F. Tests on the accuracy of the Legendre functions by comparing them with tabulated values [Abramowicz and Stegun, 1965] showed differences of less than 0.0001%, as demonstrated in Table 5.1.1.1.

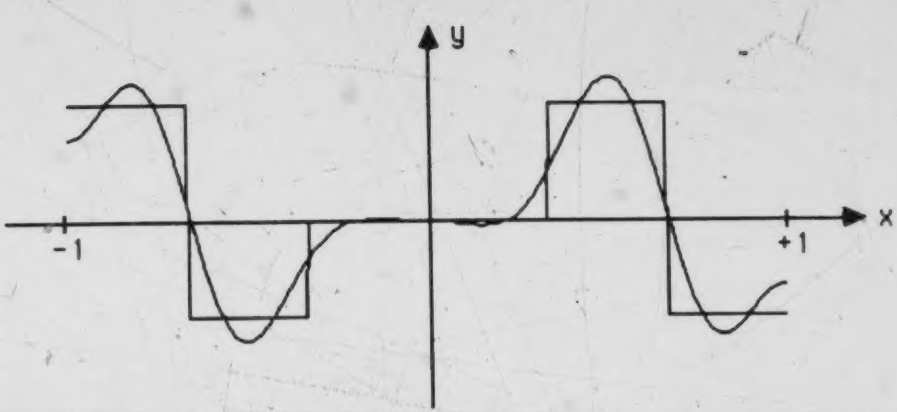

Figure 5.1.1.3 Example of a curve fit using Legendre polynomials, in this case 12 terms of the series $y = \sum_{n=0}^{\infty} A_n P_n(x)$.

Legendre polynomial	Value by microcomputer algorithm (A)	Value from Abramowicz and Stegun [1965] (B)	difference = |A-B|
$P_2(0)$	-0.50000000000000	-0.50000	0
$P_3(0)$	-0.00000011324685	0.0000000	1×10^{-7}
$P_9(0)$	0.00000018579561	0.00000000	2×10^{-7}
$P_{10}(0)$	-0.24609375000000	-0.2460937	5×10^{-8}
$P_2(0.2)$	-0.43999999761581	-0.44000	3×10^{-9}
$P_3(0.2)$	-0.28000000119209	-0.2800000	1×10^{-9}
$P_9(0.2)$	0.24595710635185	0.24595712	1×10^{-8}
$P_{10}(0.2)$	0.12907205522060	0.1290720	5×10^{-8}
$P_2(0.7)$	0.23500010371208	0.23500	1×10^{-7}
$P_3(0.7)$	-0.19249984622002	-0.1925000	2×10^{-7}
$P_9(0.7)$	0.27206057310104	0.2720599	6×10^{-7}
$P_{10}(0.7)$	0.08580575138330	0.0859058	5×10^{-8}

Table 5.1.1.1 Comparison of the values of Legendre polynomials calculated in MacPascal on the Macintosh microcomputer with those from a mathematical handbook [Abramowicz and Stegun, 1965]

5.1.2 The Spherical Harmonics

The spherical harmonics are closely related to Legendre functions, and include both azimuthal angle ($\emptyset$) and radial (r) dependence in addition to the polar (θ) dependence of the Legendre functions when used to represent a three-dimensional function in spherical coordinates. They have the form

$$T_{nm} = C_{nm} \binom{r^n}{r^{-n-1}} P_n^m(\cos\theta) \left(\begin{matrix}\sin\\ \cos\end{matrix} m\emptyset\right) \qquad (5 - 6)$$

where C_{nm} are constant coefficients.

Spherical harmonics in powers of r^n or r^{-n-1} are chosen if T_{nm} must be finite at $r = 0$ or as $r \to \infty$ respectively.

5.2 A circular coil centered on the origin.

The scalar potential for a circular coil centered on the origin is found by expanding it in terms of a series of spherical harmonics, and then including boundary conditions. The geometry of the derivation is shown in Figure 5.2.1. Since the coil is symmetrical under rotation about the y axis there is no azimuthal dependence.

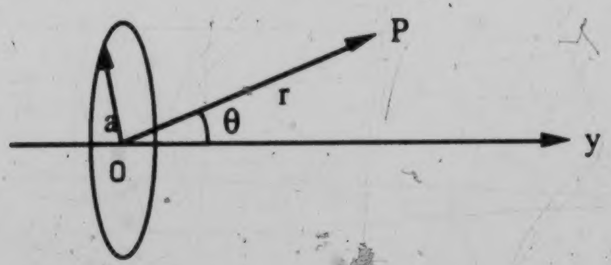

Figure 5.2.1 Definition of coordinates used in the derivation of the field from a circular coil centered at the origin.

A general solution of Laplace's equation $\nabla^2 V = 0$ for the scalar potential is

$$V_m = \sum_{n=0}^{\infty} A_n P_n(\cos\theta)\, r^n + \sum_{n=0}^{\infty} \frac{B_n P_n(\cos\theta)}{r^{n+1}}, \ -\pi/2 < \theta < \pi/2. \quad (5 - 7)$$

Now, for any point on the y axis, the scalar potential due to the circular surface coil is simply [Edminster, 1979]

$$V_m = \frac{\mu_0 I}{2}\left[1 - \frac{r}{\sqrt{a^2+r^2}}\right], \ \theta = 0, \ r \geq 0 \qquad (5 - 8)$$

This can be expanded in two ways to give powers of r^{-n} or powers of r^n, and these are used for the ranges $r \geq a$ and $r \leq a$ respectively.

$$\text{for } r \geq a,\ \theta = 0,\ V_m = \frac{\mu_0 I}{2}\left(\frac{a^2}{2r^2} - \frac{3a^5}{8r^4} + \frac{5a^6}{16r^6} - \ldots\ldots\right)$$

$$= \frac{-\mu_0 I}{2} \sum_{0}^{\infty} P_{n+1}(0) \frac{a^{n+1}}{r^{n+1}} \qquad (5 - 9)$$

$$\text{for } r \leq a,\ \theta = 0,\ V_m = \frac{\mu_0 I}{2}\left(1 - \frac{r}{a} + \frac{r^3}{2a^3} - \frac{3r^5}{8a^5} + \ldots\ldots\right)$$

$$= \frac{\mu_0 I}{2}\left(1 - \sum_{0}^{\infty} P_n(0) \frac{r^{n+1}}{a^{n+1}}\right) \qquad (5 - 10)$$

Note that equation (5 - 9) satisfies the boundary condition $V_m \rightarrow 0$ when $r \rightarrow \infty$, $\theta = 0$.

Next we equate equation (5 - 9) to equation (5 - 7) when $\theta = 0$, $r \geq a$. Since $V_m \rightarrow 0$ when $r \rightarrow \infty$, the A_n in (5 - 7) must be zero for the boundary condition to hold. Thus for $r \geq a$,

$$V_m = \frac{-\mu_0 I}{2} \sum_{n=0}^{\infty} P_{n+1}(0) \frac{a^{n+1}}{r^{n+1}} P_n(\cos\theta), \; r \geq a \qquad (5 - 11)$$

The boundary condition for $r \leq a$ is that $V_m \rightarrow \frac{\mu_0 I}{2}$ as $r \rightarrow 0$, and this is met by equation (5 - 10). When we equate (5 - 10) with (5 - 7), we see that the B_n in (5 - 7) must be zero.

$$V_m = \frac{\mu_0 I}{2}\left[1 - \sum_{n=0}^{\infty} \frac{r^{n+1}}{a^{n+1}} P_n(0)\, P_{n+1}(\cos\theta)\right], \; r \leq a$$

Expanding 1 in a series of $P_n(\cos\theta)$ gives $1 = \sum_{n=0}^{\infty} k_n P_n(\cos\theta)$

$$V_m = \frac{\mu_0 I}{2}\left[k_0 P_0(\cos\theta) + \sum_{n=0}^{\infty}\left(k_{n+1} - \frac{r^{n+1}}{a^{n+1}} P_n(0)\right) P_{n+1}(\cos\theta)\right], \; r \leq a \qquad (5 - 12)$$

In (5 - 11) and (5 - 12) we have two expressions for V_m; at their interface at $r = a$ they must be equal so

$$\frac{-\mu_0}{2}\sum_{n=0}^{\infty} P_{n+1}(0)\, P_n(\cos\theta)$$

$$= \frac{-\mu_0}{2}\left[k_0 P_0(\cos\theta)+\sum_{n=0}^{\infty}((P_n(0)-k_{n+1})P_{n+1}(\cos\theta))\right],\quad r = a,$$

and $\sum_{n=0}^{\infty} P_{n+1}(0)\, P_n(\cos\theta) = -\, k_0 P_0(\cos\theta) + \sum_{n=0}^{\infty} (P_n(0) - k_{n+1})P_{n+1}(\cos\theta)$. (5 - 13)

Rewriting the left hand side of equation (5 - 13),

$$\sum_{n=0}^{\infty} P_{n+1}(0)\, P_n(\cos\theta) = P_1(0)\, P_0(\cos\theta) + \sum_{n=1}^{\infty} P_{n+1}(0)\, P_n(\cos\theta)$$

$$= P_1(0)\, P_0(\cos\theta) + \sum_{n=0}^{\infty} P_{n+2}(0)\, P_{n+1}(\cos\theta)$$

Thus equation (5 - 13) becomes

$$P_1(0)\, P_0(\cos\theta)+ \sum_{n=0}^{\infty} P_{n+2}(0)\, P_{n+1}(\cos\theta)$$

$$=-k_0 P_0(\cos\theta)+ \sum_{n=0}^{\infty} (P_n(0) - k_{n+1})\, P_{n+1}(\cos\theta).$$

Since the $P_n(\cos\theta)$ are orthogonal, we can equate terms in them, so

$-k_0 = P_1(0)$, $P_n(0) - k_{n+1} = P_{n+2}(0)$ thus $k_{n+1} = P_n(0) - P_{n+2}(0)$, $k \geq 0$

We can now rewrite (5 - 12) without the k_n

$$V_m = \frac{\mu_0 I}{2}\left\{-P_1(0)\,P_0(\cos\theta) + \sum_{n=0}^{\infty}\left[P_n(0)\left(1 - \frac{r^{n+1}}{a^{n+1}} - P_{n+2}(0)\right)P_{n+1}(\cos\theta)\right]\right\}$$

$$= \frac{\mu_0}{2}\sum_{n=0}^{\infty} P_n(0)\left\{\frac{(2n+3)}{(n+2)} - \frac{r^{n+1}}{a^{n+1}}\right\} P_{n+1}(\cos\theta) \qquad (5 - 14)$$

From (5 - 11) and (5 - 14) we can calculate B_r and B_θ for the regions $r \leq a$ and $r \geq a$, using

$$B_r = -\frac{\partial V_m}{\partial r}, \quad B_\theta = -\frac{1}{r}\,\frac{\partial V_m}{\partial r} \qquad (5 - 15)$$

thus

$$\left.\begin{aligned}
B_r &= \frac{\mu_0 I}{2}\sum_{n=0}^{\infty}(n+1)\frac{r^n}{a^{n+1}}P_n(0)\,P_{n+1}(\cos\theta), r \leq a \\
B_\theta &= \frac{\mu_0 I}{2r}\sum_{n=0}^{\infty}\left[P_n(0)\left(1-\frac{r^{n+1}}{a^{n+1}}\right)-P_{n+2}(0)\right]P^1_{n+1}(\cos\theta), r \leq a \\
B_r &= \frac{-\mu_0 I}{2}\sum_{n=0}^{\infty}P_{n+1}(0)\,(n+1)\frac{a^{n+1}}{r^{n+2}}P_n(\cos\theta), r \geq a \\
B_\theta &= \frac{-\mu_0}{2}\sum_{n=0}^{\infty}P_{n+1}(0)\frac{a^{n+1}}{r^{n+2}}P^1_n(\cos\theta), r \geq a
\end{aligned}\right| \qquad (5 - 16)$$

This equation, (5 - 16), describes the field; however, it should be pointed out that since there is a discontinuity at $\theta = \pi/2$, $r = a$ at the wire, it is not possible to fit the boundary conditions here, so equation (5 - 16) cannot be used in the region of $\theta = \pi/2$, $r \cong a$.

For comparison of the two methods of field calculation, the field from a circular coil calculated numerically by the COIL program described in Chapter 6 using the theory of section 4.3 is shown in Figure 5.2.2. Figure 5.2.3 identifies the rectangle over which the field was calculated. Figure 5.2.4 shows the components B_r and B_θ calculated from (5-16), with Figure 5.2.5 showing the first five terms in $P_n(\cos\theta)$ and $P^1_{n+1}(\cos\theta)$ from equation (5-16) individually.

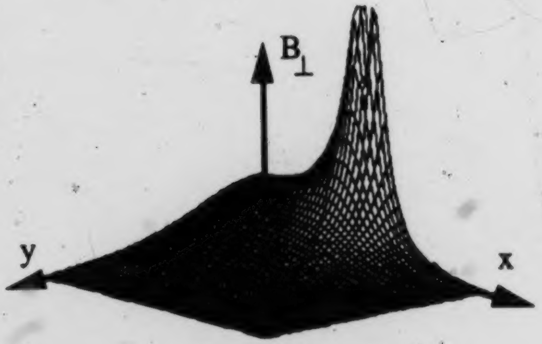

Figure 5.2.2 The total transverse field $B_\perp = (B_x^2+B_y^2)^{1/2}$ from a circular surface coil, calculated by numerical integration

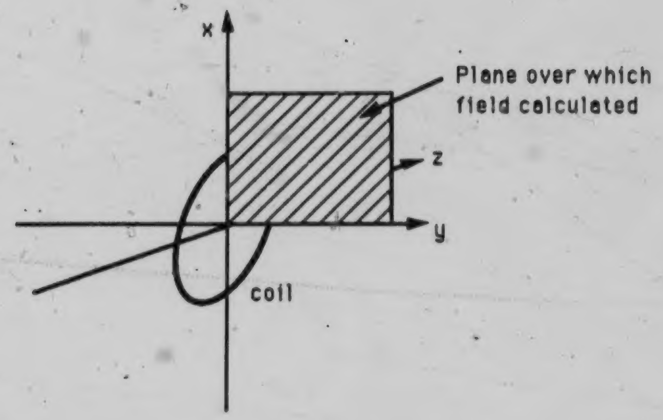
x
Plane over which field calculated
z
y
coil

Figure 5.2.3 The plane over which the field from the circular coil was calculated.

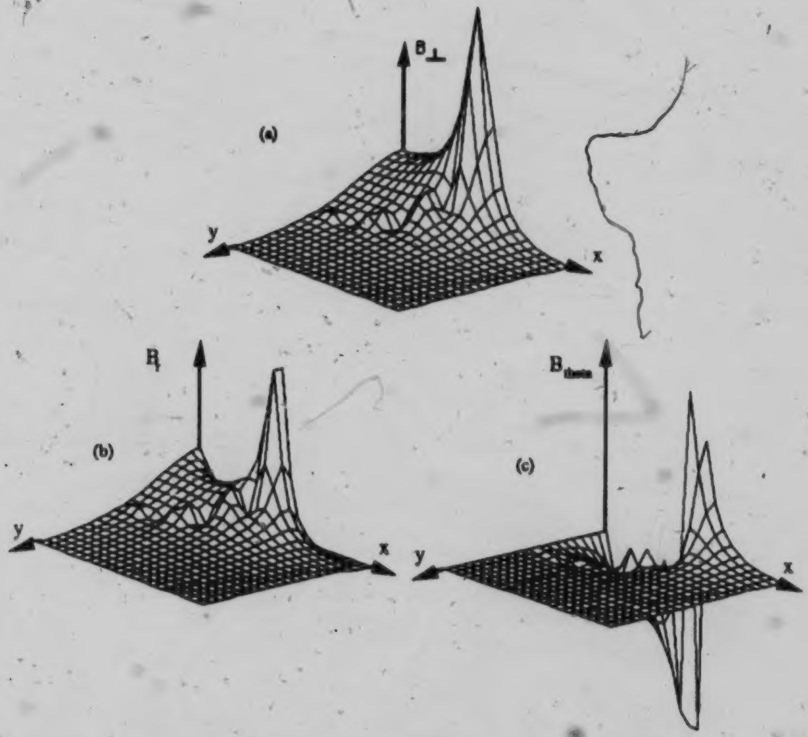

Figure 5.2.4 The field from a surface coil calculated from the spherical harmonic expansion, (a) total transverse field, (b) the B_r component and (c) the $B\theta$ component.

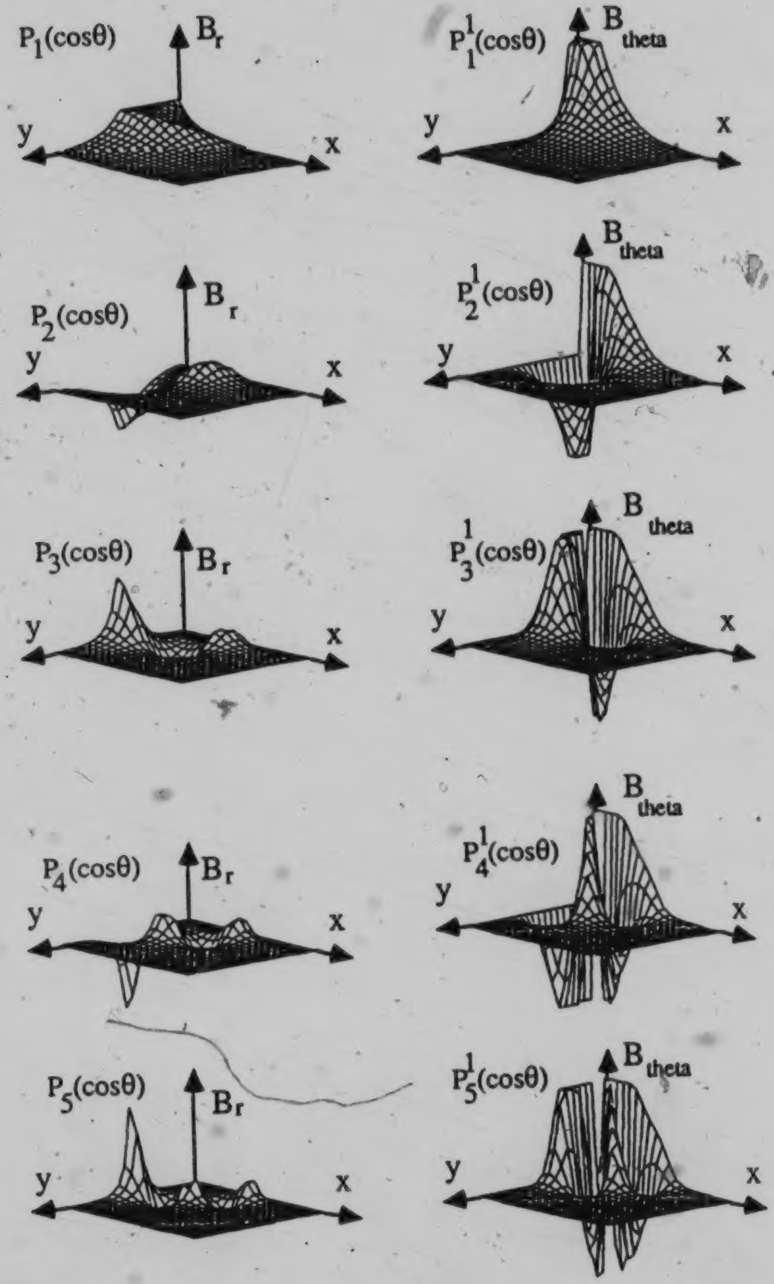

Figure 5.2.5 The contributions of the terms n = 1 to 5 of $P_n(\cos\theta)$ and $P_n^1(\cos\theta)$ respectively in equation (5 - 16).

5.3 Circular coil displaced from the origin along the axis of symmetry

When designing systems of coils it is not always possible to work with the origin at the centre of the coil. In this section the theory of Section 5.2 is extended for the case where the origin is not at the centre of the coil, but remains on the coil axis. The situation where the coil is shifted along the y axis is more complex and equations (5 - 16) are modified

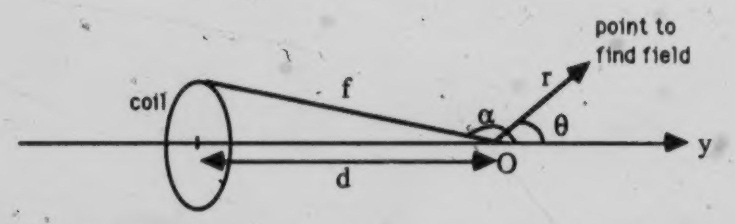

Figure 5.3.1 Coordinates for the case of a circular coil shifted away from the origin.

In this case along the y axis V_m is given by

$$V_m = \frac{\mu_0 I}{2}\left[1-\frac{(y-d)}{\sqrt{a^2+(y-d)^2}}\right],\ \theta = 0 \qquad (5 - 17)$$

Letting t = y/f, $V_m = \frac{\mu_0 I}{2}\left[1-\frac{(y-d)}{\sqrt{f^2-2dy+y^2}}\right]$

$$= \frac{\mu_0 I}{2}\left[1-\frac{(t-\cos\alpha)}{\sqrt{1-2\cos\alpha t+t^2}}\right],\ \theta = 0 \qquad (5 - 18)$$

This now has the form of the generating function for Legendre polynomials, which is:

$$\frac{1}{\sqrt{(1-2xt+t^2)}} = \sum_{n=0}^{\infty} P_n(x)\, t^n \qquad (5 - 19)$$

Using (5 - 19), we can write (5 - 18) in terms of the Legendre polynomials.

$$V_m = \frac{\mu_0 I}{2}\left[1-(t-\cos\alpha)\sum_{n=0}^{\infty} P_n(\cos\alpha)t^n\right],\ \theta = 0 \qquad (5 - 20)$$

This equation is rearranged to give an equation for V_m in powers of t,

$$V_m = \frac{\mu_0 I}{2}\left[(1+\cos\alpha) + \sum_{n=0}^{\infty} t^n(P_n(\cos\alpha)\cos\alpha - P_{n-1}(\cos\alpha))\right],\ \theta = 0 \qquad (5 - 21)$$

In this case, where we have set $t = y/f$, the series (5 - 21) will converge only if $t < 1$, or when $y < f$, since we wish to express V_m in terms of spherical harmonics.

Since V_m must be finite when $y \to 0$ $(r \to 0)$, and thus $t \to 0$, equation (5 - 21) contains only positive powers of y(r), so

$$V_m = \sum_{n=0}^{\infty} A_n r^n P_n(\cos\theta) \text{ or } V_m = \sum_{n=0}^{\infty} A_n y^n,\ \theta = 0$$

and from equation (5 - 21) we see that

$$A_0 = \frac{\mu_0 I}{2}(1+\cos\alpha),\ A_n = \frac{\mu_0 I}{2}(P_n(\cos\alpha)\cos\alpha - P_{n-1}(\cos\alpha))\, f^{-n},\ n \geq 1.$$

For the case of $r \geq f$, we use the substitution $t' = f/y$ in which case equation (5 - 17) can be written

$$V_m = \frac{\mu_0 I}{2}\left[1 - \frac{(1-t'\cos\alpha)}{\sqrt{t'^2+1-2t'\cos\alpha}}\right]. \qquad (5 - 22)$$

This also has the form of a generating function for Legendre polynomials (5 - 19), so equation (5 - 22) can be written

$$V_m = \frac{\mu_0 I}{2}\left[1-(1-t'\cos\alpha)\sum_{n=0}^{\infty} P_n(\cos\alpha)\, t'^n\right],\ \theta = 0$$

$$= \frac{\mu_0 I}{2}\sum_{n=0}^{\infty}[\cos\alpha\, P_{n-1}(\cos\alpha) - P_n(\cos\alpha)]\, t'^n,\ \theta = 0 \qquad (5 - 23)$$

Since the boundary conditions on V_m require that $V_m \rightarrow 0$ when $r \rightarrow 0$, and thus $t' \rightarrow \infty$, we use only the terms with negative powers of r in (5 - 7), and thus

$$V_m = \sum_{n=0}^{\infty} B_n r^{-(n+1)} P_n(\cos\theta) = \sum_{n=0}^{\infty} B_n y^{-(n+1)},\ \theta = 0$$

Equating terms with (5 - 23) gives

$$B_n = \frac{\mu_0 I}{2}[\cos\alpha\, P_n(\cos\alpha) - P_{n+1}(\cos\alpha)]\, f^{n+1},\ n \geq 0.$$

When $r = f$ the boundary condition requires that $V_{m,r\geq f} = V_{m,r\leq f}$, so terms in $P_n(\cos\theta)$ in the expansions of $V_{m,r\geq f}$ and $V_{m,r\leq f}$ must match individually, and thus $A_n = B_n$, giving

$$\frac{\mu_0 I}{2} k_n + \frac{\mu_0 I}{2} [P_n(\cos\alpha) \cos\alpha - P_{n-1}(\cos\alpha)] = \frac{\mu_0 I}{2} [P_n(\cos\alpha) \cos\alpha - P_{n+1}(\cos\alpha)]$$

where k_n is a constant term introduced to make A_n and B_n match.For this,

$$k_n = P_{n-1} (\cos \alpha) - P_{n+1}(\cos \alpha), \; n \geq 1 \qquad (5 - 24)$$

and thus we see that the A_0 term contributes these constants k_n, since

$$1+\cos \alpha = \sum_{n=0}^{\infty} [P_n(\cos \alpha) - P_{n+2}(\cos \alpha)] \, P_n(\cos \theta)$$

Rearranging (5 - 24) gives $k_n = P_n(\cos \alpha) - P_{n+2} (\cos \alpha), \; n \geq 0$, and thus

$$V_{m,r\leq f} = \frac{\mu_0 I}{2} \sum_{n=0}^{\infty} \left[(P_n(\cos\alpha) - P_{n+2}(\cos\alpha)) + [\cos\alpha \, P_{n+1}(\cos\alpha) - P_n(\cos\alpha)] \frac{r^{n+1}}{f^{n+1}} \right] P_{n+1}(\cos \theta)$$

$$(5 - 25)$$

$$V_{m,r\geq f} = \frac{\mu_0 I}{2} \sum_{n=0}^{\infty} [\cos\alpha \, P_n(\cos\alpha) - P_{n+1}(\cos\alpha)] \frac{f^{n+1}}{r^{n+1}} P_n(\cos\theta)$$

Equations (5 - 25) are seen to reduce to equations (5 - 11) and (5 - 14) when $\alpha = 90^o$ and f = a. Equation (5 - 25) is differentiated according to equation (5 - 15) to give B_r and B_θ.

$$B_r = -\frac{\mu_0 I}{2}\sum_{n=0}^{\infty}[\cos\alpha P_{n+1}(\cos\alpha) - P_n(\cos\alpha)]\,(n+1)\frac{r^n}{f^{n+1}}P_{n+1}(\cos\theta),\ r \le f$$

$$B_\theta = \frac{\mu_0 I}{2r}\sum_{n=0}^{\infty}\left[(P_n(\cos\alpha) - P_{n+2}(\cos\alpha)) + [\cos\alpha P_{n+1}(\cos\alpha) - P_n(\cos\alpha)]\frac{r^{n+1}}{f^{n+1}}\right]$$

$$P^1_{n+1}(\cos\theta),\ r \le f$$

$$(5 - 26)$$

$$B_r = \frac{\mu_0 I}{2}\sum_{n=0}^{\infty}[\cos\alpha P_n(\cos\alpha) - P_{n+1}(\cos\alpha)]\frac{f^{n+1}(n+1)}{r^{n+2}}P_n(\cos\theta),\ r \ge f$$

$$B_\theta = \frac{\mu_0 I}{2r}\sum_{n=0}^{\infty}[\cos\alpha P_n(\cos\alpha) - P_{n+1}(\cos\alpha)]\frac{f^{n+1}}{r^{n+1}}P^1_n(\cos\theta),\ r \ge f$$

Equation (5 - 26) reduces to equations (5 - 16) when $\alpha = 90^o$ and $f = a$.

5.4 Coil coordinate transformation for series convergence.

Figure 5.2.4 demonstrates that the series in equation (5 - 16) converge slowly in the region $r \approx a$, indicated by bumps on the surfaces for B_r, $B\theta$ and $B_\perp$. In equation (5 - 26) this slow convergence occurs when $r \approx f$. However, by shifting the coil along the z axis, it is always possible to find a place where $r > f$ or $r < f$. The field can be calculated at this position, and the field transformed to give the field at the original position.

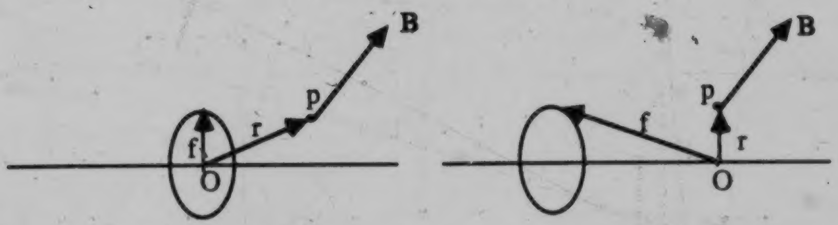

(a) original configuration
$r \equiv f$

(b) transformed configuration
$r << f$

Figure 5.4.1 Coil coordinate transformation to accelerate series convergence.

This simple coordinate transformation overcomes the problem of slow convergence of equati[illegible] 16) and (5 - 26). This transformation was performed for the case in which P was always shifted to a point where $\theta = \pm\pi/2$; the resulting calculated field is shown in Figure 5.4.2.

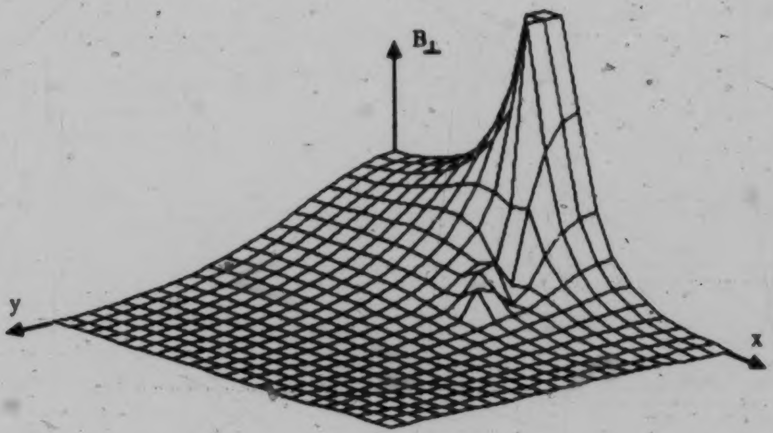

Figure 5.4.2 The transverse field $B_\perp$ calculated from spherical harmonics, but using the transformation of the point at which the field is calculated back to the xz plane.

5.5 Multi-loop coil field determination.

Equation (5 - 26) describes how the field from a circular coil can be calculated, given that the coil axis lies along the axis of symmetry of the cylindrical coordinate system. A coordinate transform has been shown to accelerate the spherical harmonic series convergence in Section 5.4. In this section the field from a coil consisting of multiple coils is calculated.

Consider a system of W co-axial loops, with each loop having the parameters f_g, α_g corresponding to f and α in Figure 5.3.1 and I_g being the current in the g^{th} loop. Equation (5-26) now becomes

$$B_r = \frac{\mu_0}{2} \sum_{g=0}^{W} I_g \sum_{n=0}^{\infty} \left\{ \begin{array}{l} r \le f \ldots [P_n(\cos\alpha_g) - \cos\alpha_g P_{n+1}(\cos\alpha_g)](n+1)\dfrac{r^n}{f_g^{n+1}} \\ r \ge f \ldots [\cos\alpha_g P_n(\cos\alpha_g) - P_{n+1}(\cos\alpha_g)](n+1)\dfrac{f_g^{n+1}}{r^{n+2}} \end{array} \right\} P_n(\cos\theta)$$

$$B_\theta = \frac{\mu_0}{2r} \sum_{g=0}^{W} I_g \left\{ \begin{array}{l} r \le f \ldots \sum_{n=0}^{\infty} [(P_n(\cos\alpha_g) - P_{n+2}(\cos\alpha_g)) \\ \qquad + \{\cos\alpha_g P_{n+1}(\cos\alpha_g) - P_n(\cos\alpha_g)\}](n+1)\dfrac{r^{n+1}}{f_g^{n+1}} P^1{}_{n+1}(\cos\theta) \\ r \ge f \ldots \displaystyle\sum_{n=0}^{\infty} [\cos\alpha_g P_n(\cos\alpha_g) - P_{n+1}(\cos\alpha_g)]\frac{f_g^{n+1}}{r^{n+1}} P^1{}_n(\cos\theta) \end{array} \right\} \qquad (5 - 27)$$

This analytic solution for the magnetic field from a multi-loop coil is straightforward to implement in a computer program; the TurboPascal program listed in Appendix H calculates the field from a multi-loop coil using equation (5-27) and the coordinate transformation of Section 5.4. The field calculation for a single offset loop is shown in Figure 5.5.1.

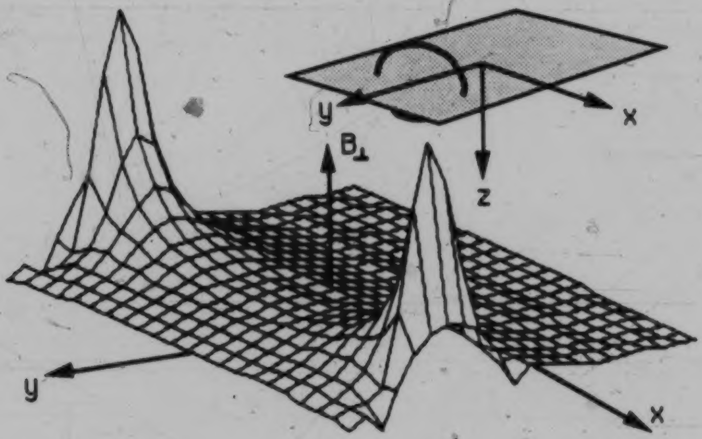

Figure 5.5.1 The transverse field (xy plane) from a circular coil axial with the y axis but displaced from the origin.

The field from the breast coil described in Chapter 6 was calculated using the theory presented in this section. Since the theory was for circular coils whose plane was perpendicular to the axis of symmetry of the cylindrical coordinate system, a true three-turn conical helix could not be calculated, so the helix of Figure 6.3.4 was replaced by a three-loop coil system, as shown in Figure 5.5.2. The coil parameters are given in Appendix H.

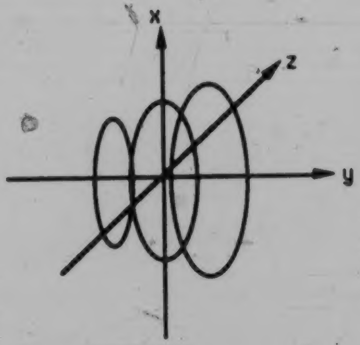

Figure 5.5.2 A three-loop coil approximating a conical helix.

The field calculated is shown in Figure 5.5.3.

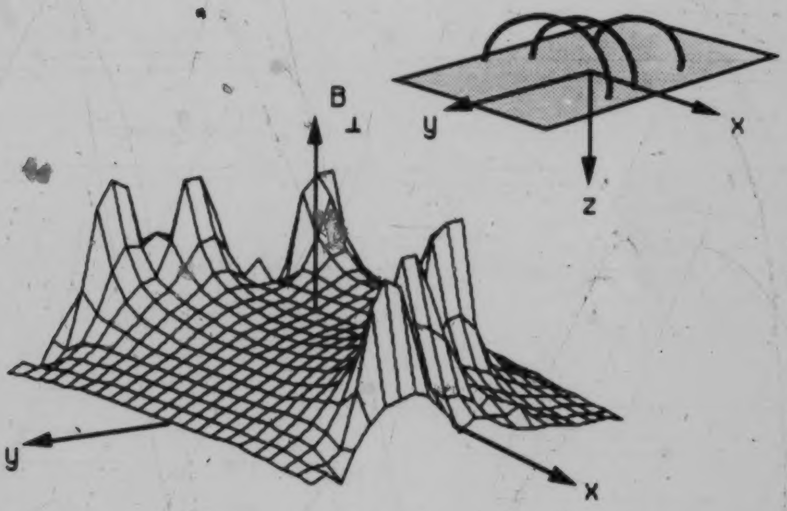

Figure 5.5.3 Transverse field in the xy plane from the three-loop coil approximating the conical helix co-axial with the y axis.

The plateau region near the origin on Figure 5.5.3 corresponds to the uniform region seen on the field maps calculated by numerical integration (Figure 8.4.2(d)).

The method of field calculation described in this chapter is suitable for magnetic field optimization by computer control of the coil parameters f_g, α_g and I_g, since the solution is analytic. Without the restrictions of currents flowing on the surface of a cylinder used by Turner [1986], the spherical harmonic method could be used to design gradient coil sets and surface coils with geometries other than cylindrical, for which Turner's approach of Fourier-Bessel-series expansion is probably the most suitable.

The only available standard against which to test the accuracy of both the numerical integration and spherical harmonic field calculations is the field along the axis of the coil, derived analytically by differentiating equation (5 - 8) according to equation (5 - 15). The program listed in Appendix H is capable of calculating the field along the coil axis to within 1% of the analytic calculation. The accuracy is determined by the number of terms taken in the series expansion of the field components. In the program listing the number of terms is set at 16. However, this is limited only by the time available for the calculation. The field plot in Figure 5.5.3 took about 1 hour to calculate on a Macintosh II microcomputer.

Figure 5.4.2 demonstrates that the coordinate transformation is not ideal in the region $x \approx a$. Other, more sophisticated, coordinate transformations could reduce the inaccuracy in this region.

In order to design coil geometries for arbitrary field distributions, it will be necessary to either invert the field equations of this chapter, or use computer techniques to optimize the field distribution based on putting certain constraints on the coil parameters. This will require further work.

CHAPTER 6

THE DESIGN OF THE BREAST COIL

In order to evaluate coil designs with complex geometries it is necessary to be able to calculate the magnetic field produced by the coil. The purpose of this chapter is to describe how this can be done numerically, and to introduce my program named COIL which has been developed in Turbo Pascal for the Macintosh microcomputer for this purpose. This program is described in detail in Appendix A.

6.1 Field calculation and the COIL program.

The field from a coil is calculated using the Biot-Savart Law described in Section 4.2, by breaking up the coil into a large number of short straight segments as described in Section 4.3. The COIL program has as its input a text file containing a description of the coil in terms of arcs and lines. The program output is three data files containing the three components (B_x, B_y and B_z) of the magnetic field. The region over which the field is to be calculated is defined using five parameters. The first of these is the base point (x_0,y_0,z_0) in Cartesian coordinates relative to which the region is located . The shape of the region is defined by two direction vectors also in Cartesian coordinates $(\Delta x_1,\Delta y_1,\Delta z_1)$ and $(\Delta x_2,\Delta y_2,\Delta z_2)$. The maximum number of times that the direction vectors are added in each direction to give the point at which the field is calculated comprise the other two parameters N_1 and N_2. The two direction vectors would normally be perpendicular, but do not need to be for the program. The points at which the field is calculated are given by equation (6 -1). The way that the field data is arranged in data files, and other details of the program are given in Appendix A.

$$\left.\begin{aligned} x &= x_0 + i\Delta x_1 + j\Delta x_2 \\ y &= y_0 + i\Delta y_1 + j\Delta y_2 \\ z &= z_0 + i\Delta z_1 + j\Delta z_2 \end{aligned}\right| \quad \begin{aligned} 0 \le i \le N_1 \\ 0 \le j \le N_2 \end{aligned} \qquad (6 - 1)$$

6.2 Example of coil field calculation using the program COIL.

As an example of the use of the software, the field from a circular coil lying on the xz plane is calculated. The first step is to define the geometry of the coil (see Appendix A for further details). This is done by dividing the circle into 4 arcs, as shown in Figure 6.2.1.

```
*     circle in the xz plane
*       coil definition
*      four arcs are used
*
*    start     finish     centre
*    x y z     x y z     x y z
arc  1 0 0     0 0 1     0 0 0
arc  0 0 1  -1 0 0      0 0 0
arc-1 0 0     0 0 -1    0 0 0
arc  0 0 -1   1 0 0      0 0 0
end
*
* parameters
xmax=4
ymax=4
zmax=4
seglength=.1
end
```

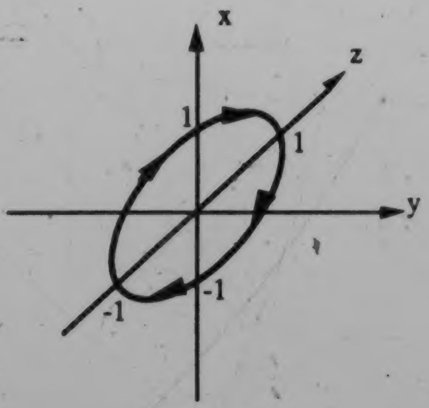

Figure 6.2.1 The definition of the circular coil file.

The B_y component of the field can now be calculated at discrete points along the axis of the coil using the numerical integration program COIL, giving the results shown in Figure 6.2.2. The current flowing is 1 A and the deviation from the theory of Section 4.2 is less than 1%.

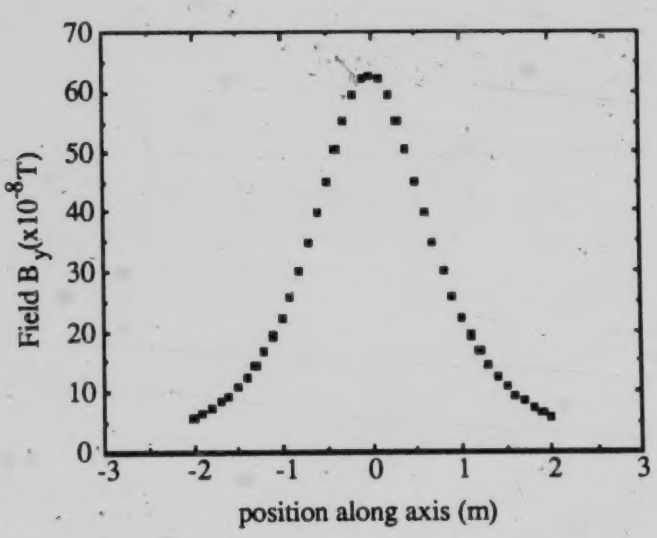

Figure 6.2.2 The calculated B_y component of the field along the axis of a 1 m radius circular coil at discrete points, when a current of 1 A flows in the coil.

The field can also be calculated at points within a rectangle, and in Figure 6.2.3 the rectangle is chosen to be in the xy plane perpendicular to the coil.

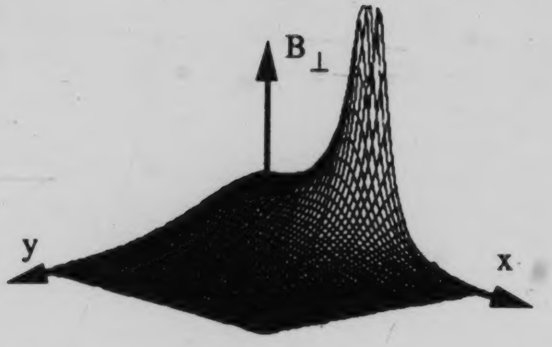

Figure 6.2.3 The transverse field $B_\perp$ in the xy plane for the circular coil.

Calculated data can then be used to make tip angle contour plots. These were done for the coil defined above. The main field, B_0, was assumed to be in the z direction, so that in the zy plane, where the B_x component of the magnetic field is

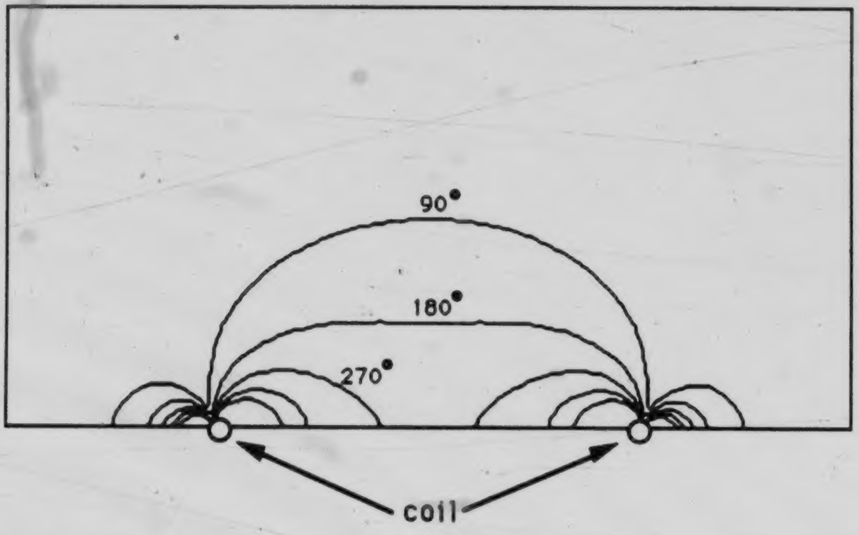

Figure 6.2.4 Contour plot of tip-angle for circular coil for section parallel to B_0 field.

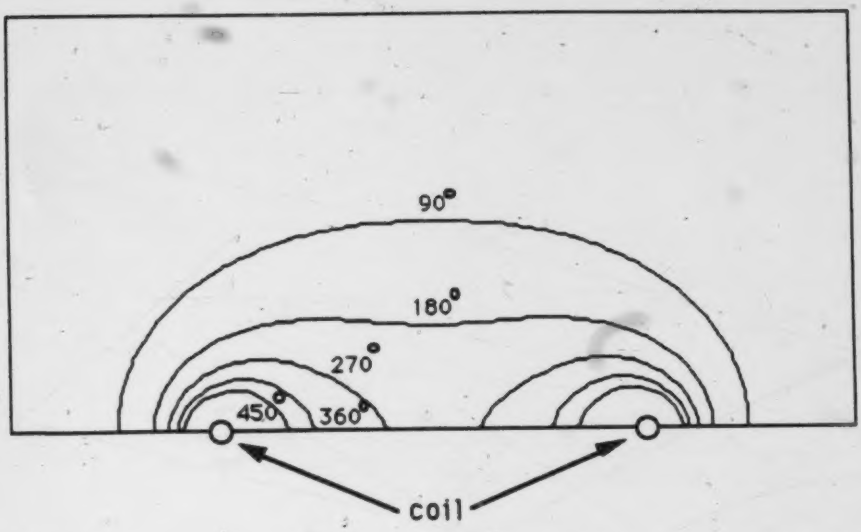

Figure 6.2.5 Contour plot of tip angle for circular coil for section perpendicular to the B_0 field.

zero, the field which tips the nucleii is only the B_y component. In the xy plane, however, the B_x and B_y components of the magnetic field both contribute to the tipping of the nuclei. The tip angle contour plots are thus different for the zy and xy planes corresponding to the planes parallel and perpendicular to the B_o field, respectively.

From Figures 6.2.4 and 6.2.5, the contour plots of the tip angle are seen to be smoothly continuous for the xy plane, while they have a node at the wire in the zy plane.

The accuracy of the field calculated by the COIL program is limited by the length of the straight segments into which the coil is divided. For the calculation of the field in Figure 6.2.2 the circular coil was divided into about 30 straight segments by setting the segment length to 10 cm for the 1 m radius coil.

The field calculation for Figure 6.2.3 took approximately 2 hours on the Macintosh II microcomputer to calculate the field at 1600 points. The coil radius was 1 m and the segment length 10 cm.

6.3 Using COIL to design the breast coil.

The design requirements for the breast coil were that it should be tunable for both proton and phosphorus NMR frequencies, and should be suitable for both imaging and spectroscopy. In order to maximize the signal-to-noise ratio when doing spectroscopy and imaging, the coil should be as close to the breast as possible (Section 4.1.2). This suggested a conical coil, since it had already been decided that the patient should lie prone in order that the maximum view of the breasts be obtained. Previous workers have used single turn surface coils [Dash *et al*, 1986; Heywang *et al*; 1986, Wiener *et al*, 1986], tube resonators [Wolfmann *et al*, 1986] and tapered saddle coils [McOwan and Redpath, 1987] principally for imaging the breasts. Most breast spectroscopy experiments have been performed using circular single-turn surface coils.

Designs which were considered for the breast coil were (a) conical helix, (b) parallel rings and (c) helix as shown in Figure 6.3.1 since these could be simply described mathematically. In order to make the field as uniform as possible over the volume of the breast the helix was preferred, and the conical helix was best fitted to the shape of the breast to maximize signal-to-noise ratio.

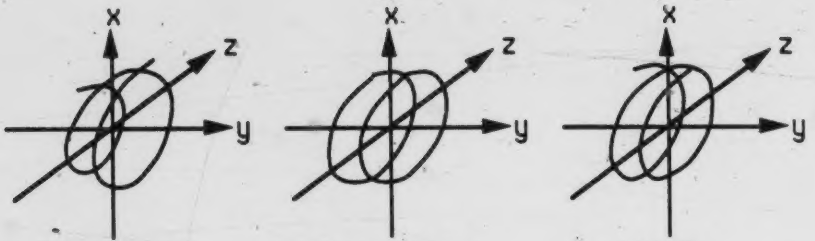

(a) conical helix (b) parallel rings (c) helix

Figure 6.3.1 Some coil geometries considered for the breast coil.

However, when using a conical helix the problem arose that the field was intensified at the narrow end of the coil, as shown in Figure 6.3.2, where the on-axis field for the three types of coil in Figure 6.3.1 are compared. Each has a largest diameter of 14 cm and a current of 1 A flowing in it.

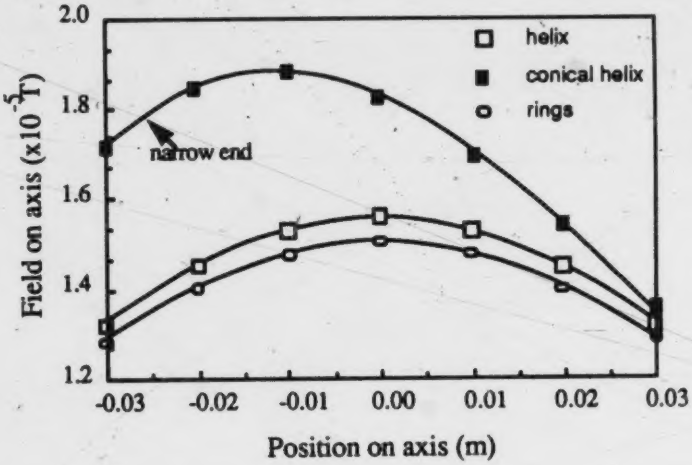

Figure 6.3.2 Comparison of field from different breast coil geometries along coil axis.

The field from the helix was made more uniform along the axis by compressing the turns near the ends, and expanding them at the centre, as shown in Figure 6.3.3. Observing from Figure 6.3.2 that the field intensity appeared to drop as the square of the distance from the centre of the coil, the turns ratio was increased as the square of the distance from the centre. Since the number of turns was so small, a quarter turn was used in place of a complete turn as the unit of winding.The effect of the increased field near the small end of the conical helix was reduced by increasing the turns density near the large end, and decreasing it near the small end. Since for a short solenoid the field at the centre is proportional to the number of turns per unit length divided by the radius [Harpen, 1987], to keep the field constant the ratio of turns density to radius of the turn was kept constant along the coil. These two techniques applied together improved the field distribution of the conical helix as required in Section 4.1.2.

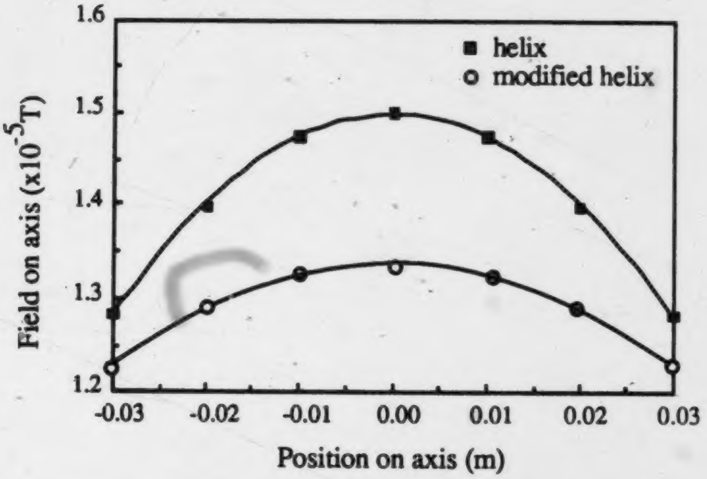

Figure 6.3.3 Improved field uniformity by non-linear turns spacing.

Since the techniques mentioned above required a large number of turns to work optimally, and since the inductance of the coil limited the number of turns which could be used practically, the number of turns was chosen as three, which enabled some correction by adjusting the turns density but was still tunable.

The design used in the study was a three turn conical helix with non-linear turns spacing (Figure 6.3.4). The wide end of the coil was 14 cm in diameter, and the small end was 8 cm. The exact geometry is described in a COIL program data file at the end of this section. This size was able to accommodate all the volunteers in the study. It would however be too small for obese women and those with large tumours. For practical reasons of the size of the tune and match capacitors, both right and left handed helices were used.

Once the on-axis field had been made as uniform as possible, the COIL numerical integration program was used to calculate the field over the field of view of the coil. This was to test the uniformity of the field, and was later used for correcting the images taken with the coil (see Section 8.4).

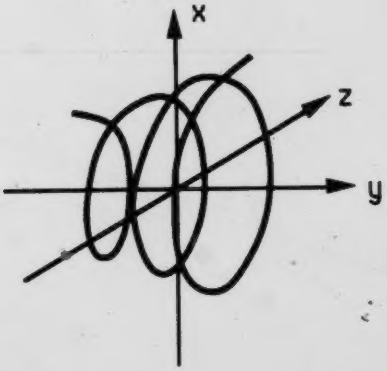

Figure 6.3.4 The three-turn modified conical helix used as the breast coil

The conical helix breast coils were mounted in a patient bed constructed of wood and acrylic as shown in Figure 6.3.5. Rods extending from the foot of the bed enabled the coils to be tuned and matched with the patient lying on the bed. The electrical circuit for tuning and matching is shown in Figure 6.3.6.

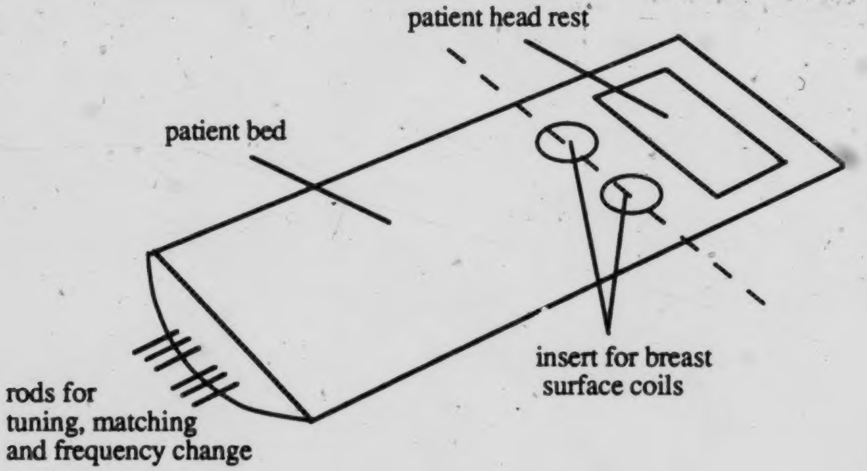
patient head rest
patient bed
insert for breast surface coils
rods for tuning, matching and frequency change

Figure 6.3.5 Patient bed used to mount breast coils.

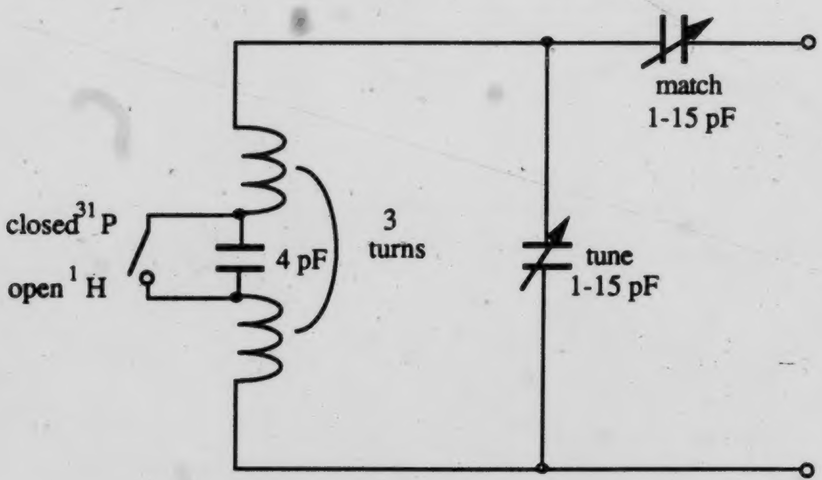
match
1-15 pF
closed ^{31}P
open ^{1}H
4 pF
3 turns
tune
1-15 pF

Figure 6.3.6 The breast coil electrical circuit.

The exact description of the conical helix of Figure 6.3.4 is given below in the format required by the COIL program.

```
* 3 turn modified conical helix
* left hand screw in y
* made of 24, 45 degree arcs
*
*          start                    finish                   centre
*    x      y      z       x      y      z       x      y      z
*
arc  7      4      0       4.9    3.75   -4.9    0      3.87   0
arc  4.9    3.75   -4.9    0      3.5    -6.8    0      3.63   0
arc  0      3.5    -6.5    -4.55  3.25   -4.55   0      3.37   0
arc  -4.55  3.25   -4.55   -6.5   3.0    0       0      3.12   0
arc  -6.2   3.0    0       4.34   2.7    4.34    0      2.85   0
arc  -4.34  2.7    4.34    0      2.4    6.2     0      2.55   0
arc  0      2.4    6       4.2    2.1    4.2     0      2.25   0
arc  4.2    2.1    4.2     6      1.8    0       0      1.95   0
arc  5.8    1.8    0       4.06   1.5    -4.06   0      1.65   0
arc  4.06   1.5    -4.06   0      1.2    -5.8    0      1.35   0
arc  0      1.2    -5.5    -3.85  0.9    -3.85   0      1.05   0
arc  -3.85  0.9    -3.85   -5.50  0.6    0       0      0.75   0
arc  -5.2   0.6    0       -3.64  0.25   3.64    0      0.43   0
arc  -3.64  0.25   3.64    0      -0.1   5.2     0      0.07   0
arc  0      -0.1   5       3.5    -0.45  3.5     0      -0.27  0
arc  3.5    -0.45  3.5     5      -0.8   0       0      -0.62  0
arc  4.7    -0.8   0       3.29   -1.15  -3.29   0      -0.97  0
arc  3.29   -1.15  -3.29   0      -1.5   -4.7    0      -1.32  0
arc  0      -1.5   -4.5    -3.15  -1.85  -3.15   0      -1.67  0
arc  -3.15  -1.85  -3.15   -4.5   -2.2   0       0      -2.02  0
arc  -4.3   -2.2   0       -3     -2.65  3       0      -2.42  0
arc  -3     -2.65  3       0      -3.1   4.3     0      -2.87  0
arc  0      -3.1   4       2.8    -3.55  2.8     0      -3.32  0
arc  2.8    -3.55  2.8     4      -4     0       0      -3.77  0
end
*
topleftx=50
toplefty=50
bottomrightx=200
bottomrighty=200
titlex=20
titley=20
title=three turn modified conical helix
xmax=20
ymax=20
zmax=20
seglength=0.5
end
```

Examples of the use of this breast coil for imaging and spectroscopy are given in Chapters 8 and 9.

6.4 Testing the breast coil

The three-turn conical helix breast coil described in the previous sections was tested against the existing body coil, and the results are given below.

6.4.1 Phantom imaging.

The purpose of this phantom study was to compare the images taken with the breast coil with those taken with the body coil supplied with the Philips Gyroscan system, when taking images of the same phantom. The phantom consisted of two concentric glass spheres of outer diameter 76 mm and inner diameter 43 mm filled with water.

The phantom was placed in the left breast coil of the patient bed and an image taken with a field of view of 100 x100 mm. The image slice thickness was 2 mm, and the image was a spin echo image with echo time 50 ms and repetition time 580 ms. This image is shown in Figure 6.4.1.1 (a). Secondly, the breast coils were removed from the patient bed, in case they coupled with the body coil, and an image was taken with the body coil. The same spectrometer settings were used as mentioned for the breast coil above. The body coil image is shown in Figure 6.4.1.1 (b). It is apparent that the breast coil has a greater signal-to-noise ratio than the body coil. This is quantified in the next section.

6.4.2 Comparison of the breast coil with the body coil.

The signal-to-noise ratio is estimated from the images [Philips, 1989] by

$$\text{SNR} = \frac{\text{mean of uniform region within sample}}{\text{SD of uniform region within sample}}\ .$$

The mean and standard deviation of pixel levels over regions within an image are readily measured on the Philips Gyroscan spectrometer using the standard ROI (region of interest) feature. A circular or square region, of chosen size, can be located over part of the image and the mean and standard deviation of the pixel intensities within that region measured. Using this technique the signal-to-noise ratios shown in Table 6.4.2.1 were calculated.

Ghosting is creation of false images in the image, usually most severely in the phase-encoding direction. The level of ghosting can be calculated by comparing the pixel level over a region near the phantom in the phase-encoding direction with the pixel level over a region far from the phantom, and in the readout gradient direction.

$$\text{Level of ghosting} = \frac{\text{Mean of ghost image region - mean of background}}{\text{Mean of phantom image region - mean of background}}$$

The calculated percentage ghosting levels are given in Table 6.4.2.1.

	Mean/SD of the 0.2 cm^3 region at centre of phantom.	Mean/SD of background.	SNR	Mean/SD of ghost.	Ghosting level.
breast coil image	1068/99	103/52	10.8	118/57	1.6%
body coil image	885/370	492/263	2.4	495/271	0.8%

Table 6.4.2.1 Comparison of the signal-to-noise ratios and ghosting levels of breast and body coils.

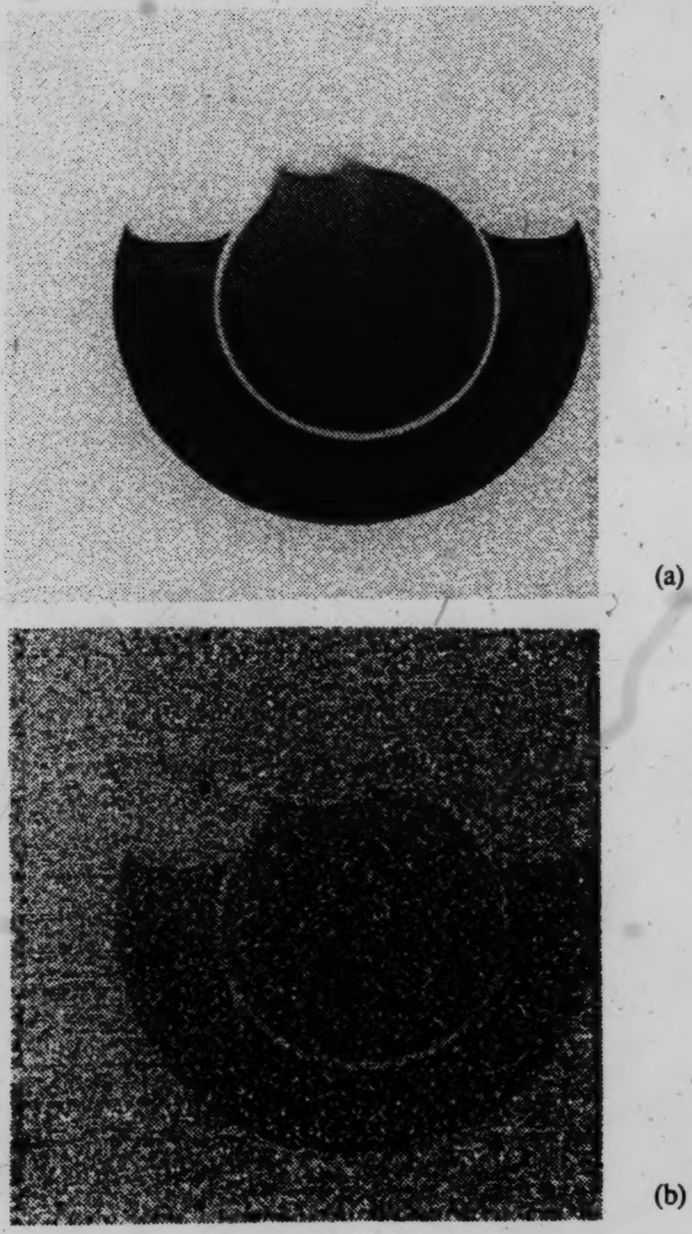

Figure 6.4.1.1 Images taken with (a) the breast coil and (b) the body coil. Field of view is 100 x 100 mm and slice thickness is 2 mm.

The breast coil is seen to have a significantly higher signal-to-noise ratio than the body coil, and while the ghosting level is lower for the body coil, that from the breast coil is still not apparent in the image of Figure 6.4.1.1 (a). The 1 mm glass wall of the phantom is clearly resolvable on the breast coil image, but not clearly resolvable on the body coil image because of the higher noise level.

CHAPTER 7

THE NORMAL VOLUNTEER BREAST TRIALS

In order to test the efficacy of the breast coil described in Chapter 6, NMR imaging and spectroscopy trials were carried out using the breast coils mounted in the patient bed (Figure 6.3.5). These trials were performed under the watchful eye of Dr.Scott Ernst, the attending doctor. The trials were approved by the Ethics Committee of the Cross Cancer Institute, and were under the control of Dr.McEwan, Head of the Department of Nuclear Medicine.

7.1 Selection of the volunteers.

Since as wide a range of breasts as possible was required for the trials, volunteers were recruited from nurses within the University of Alberta, Volunteer Staff of the Cross Cancer Institute and through friends. Requirements of the volunteers were that they have no internal metal, were able to lie still for up to one hour, and did not suffer from claustrophobia.

7.2 Examination Procedure

After briefing about the nature of the project, and what the volunteer would need to do and expect to experience during the examination, an informed consent and relevant menstrual history were obtained. The consent form used for the normal healthy volunteers is shown in Appendix G. The volunteer was shown to a changing room and asked to don the blouse which she would wear throughout the examination, and then was checked for the presence of any metal objects before being led to the patient table. The volunteer was instructed to lie prone on the patient bed and to position her breasts such that they were comfortably in the centre of the breast cups. The patient bed was centered in the magnet using the light beams provided in the magnet. The volunteer was instructed to close her eyes during the alignment process to avoid any danger to her eyes from the low-powered lasers used by the Gyroscan system for alignment of the patient bed. The patient bed was then moved into the magnet until the line through the centre of the breast cups was at the centre of the magnet.

The study of each volunteer was in three parts: proton imaging, proton spectroscopy and phosphorus spectroscopy. Once the patient was installed in the magnet, either the left or right breast was selected by connecting the appropriate coil to the socket in the magnet housing. The coil was then tuned to the proton resonance and matched to the preamplifier using the tune and match rods which extended under the patient bed and came out below the volunteer's feet.

Once the coil had been tuned to the proton resonance, a set of six transverse images were made, 5 mm apart and centered on the centre of the breast cup. The field of view of these images was 250 x 250 mm. These images took about 5 minutes to obtain, and were viewed at once to ensure that the patient was in a suitable position for the spectroscopy.

When the images had confirmed that the position of the breast under examination was correct, the magnet shims were adjusted to give the most uniform B_0 field across the breast under examination. Shimming was a time consuming process, and normally took from 5 to 10 minutes. The localized spectroscopy was then performed on a 3 x 3 x 3 cm cube located behind the volunteer's nipple. This took approximately 2 minutes for 32 scans.

After the proton spectroscopy the volunteer was given the opportunity to move about before the longest part of the examination, the phosphorus spectroscopy. The coil was retuned for phosphorus, and then the phosphorus spectrum localized to a 45 mm slice through the breast parallel to the chest wall was obtained. This spectrum took approximately 12 minutes to obtain.

At the end of the examination the patient was asked to comment on any uncomfortable or disconcerting parts of the examination procedure, and these comments were recorded and used to improve the procedure.

7.3 The imaging method.

Imaging was performed on the Philips Gyroscan spectrometer using Gyroscan version 5.6 software. The centre of the breast coils was measured as being at ± 98 mm away from the isocentre of the magnet in the left-right or y direction and at -22 mm from the isocentre in the anterior-posterior or x direction. The coordinate system for imaging is shown in Figure 7.3.1.

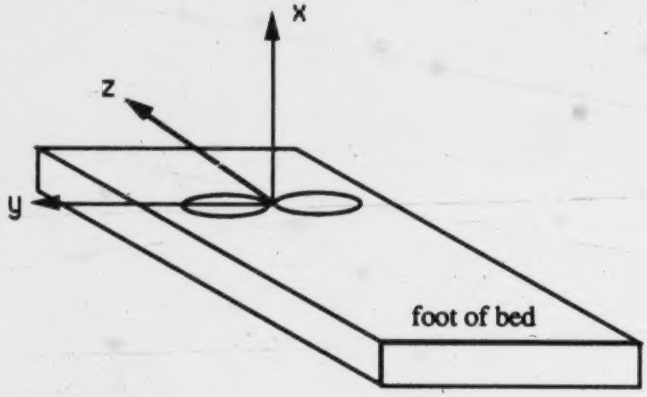

Figure 7.3.1 Imaging coordinate system.

The coordinates (-22 mm, 98 mm, 0 mm) were always used for the centre of the left breast images, and (-22 mm, -98 mm, 0 mm) for the coordinates of the centre of the right breast image. The field of view of the image was 250 x 250 mm. The imaging sequence used was multislice spin echo, with 90^{o} pulse length 0.11 ms. The echo time was 50 ms and the repetition time 580 ms. 6 contiguous 5 mm slices were taken. The *imaging pulse sequence is described in* Section 3.2.2.

7.4 The spectroscopy method.

The spectroscopy was performed using Gyroscan version 4.7 software and the LACTATE programme written by Mr. Dan Gheorghiu and designed by Dr. Chris Hanstock, both of the Clinical NMR Unit, University of Alberta. Before spectroscopy could be performed, shimming was carried out using LACTATE with the BREASTSHIM parameter file. The parameter file contains all the variables needed for LACTATE to produce the pulse sequence needed for spectroscopy. Two peaks appeared on the proton shimming spectrum, from water and from fat. The goal of shimming was to make these peaks as narrow as possible, indicating that the B_0 field was the most uniform over the breast volume. Only the first order shims in x, y and z were used, i.e. those shims which produce independent linear field gradients in the x, y and z directions. The width of the water resonance while shimming was about 0.3 ppm (20 Hz at 1.5 T). In cases where the breast was predominantly fat, the fat peak was used rather than the water peak for shimming. This was less satisfactory since the fat peak has several resonances, corresponding to protons at different positions on the long carbon chains found in fats [Sijens *et al*, 1988] which made the peak difficult to shim.

The coordinate system for spectroscopy on the Philips Gyroscan is different from that used for imaging. This required a coordinate transformation from imaging coordinates to spectroscopy coordinates. Fortunately this only required changing the sign of the y ordinate, as shown in Figure 7.4.1.

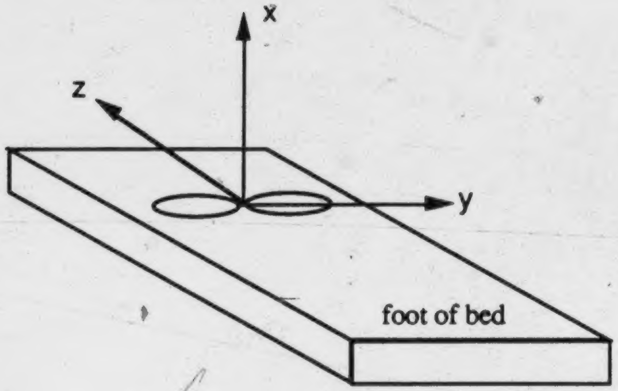

Figure 7.4.1 Spectroscopy coordinate system.

7.4.1 Proton spectroscopy

The proton spectroscopy was performed with LACTATE and the BREASTH parameter file. This contained the parameters for a three-dimensional ISIS (see Section 3.2.3.1) spin echo sequence. The location was centered on (±98 mm, -22 mm, 0 mm) and the cube had dimensions 30 x 30 x 30 mm. Thirty-two repetitions were performed to complete the ISIS sequence with phase cycling. This location was chosen since it normally contained both fat and gland tissue.

The 90^o pulse had a length of 0.1 ms, and the RF power attenuation was set to 20 dB. The echo time was 100 ms and the repetition time was 2 s.

7.4.2 Phosphorus spectroscopy

The phosphorus spectroscopy was performed with LACTATE and the BREASTP parameter file. This contained the parameters for a one-dimensional ISIS 90^{o}-acquire sequence. The location was centered at x = -22 mm and the slice had a thickness of 45 mm.This location was used since it isolated the breast from the chest wall and associated muscle. Two hundred and fifty-six repetitions were performed to complete the ISIS sequence with phase cycling.

The 90^{o} pulse had a length of 0.1 ms, and the RF power attenuation was set to 24 dB. The repetition time was set at 3 s.

CHAPTER 8

NMR IMAGING OF THE BREAST

The images in this study were taken using the 1.5 Tesla Philips Gyroscan system and the patient bed with two breast surface coils described in Chapter 6. Twenty-five normal volunteers were examined. They lay prone on the patient bed with their breasts pendant in the breast coils. Six spin echo images were taken of one or both breasts, each image being from a slice 5mm thick, and with the images contiguous. The images were transverse images, and located near the centre of the breast coil cups, with three cranial to the nipple and three caudal to the nipple, so that the region behind the nipple could be seen. In this chapter some images are presented and correlation made to patient parameters.

8.1 Images from normal volunteers.

The volunteers examined in this study ranged in age from 21 to 68 and included nursing mothers. The experimental method used is described in Chapter 7. The images in this section were chosen to demonstrate particular features, and are a fraction of the more than 200 images taken. Two distinct regions were seen on the images, one with low intensity (light in images in this thesis) and one with high intensity (dark in images in this thesis). This section attempts to relate the images with the breast anatomy described in Chapter 2.

Anatomically one would expect to find the main collecting ducts located directly behind the nipple, and on the images there was seen to be a low intensity region here. The areolar region contains little fat, and the images showed that the low intensity region includes the areolar region, nipple and ducts, which extend into the breast fat behind the nipple. The anatomical regions are described below.

Fat

Because fat containing structures are readily identified on the NMR images, it is apparent that there exists a wide variation in the relative fat concentrations from volunteer to volunteer. A number of fat types can be distinguished from the images (Figure 8.1.1):

1. Lobular - multiple discrete lobules of fat. These lobules are traversed by fine linear water-dense structures which may be blood vessels or supporting fibrous stroma. These fat lobules are part of the interlobular stroma of the breast. They are most apparent in premenopausal nulliparous women (Figure 8.1.1(a)).

2. Speckled - a speckled arrangement of fat throughout the breast. The fat appears to be closely associated with the breast parenchyma and other stromal structures. This fat is primarily found in perimenopausal and postmenopausal women (Figure 8.1.1(b)).

3. Subcutaneous - this pattern of fat distribution was present in all images and consisted of a band of fat-dense tissue around the periphery of the breast. This undoubtedly represents the layer of subcutaneous fat under the skin. This layer can be seen to taper and stop at the peri-areolar region where the collecting ducts converge, and where no subcutaneous fat exists anatomically (Figure 8.1.1(c)).

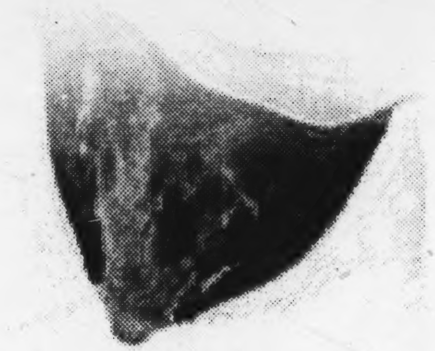

(a) lobular fat in the breast of a young nulliparous woman.

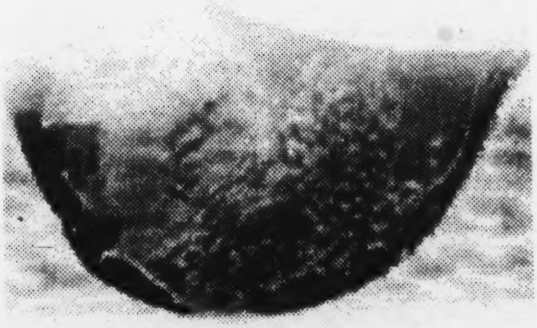

(b) speckled fat in the breast of a perimenopausal multiparous woman.

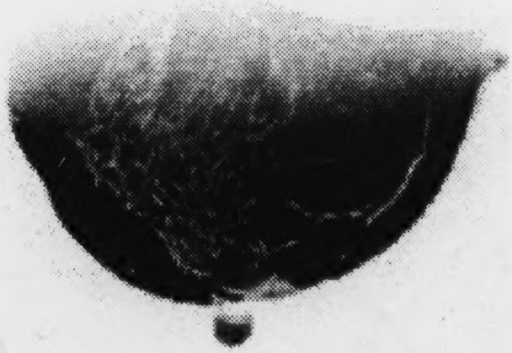

(c) subcutaneous fat surrounds the breast, disappearing near the areolar region. (Marker sphere at bottom centre).

Figure 8.1.1 Fat types seen in images of the breast.

Blood vessels

Blood vessels can be identified on the images as areas of reduced signal intensity haloed by regions of increased signal intensity. This pattern reflects a motion artefact caused by the flow of blood through the six contiguous slices. The central area of low intensity results from the relatively high flow velocity at the centre of the vessel. The high intensity region seen at the periphery of the vessels results from the flow-related enhancement; the additive contribution of slowly flowing blood entering the imaging volume. The blood has not been previously magnetized and therefore an enhanced signal is generated upon excitation (see Figure 8.1.2(a)).

Gland tissue

Gland tissue is seen as lower intensity areas interspersed with the fat in the breast. This is confirmed by the large areas of this type seen in the lactating breast (Figure 8.1.3(b)), in which much of the breast volume is taken up with gland tissue. Ducts are clearly seen as lines originating in the areolar region and spreading into the breast (Figure 8.1.2(b)). Lactating women have large amounts of glandular tissue when compared with non-lactating women, as shown in Figure 8.1.3.

Certain factors are clearly seen to affect the appearance of breast images. Some of these are:

Age

It is well established histologically that relative fat content increases with age. Following menopause, the breast is almost entirely replaced by adipose tissue. Figure 8.1.4 compares breasts of pre and post menopausal women.

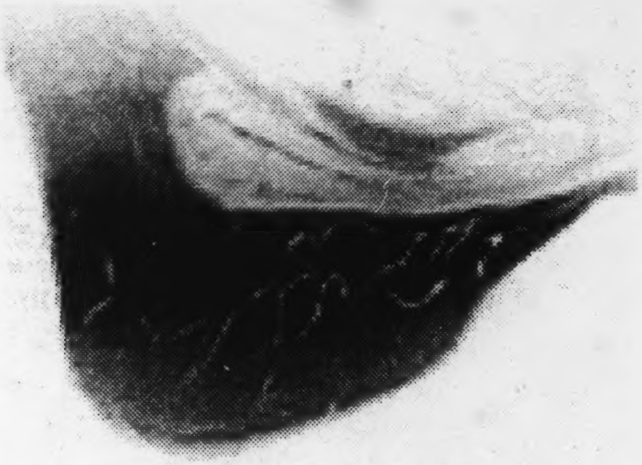

(a) blood vessels indicated by flow artefacts.

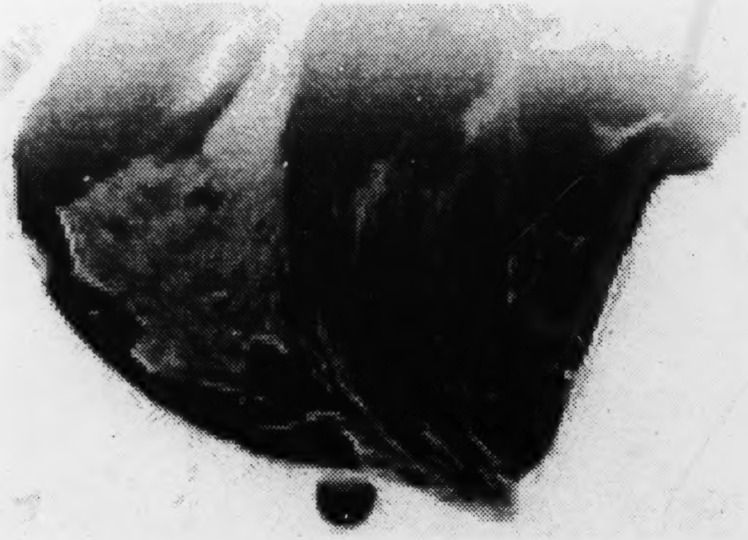

(b) ducts spread into the breast from behind the nipple.
(Marker sphere at bottom centre.)

Figure 8.1.2 (a) blood vessels and (b) ducts can be readily identified on images of the breast.

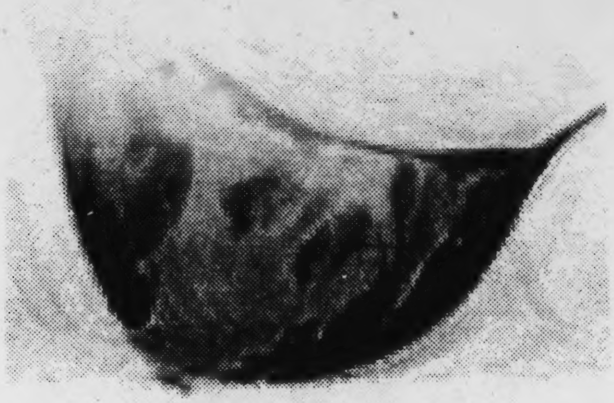

(a) premenopausal breast.

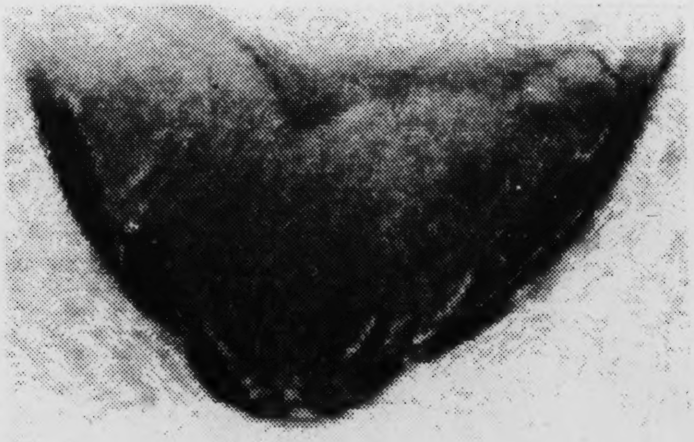

(b) lactational breast.

Figure 8.1.3 (a) premenopausal and (b) lactational breasts.

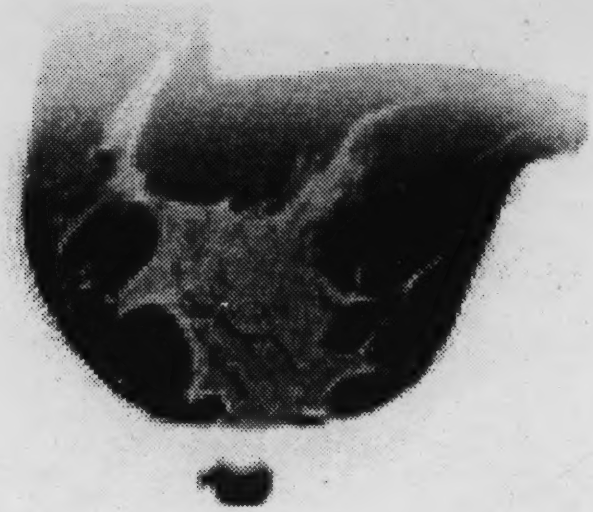

(a) premenopausal breast.

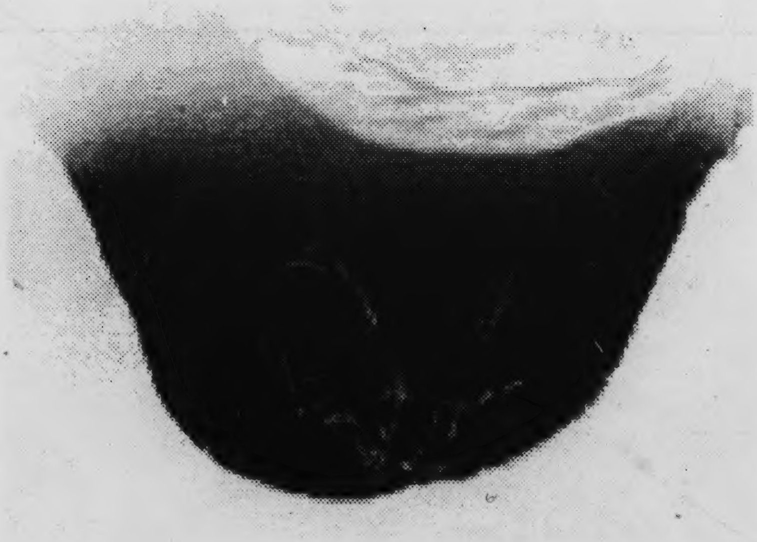

(b) postmenopausal breast.

Figure 8.1.4 (a) premenopausal and (b) postmenopausal breasts.

Obesity

Obesity affects the relative fat content of breasts. Figure 8.1.5 compares, for women of similar age and height, images of a woman of normal build (a), with a woman approximately 40 lbs. overweight (b).

Balance

A variation in breast size between left and right breasts is often seen, and Figure 8.1.6 shows that the internal structure can differ between the breasts.

8.2 Numerical data from the images

The breast images obtained from normal volunteers (see Section 8.1) were seen to contain regions of high intensity (dark on image examples) extending inwards into the gland from the skin, and regions of low intensity spreading into the gland from behind the nipple. The low-intensity regions were taken as being fibroglandular tissue, as suggested by Stelling *et al* [1985] and Dash *et al* [1986] with the high-intensity regions corresponding to fatty tissue. In order to correlate the images with spectroscopy data, and with the patient parameters of menstrual status, parity and age, the areas of high and low intensity were measured from the six images taken for each volunteer, and summed to give an estimate of the high/low intensity ratio in the spectroscopy volumes and over the whole gland, and the overall gland size. The volumes measured are shown in Figure 8.2.1. Because of the inhomogeneity of the breast coil it is not possible to give a single reference above which the intensity is defined as high and below which low, since this reference changes over the image.

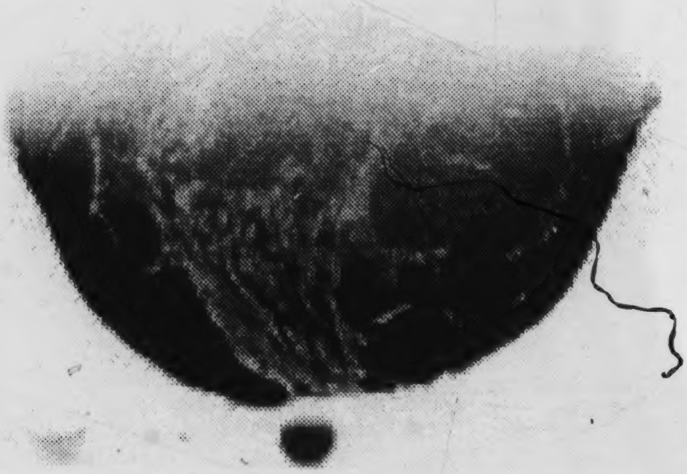

(a) premenopausal breast of woman of normal build.

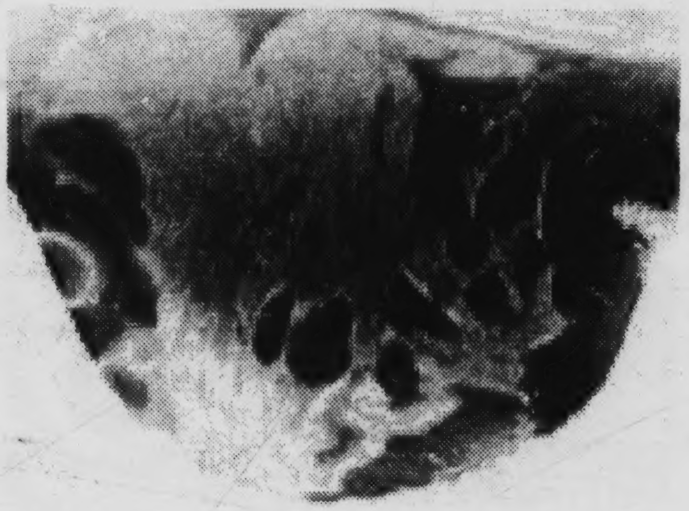

(b) premenopausal breast of obese woman.

Figure 8.1.5 (a) normal and (b) obese premenopausal breasts.

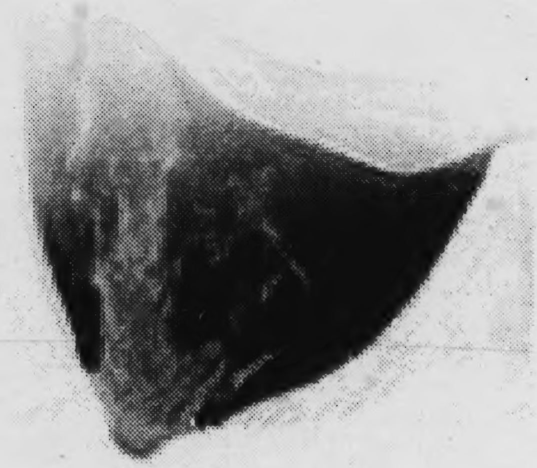

(a) left breast.

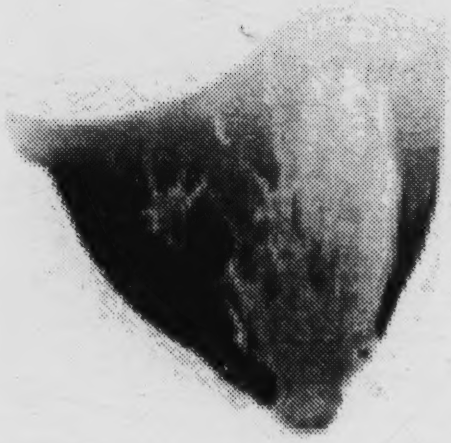

(b) right breast.

Figure 8.1.6 (a) left and (b) right breasts of a 24-year-old nulliparous woman.

However, near the centre of an average breast image, and with the intensity of the image defined as 0 = white and 1 = black, a level of 0.6 could be used to discriminate high from low intensity regions.

The actual procedure used for measuring the high/low intensity ratio was to cover the image with a carefully aligned transparent grid which showed the regions used in the spectroscopy. Squares in the grid which fell over low and high intensity regions were counted separately and their ratio calculated. Results of this measurement are shown in Table 8.2.1. % low in gland is calculated by 100% x low in gland / (high + low in gland). The unit of volume is 0.125 ml.

8.3 Preliminary interpretation of image data.

The '% low in gland' mentioned in Table 8.2.1 is associated with the amount of glandular material in the breast. Consequently this is expected to be related to the menstrual status (premenopausal, postmenopausal, lactating) of the woman. Classification of the '% of low in gland' into the three categories of menstrual status shows clearly that lactating women tend to have more gland tissue than the average for premenopausal women, and that postmenopausal women have less. When parity is included in the premenopausal case, four classes are distinguishable. Figure 8.3.1 shows the variation seen in four classes of women in this study.

Statistical analysis of the data in Table 8.2.1 is shown in Table 8.3.1. Scheffe's test indicates that there is a statistically significant difference between the following pairs of groups: lactational / nulliparous premenopausal, lactational / postmenopausal and multiparous premenopausal / postmenopausal.

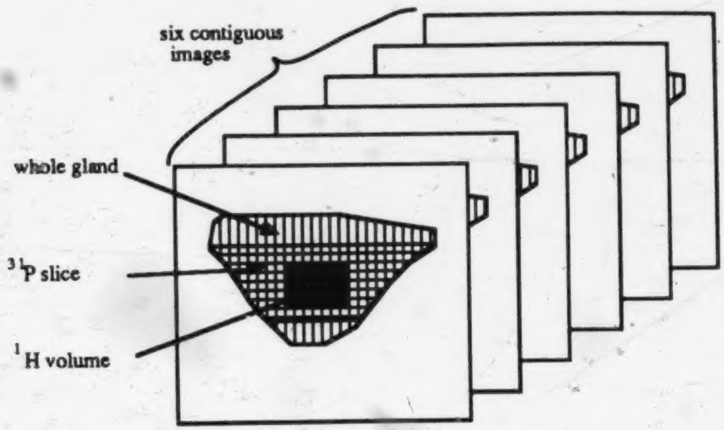

Figure 8.2.1 Volumes over which high/low intensity ratio measured.

volunteer number	high/low in cube	high/low in slice	high in gland	low in gland	high/low in gland	% low in gland	menstrual status
3	0.67	1.30	310	146	2.12	32.0	pre A
4	3.36	1.55	566	296	1.91	34.3	pre B
5	0.57	1.53	490	201	2.44	29.1	pre A
7	-	-	262	261	1.00	49.9	pre B
9	1.46	4.56	637	96	6.64	13.1	pre A
10	2.43	2.80	661	158	4.18	19.3	pre B
11	2.43	1.37	690	394	1.75	36.3	pre B
12	-	-	197	33	5.97	14.3	post
13	2.84	3.18	698	156	4.47	18.3	post
14	0.03	-	311	424	0.73	57.7	lac
15	2.69	3.62	718	177	4.06	19.8	post
16	2.05	4.08	520	100	5.20	16.1	post
17	0.35	-	669	564	1.19	45.7	pre B
19b	0.71	1.91	504	208	2.42	29.2	pre A
19d	0.92	-	410	240	1.71	36.9	pre A
20b	2.20	2.55	718	268	2.68	27.2	pre A
20c	2.31	-	710	215	3.30	23.2	pre A
20d	3.57	-	734	250	2.94	25.4	pre A
21	0.85	1.66	514	176	2.92	25.5	post
22a	2.37	2.66	648	223	2.91	25.6	pre A
23	7.67	-	156	142	1.10	47.7	pre A
25	0.07	-	203	449	0.45	68.9	lac
26	0.41	1.40	648	370	1.75	36.3	lac
27	-	-	324	441	0.74	57.6	pre B
29	-	-	257	501	0.51	66.1	lac

Table 8.2.1 Data measured from the normal volunteer images (pre A = nulliparous premenopausal, pre B = multiparous premenopausal, lac = lactational, post = postmenopausal)

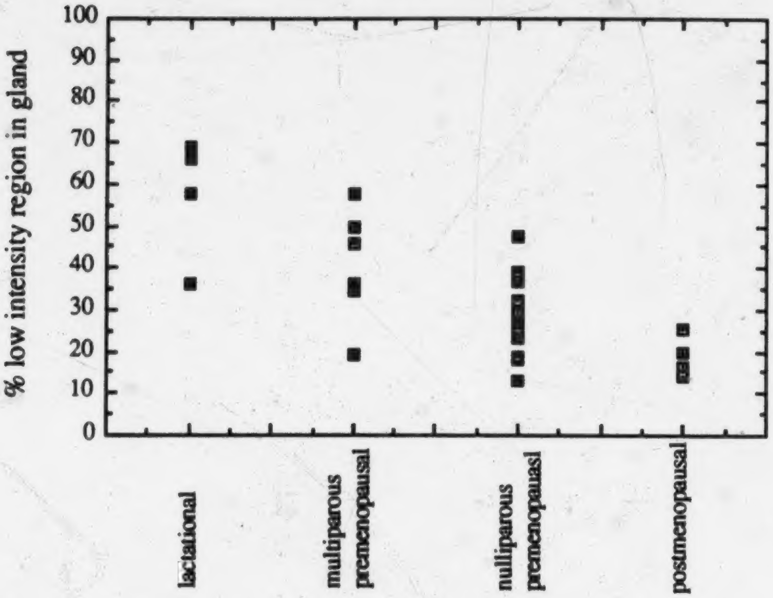

Figure 8.3.1 Correlation of low intensity regions in breast images as percentage of total breast with menstrual status of women.

Dependent variable : % low intensity region in gland.

source	degrees of freedom	sum of squares	mean square	f value	pr>f	Rsquare	c.v.
model	3	3729.9	1243.3	10.25	0.0003	0.6180	31.49
error	19	2305.5	121.3				
total	22	6035.4					

Result of Scheffe's test

grouping		mean	N	menstrual status
	A	57.25	4	lactational
B	A	40.52	6	multiparous premenopausal
B	C	29.33	9	nulliparous premenopausal
	C	17.12	4	postmenopausal

Table 8.3.1 Analysis of variance and Scheffe's test on imaging data.

8.4 A possible breast image correction technique.

Images taken with the breast coil exhibit inhomogeneous levels due to sample variations and also two factors, the variation of tip angle with position and the variation of receiver sensitivity with distance. The signal from regions where the tip angle is 'close' to $\pi/2, 3\pi/2$ etc. can be corrected to have the value that they would have if they had received a $\pi/2$ tip angle, and a uniform receiver sensitivity. The corrections require the field distribution of the coil to be known. The $B_\perp$ (see Section 2.4) component of the field can then be used to correct the image, so that the image pixel intensities reflect true spin densities and relaxation times, unmodulated by coil characteristics. It should be borne in mind that correction will boost the background noise along with the wanted image signal, and this could result in misleading images if the correction factor is too high. This is the reason for applying correction only to regions where the tip angle is close to $\pi/2$, $3\pi/2$ etc.. When the tip angle is near π, 2π etc. the signal to noise ratio will be low, and correction should not be performed.

The purpose of the image correction performed in this work was firstly to improve the quality and diagnostic usefulness of the images. The second purpose was the possibility of measuring the areas of different tissue type by automatically counting pixels with the same intensity rather than using the manual method of Section 8.2. It appeared from the images that the fat would have had a fairly uniform intensity if it were not for the surface coil sensitivity variation.

The field distribution of the breast coil was calculated using numerical integration and the COIL program (Section 6.1 and Appendix A). Field files were produced for B_X , B_Y and B_Z, but only B_X and B_Y were combined to give $B_\perp$. This was because the z direction for the calculation was taken as being along the B_0 field and thus did not have an effect on the nuclear spins. The axis of the coil was taken as along the y axis for the calculation, but any direction in the xy plane would have given the same result for $B_\perp$, since it is given by

$$B_\perp = (B_x{}^2 + B_y{}^2)^{1/2} \qquad (8 - 1)$$

The coil geometry used is shown in Figure 8.4.1. The three turn modified conical helix was divided into 24 arc sections for the purposes of the calculation, each arc being 45°. The plane over which the field was calculated is indicated by the oblique rectangle. The plane is oblique so that it is parallel to the transverse plane of the patient bed, since for convenience the coils were rotated through 45° about their axes when being installed in the coil holders of the patient bed. The plane corresponds to an area larger than the breast coil and extending above the coil into what would be the pectoral muscle, lung and breast axilla of the patient. In this area above the coil the field naturally dies away in intensity, and the image fades. The correction could help the radiologist compare the axilla with the other parts of the breast.

The $B_\perp$ information was used to produce calculated sensitivity maps for the breast coil. For these maps the intensity was calculated from the equation

$$\text{expected received signal} \;\; \alpha \;\; \frac{B_\perp}{B90} \sin \frac{B_\perp}{B90}\frac{\pi}{2} \qquad (8 - 2)$$

These maps were produced by the program Sensitivity Maps in Appendix D. Equation (8-2) is described in detail in Appendix B on correction factors. The maps thus obtained correspond to what would be seen if the entire area in Figure 8.4.1 were filled with a homogeneous sample and images taken with the real coil.

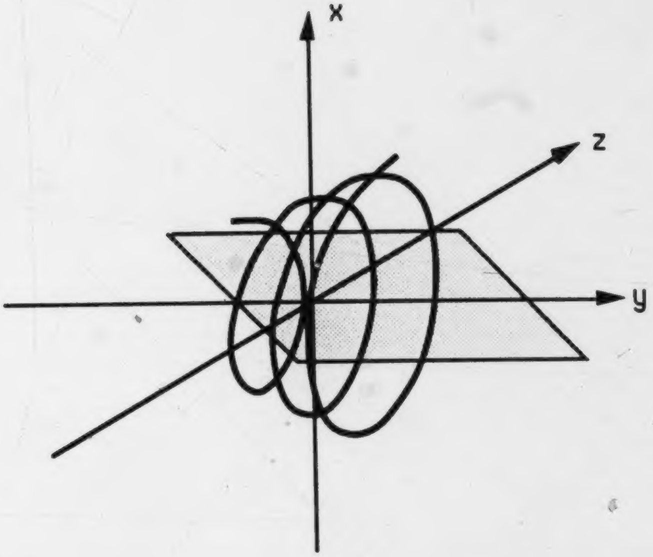

Figure 8.4.1 The plane through the breast coil used for calculated field sensitivity maps.

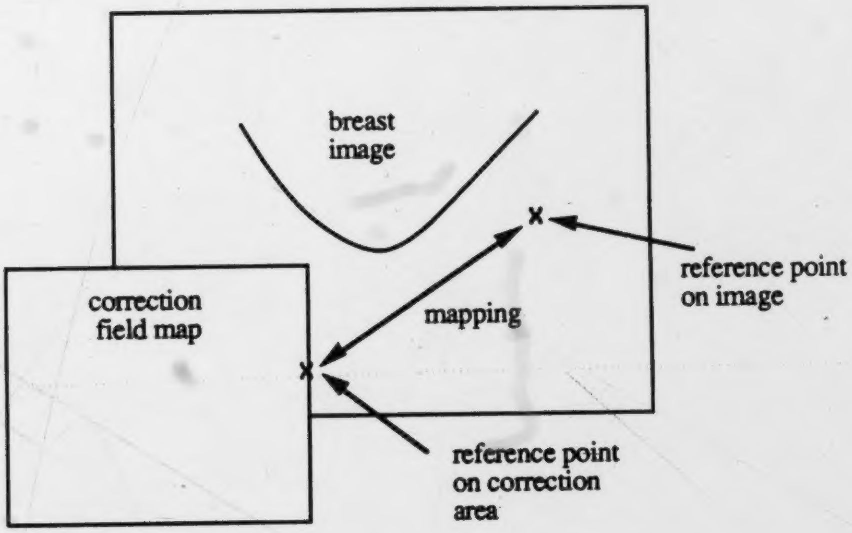
breast image
correction field map
mapping
reference point on image
reference point on correction area

Figure 8.4.3 Application of correction to a region of the image, to reduce the effects of surface coil inhomogeneity.

The only parameter in equation (8-2) is B_{90}, which is the $B_\perp$ field required to produce a 90° tip angle. The effect of varying this parameter is shown in Figure 8.4.2. When using the coil for imaging, care was taken to ensure that $B_\perp$ at the centre of the coil did not exceed B_{90}, since this would result in a band of zero intensity inside the part of the breast coil which would contain the breast as demonstrated in Figure 8.4.2(e). Since the breasts were kept away from the coils by an insulated acrylic cup, the high flux bands and zero intensity bands close to the wires were only seen at the very edges of the breasts, in which regions of skin and subcutaneous fat were not of great interest for this study.

Since the area over which the field was calculated was smaller than the imaging area used in this study, a program was written which would take the $B_\perp$ data and apply the correction to an image, aligning the overlaid correction area as shown in Figure 8.4.3 using reference points on both image and the correction area.

Since the pixel size is not necessarily the same in correction area and image, the program has the flexibility to locate the nearest correction area pixel to a particular pixel in the image. The program is described in more detail in Appendix D.

An example of a corrected image is given in Figure 8.4.4. Correction was only used where the signal had dropped to 25% of its value where the field was sufficient to give a 90° tip angle. The correction helps to make the region far from the wires more uniform, but introduces more inhomogeneity close to the wires and artefacts are introduced: dark regions near the coil and a grid pattern superimposed on the image. The former is caused by misalignment of the correction overlay and the latter by the coarseness of the overlay grid used here.

This chapter has demonstrated that quantitative data can be extracted from breast images manually, and that should this data be deemed valuable, a correction technique could enable automatic processing to speed up the quantification and render it more accurate. However in order to do this, attention will have to be paid to blood flow artefacts.

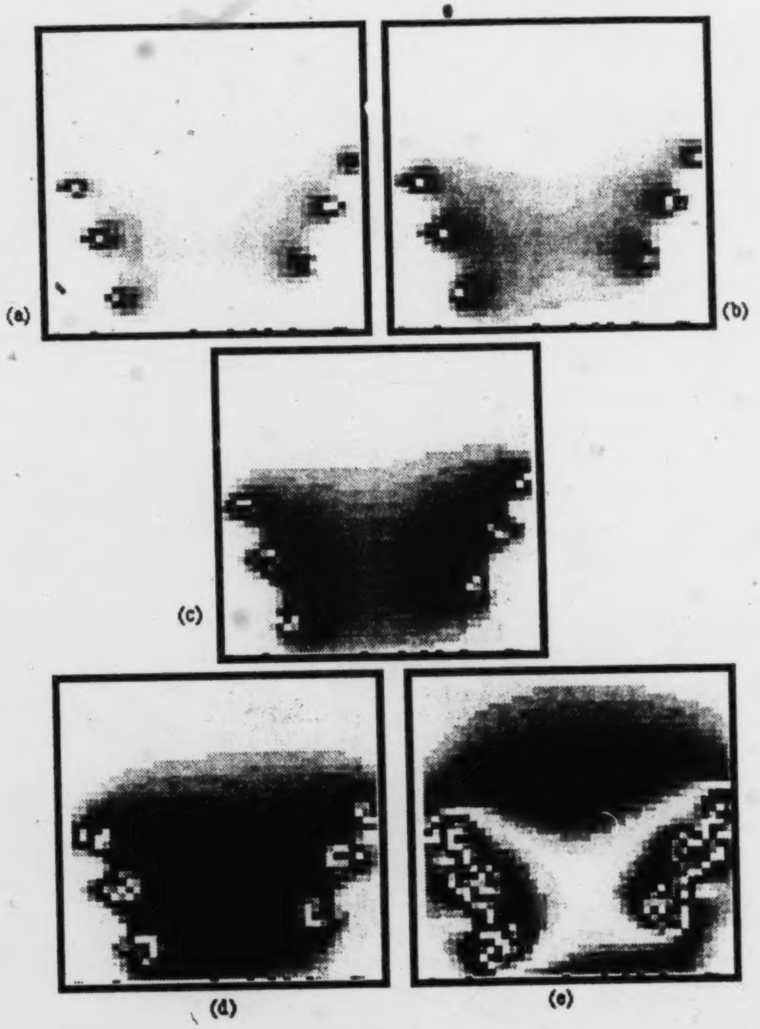

Figure 8.4.2 The calculated sensitivity maps for the breast coil when the field at the centre is less than B_{90} [(a) 0.4 B_{90}, (b) 0.5 B_{90}, (c) 0.7 B_{90}, (d) B_{90}] and greater than B_{90} [(e) 2 B_{90}] showing the banding which results if the field at the centre is greater than B_{90}

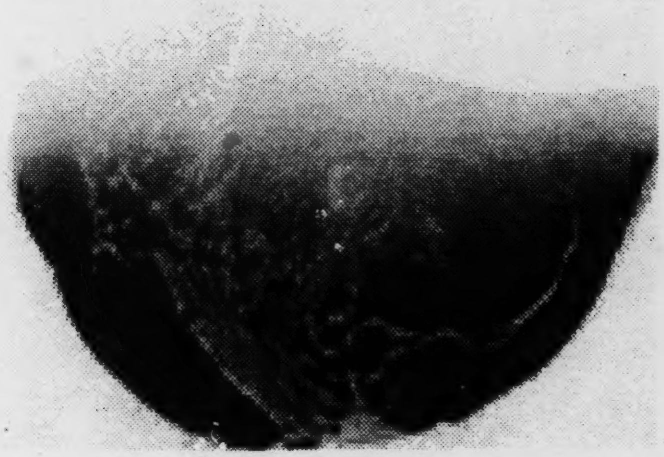

(a) uncorrected breast image.

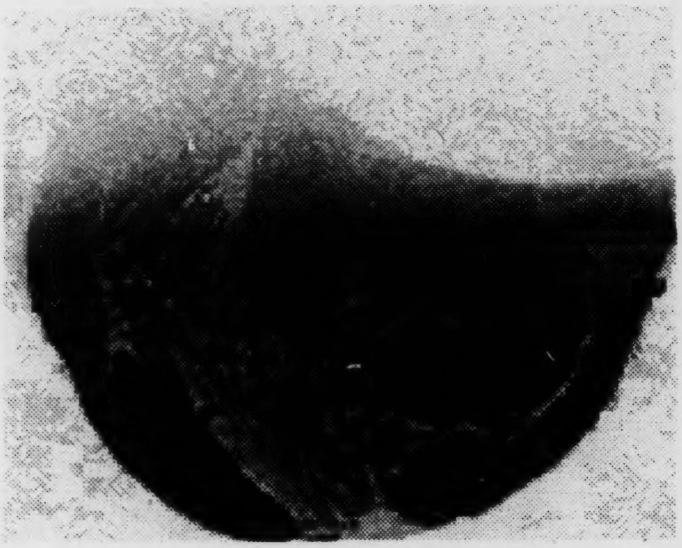

(b) corrected breast image.

Figure 8.4.4 (a) uncorrected and (b) corrected images using the image correcting technique.

CHAPTER 9

SPECTROSCOPY OF THE BREAST

In this chapter some of the spectra obtained during the normal volunteer trials are presented, and some correlation made between them and the image data described in Chapter 8. The purpose of this correlation was to identify which region from the images was associated with which parts of the proton and phosphorus spectra, and thus proportions of metabolites in the high and low intensity regions measured from the images.

9.1 Proton spectroscopy.

9.1.1 Spectra from normal volunteers

In the proton spectroscopy part of this study, ISIS (see Section 3.2.3.1) was used to localise to a 3x3x3cm volume near the centre of the breast. Thirteen breasts were examined, six premenopausal, three postmenopausal and four lactational. The spin echo sequence was used with a repetition time of 4s and an echo time of 100ms.

The range of fat:water ratio is indicated by the Figure 9.1.1. Figure 9.1.1(a) shows a proton spectrum from a lactational breast, processed using the NMRSPC programme developed here by Mrs. Ivy Ho and Dr. Carey.J.Gibson. The water peak is five times as large as the fat peak, giving a fat:water ratio of 0.2. In Figure 9.1.1(b) the proton spectrum of a post-menopausal breast shows a marked increase in fat at the expense of water, with a fat:water ratio of 4.9.

These findings are in agreement with the expected changes in the breast. The lactational breast has a high water content as the acini are gorged with milk, and the fat in the stroma has largely disappeared. The post menopausal breast has larger fat deposits which replace the involuted gland tissue, resulting in the high fat:water ratio.

(a) lactational breast

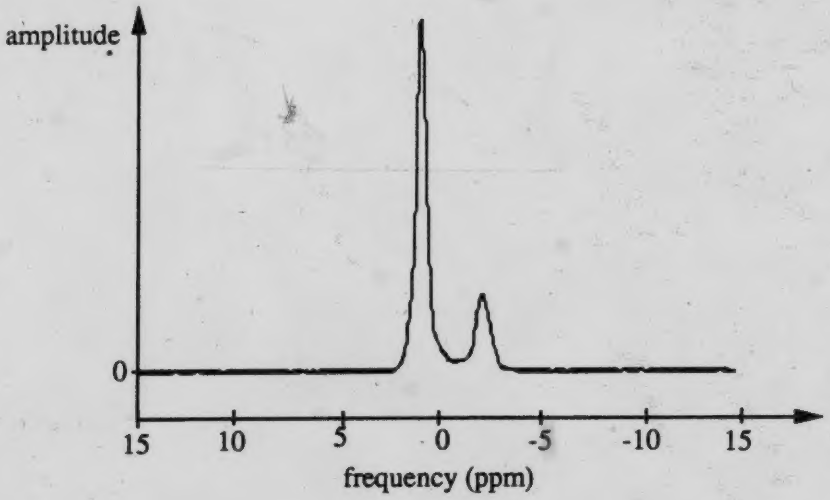

(b) post-menopausal breast

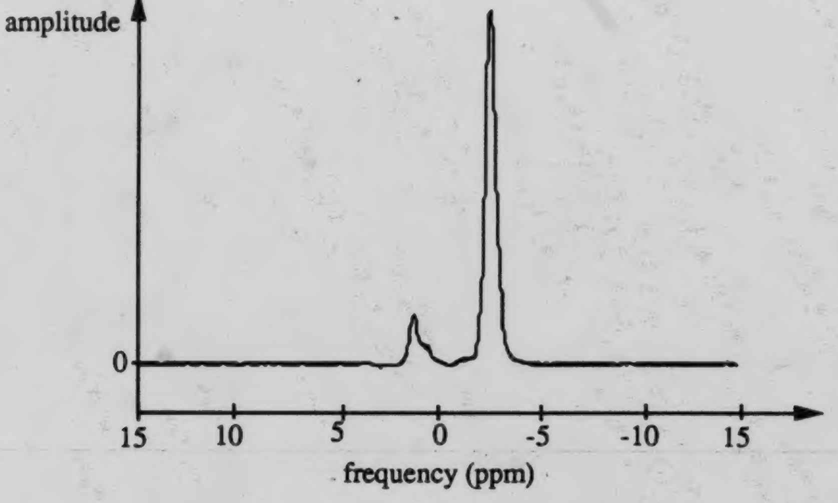

Figure 9.1.1 Proton spectra of (a) lactational and (b) post-menopausal breasts. The water peak is on the left, and the fat peak on the right.

9.1.2 Correlation of spectra with images.

In Section 8.2 results are given for the ratio of high intensity region in images (associated with fat in the interlobular stroma) to low intensity region in images (associated with the parenchyma) for the proton spectroscopy volume shown in Figure 8.2.1. The purpose of this part of the experiment was to attempt to correlate this imaging data with the proton spectroscopy fat/water ratio described in Section 9.1.1 and thus identify how the fat and water are distributed in the breast. The imaging data and the proton spectroscopy data were both from the same volume of gland. The data are presented in Table 9.1.2.1, and the correlation plotted in Figure 9.1.2.1. The regression coefficient for this correlation is 0.8.

menstrual state	high/low intensity region ratio from imaging of proton spectroscopy volume	fat/water ratio from spectroscopy of proton spectroscopy volume
lactational	0.03	0.21
lactational	0.07	0.11
lactational	0.41	1.1
lactational	0.05	0.42
premenopausal	0.35	1.0
premenopausal	0.71	1.87
premenopausal	0.92	2.97
premenopausal	2.31	3.9
premenopausal	3.57	5.18
premenopausal	2.37	3.95
postmenopausal	2.69	4.87
postmenopausal	2.05	6.08
postmenopausal	0.85	2.91

Table 9.1.2.1 Data from imaging and proton spectroscopy

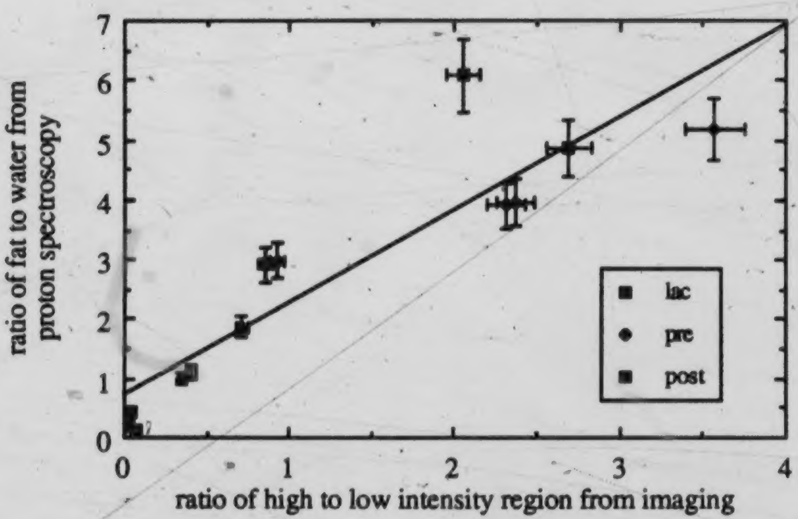

Figure 9.1.2.1 Correlation of imaging and proton spectroscopy data from the same volume of gland.

9.1.3 Preliminary interpretation of spectral data.

Figure 9.1.2.1 suggests that the assignment of the high intensity regions on the images to interlobular stroma is appropriate and that the low intensity regions are the main water containing parts of the breast, which would consist of the ducts and the gland lobules. The high/low-intensity region ratio is thus apparently equivalent to some form of the stroma/parenchyma ratio. Difficulties arose in measuring the volumes of the two regions from the images, especially in postmenopausal breasts with their tendency to the speckled distribution of fat (see Section 8.1 and Figure 8.1.1(b)). Problems of volume measurement also arose in breasts with high vascularity due to blood flow artefacts.

9.2 Phosphorus Spectroscopy

9.2.1 Spectra from normal volunteers.

Phosphorus spectra were obtained from a group of 13 normal volunteers, some of whom where the same as used in the proton spectroscopy study. Some experiments were performed without localization while all were performed with localization. With no localization the region from which the spectra were obtained included the entire breast, the muscle behind the breast and part of the arm. This resulted in a spectrum which did not reflect the true breast constituents. Large amounts of phosphocreatine were seen to be present in these spectra (see Figure 9.2.1). This arose from the pectoral muscle behind the breast.

Because of this problem of contamination from other parts of the body, localization was used. Since acquisition time was limited by patient comfort to about twenty minutes for this part of the breast experiments, the localized volume could not be made too small. A one-dimensional ISIS was used to localize to a slice transverse to the breast (coronal to the body) as shown in Figure 9.2.2. Slice thickness was

4.5 cm allowing a reasonable SNR (4 - 30, area of β ATP peak / rms noise) to be obtained in 256 acquisitions. The typical breast volume in the slice was approximately 400 ml. Because of the short relaxation time of some of the phosphorus metabolites a 90°-acquire sequence was used, following an ISIS localization sequence, and the repetition time was set to three seconds.

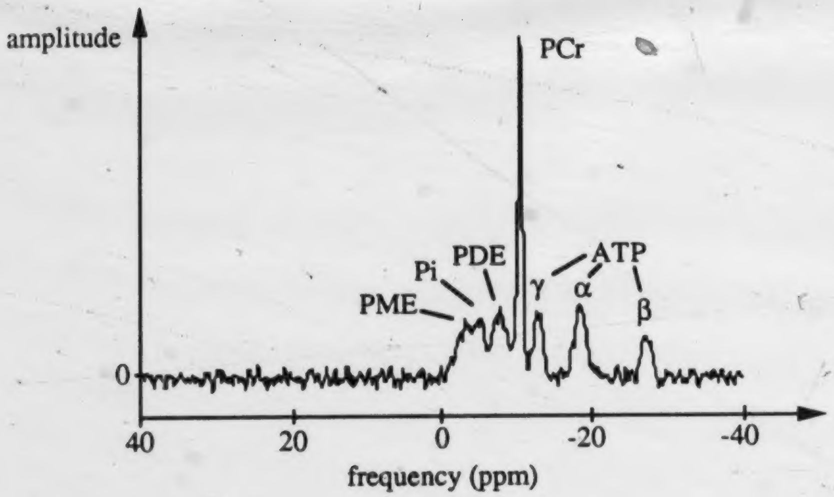

Figure 9.2.1 Unlocalized ^{31}P spectrum of the breast.

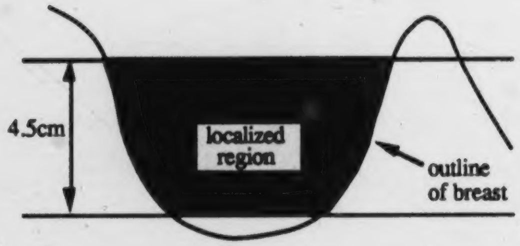

Figure 9.2.2 The selected slice for ^{31}P spectroscopy.

With this slice selection the phosphorus spectrum of the breast was considerably altered. The phosphocreatine disappeared, demonstrating that it did arise in the muscle (see Figure 9.2.3) and that the slice selection has effectively removed contamination of the breast gland spectrum by the muscle spectrum.

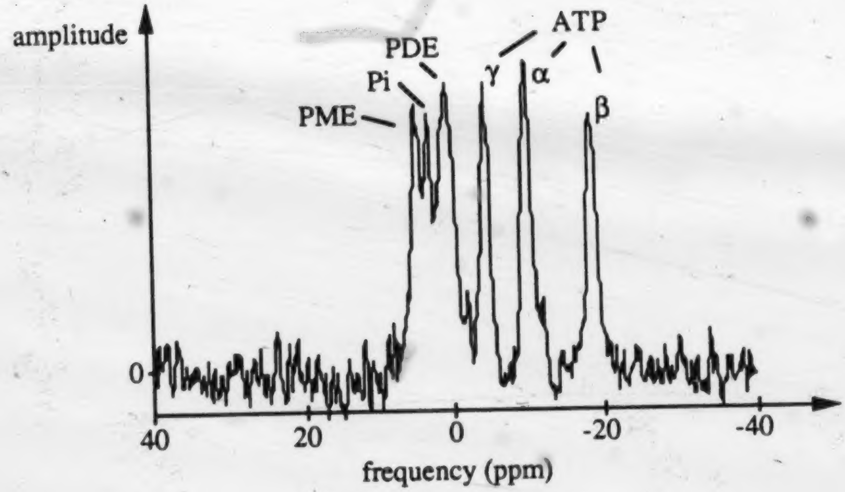

Figure 9.2.3 Localized ^{31}P spectrum of the breast.

9.2.2 Correlation of spectra with breast characteristics.

Correlations were attempted between the amount of high- and low-intensity regions in the breast images with the areas of the phosphorus-metabolite peaks from the phosphorus spectroscopy. The purpose of this was to determine which part of the breast (high-intensity region and low-intensity region on the images) was associated with which metabolite in the phosphorus spectrum. In order to able to compare the signal intensities directly, spectra were only used from breasts of approximately the same size, so that the loading of the breast coil was approximately the same, and that the power level used produced approximately the same tip angle distribution in the breast. There were nine such breasts, and the imaging and spectral data obtained from them are given in Table 9.2.2.1. Because of the inhomogeneity of the magnetic field of the breast coil across the volume of the breast, it was not appropriate to calibrate the phosphorus spectra against an external standard. However, with a knowledge of the magnetic field it would be possible to correct the spectra, using the images to determine the breast position and extent. This was not attempted here. The areas of the peaks are in units of volt parts-per-million (v ppm), since the signal level is measured in volts and where

$$\text{ppm} = 10^6 \times \frac{\text{offset frequency of peak from standard}}{\text{standard frequency}}$$

Figures 9.2.2.1 and 9.2.2.2 show the correlation between the total phosphorus signal (measured by adding the areas of all the peaks) and the volumes of low- and high-intensity regions in the equivalent region from the six images. This suggests that the phosphorus metabolites were concentrated in the low intensity region in the images, corresponding to the parenchyma. A graph which plotted total phosphous metabolites as a function of the ratio of high-to-low intensity region in the images would not have resulted in the linear correlation seen here, so this plot was not used in this case.

Figures 9.2.2.3 and 9.2.2.4 show the correlation between the individual γ, α and β peak areas of ATP in the phosphorus spectra from the nine breasts which filled the breast cups and the areas of low and high intensity regions in the equivalent volume from the six images. Individual peaks were plotted to determine if there was

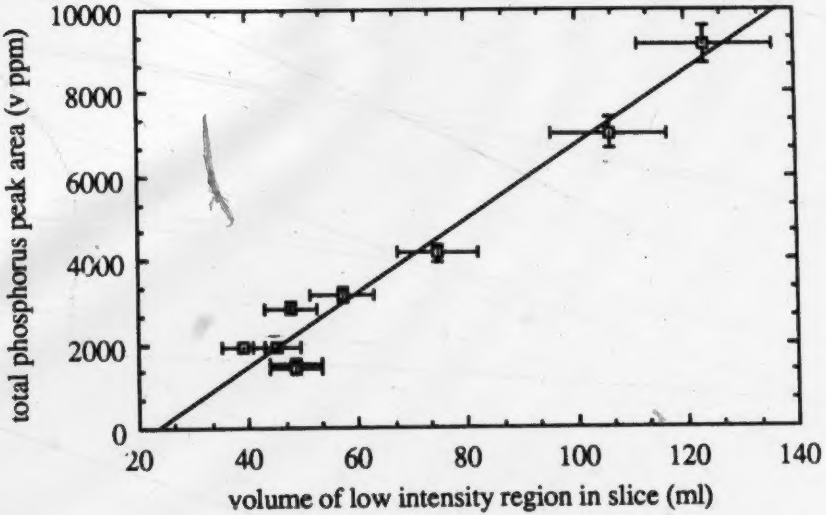

Figure 9.2.2.1 Correlation of total phosphorus peak area with volume of low intensity region from equivalent volume in images.

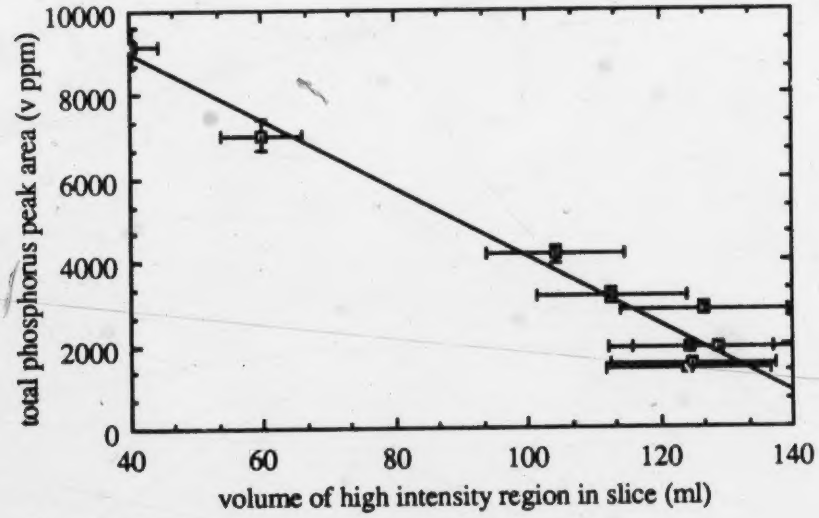

Figure 9.2.2.2 Correlation of total phosphorus peak area with volume of high intensity region from equivalent volume in images.

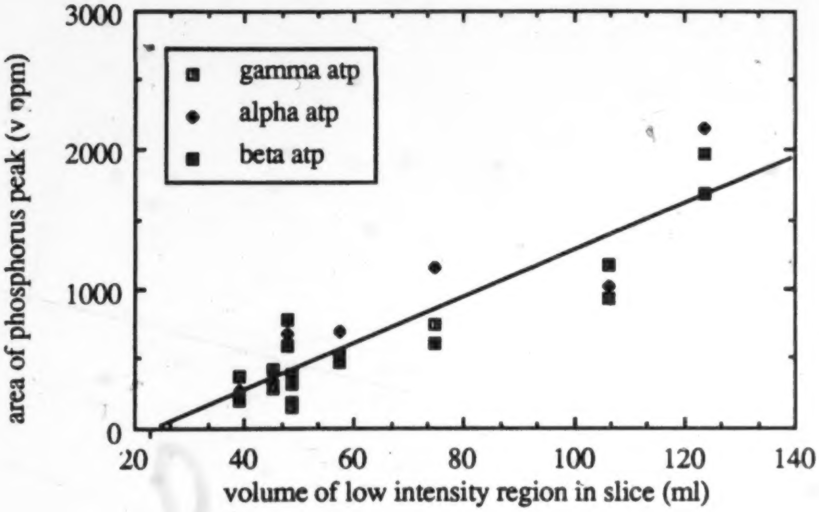

Figure 9.2.2.3 Correlation of ATP peak areas with volume of low intensity region from equivalent region in images.

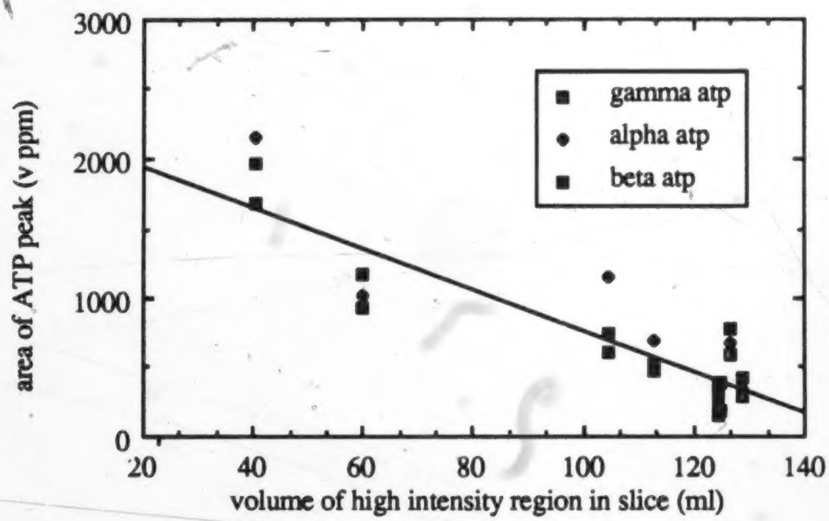

Figure 9.2.2.4 Correlation of area of the ATP peaks with volume of high intensity region from the equivalent region in images.

any consistency in the ratios within peak areas. This did not seem to be the case, suggesting that the areas are approximately the same, as expected, but with random error. Error bars are omitted for clarity, but estimated y error is 5% and estimated x error is 10%.

high inten region (ml)	low inten region (ml)	γATP (V ppm)	αATP (V ppm)	βATP (V ppm)	PME (V ppm)	Pi (V ppm)	PDE (V ppm)
125	39	378	270	205	351	406	716
125	49	179	376	382	260	327	355
129	45	421	334	294	143	392	754
124	49	147	322	323	285	147	351
127	48	594	673	784	247	947	549
113	57	532	690	467	513	505	964
104	75	750	1158	613	721	629	911
40	124	1670	2150	1973	1230	1294	2143
60	106	1166	1011	933	1583	0	2337

Table 9.2.2.1 Imaging and spectral data from breasts filling the breast coil cups.

Figures 9.2.2.5 and 9.2.2.6 show the correlation between the areas of the phospholipid peaks in the phosphorus spectra from the nine breasts which filled the breast cups and the volumes of low and high intensity regions in the equivalent region from the six images.

9.2.3 Preliminary interpretation of spectral data.

The graphs in Section 9.2.2 indicate clearly that the phosphorus metabolites are mainly located in the parenchyma tissue of the breast, rather than in the fatty interlobular stroma. This is in agreement with a model of the fatty interlobular stroma as consisting primarily of adipose cells, with most of the cell volume consisting of triglycerides. From Figures 9.2.2.5 and 9.2.2.6 the phospholipids are mostly located

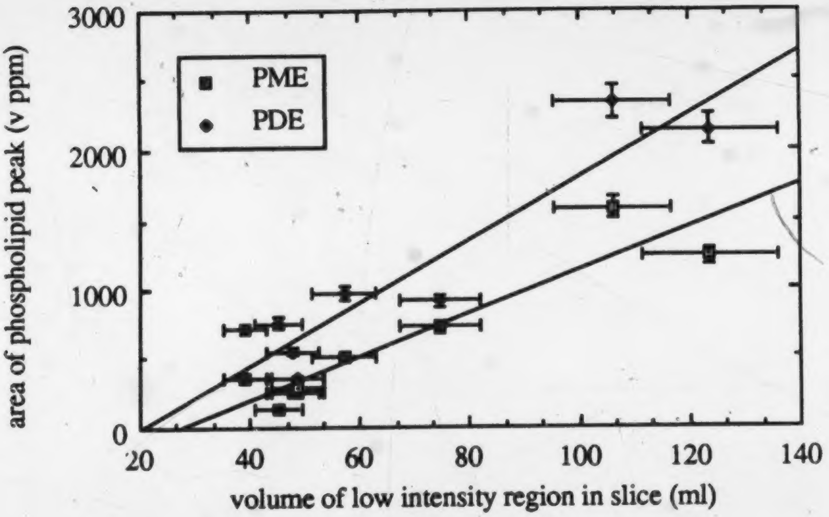

Figure 9.2.2.5 Correlation of areas of phospholipid peak areas with volume of low intensity region from equivalent volume in images.

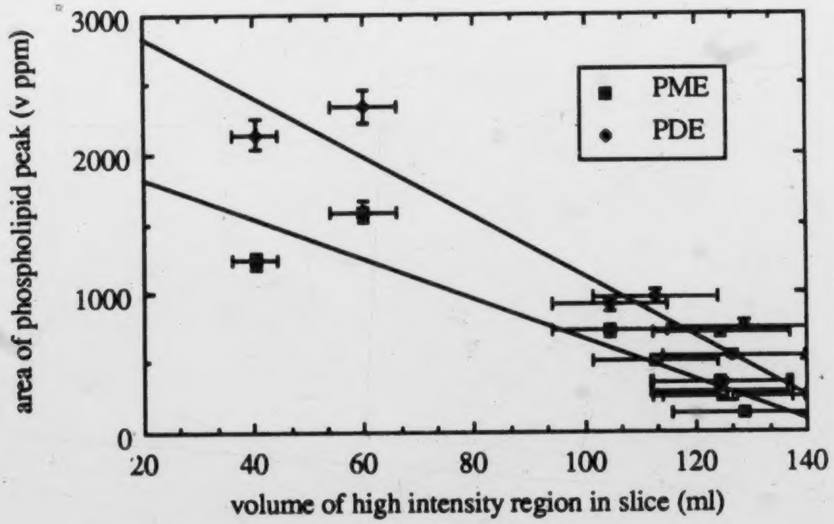

Figure 9.2.2.6 Correlation of phospholipid peak area with volume of high intensity region from equivalent volume in images.

in the parenchyma, and the phosphodiesters are consistently at a higher level than the phosphomonoesters. Since these phospholipids are precursors (phosphomonoesters) and postcursors (phosphodiesters) of membrane phospholipids, they would both be expected to be present in tissue which is constantly replacing cells. The correlation of phospholipids with parenchyma suggests that imaging data could be used to predict the expected levels of phospholipids in a breast. With reports that phospholipids are important in treatment monitoring of tumours [Sijens *et al*, 1987, Glaholm *et al*, 1989], being able to predict normal levels would appear important.

One important note that needs to be made here is that the volume of high and low intensity region measured from the images did not cover the entire breast, but a three cm slice through the centre of the breast. While this does not affect the significance of the results in this chapter, it means that it is not possible to quantify the molarity of phosphorus metabolites in the breast. Any future study would need to cover the entire breast by increasing the number of slices, and for this analysis it would be advisable to use computer image processing and analysis, as suggested in Section 8.4. Another solution would be to localize to a smaller volume of breast, but this would reduce the signal-to-noise ratio, which is already not high.

The problem of the correction of the spectra for breast size and position in the field from the breast coil needs to be addressed. Since the magnetic field distribution is known, it will be possible to integrate the expected signal (see Appendix B) over the volume of parenchyma in the breast, and use this as a correction factor for the phosphorus spectra. This would lead to the ability to predict metabolite levels, and recognition of excessively high or low amounts of particular metabolites.

CHAPTER 10

CONCLUSIONS

The breast coil design described in Chapter 6 has a much higher signal-noise-ratio than the body coil, as shown in Section 6.4. It has produced quality images as shown in Chapter 8, and good-quality proton and phosphorus spectra, as shown in Chapter 9.

This study has been able to demonstrate that the water signal observed in proton NMR spectra of the breast arises mainly in the region of the breast which appears of low intensity in the images of the breast described in Chapters 7 and 8. The fat signal appears to be associated with the high-intensity region on the images. I postulate that this indicates that the water signal arises mainly in the parenchyma of the breast and the fat signal in the interlobular stroma. This is supported by the phosphorus NMR spectroscopy studies which indicate that the phosphorus metabolites originate in the same region as the water, and not in the region containing mostly fat. This is in agreement with phosphorus metabolites having a much higher concentration per unit volume in gland cells than in adipose cells, which are mainly filled with triglycerides.

It has been suggested that NMR spectroscopy of the human breast be used for the monitoring of chemotherapy for cancer treatment. To quantize metabolite concentrations the entire breast would need to be imaged, requiring a large amount of image analysis. In the present study the image analysis was done by hand. It would be advisable to use computer image processing and analysis for future studies. This would seem to be feasible from the image correction suggested in Section 8.4 . With a knowledge of the volume of parenchyma in the breast, and the metabolite concentrations expected in the normal parenchyma, monitoring of breast cancer treatment by NMR spectroscopy would appear to have potential as a non-invasive adjunct modality .

In order to analyze the images accurately into the different parts of the breast, it would be helpful to use T_2 relaxation time measurements taken from multi-echo images. A computer algorithm could be written that would not only discriminate between levels in a single image, but would discriminate within levels according to the relaxation time. This could assist in separating the low-intensity region seen on images in this study into blood vessels, ducts and other components, enabling a better correlation with the spectroscopy data.

Shimming was a slow process in the spectroscopy studies described here, and since the time that a breast cancer patient spends on the patient bed should be kept as short as possible to avoid discomfort, it would be advisable to move to automatic shimming in future work.

It was difficult to obtain phosphorus spectra from some postmenopausal breasts because of the low signal-to-noise ratio caused by the low parenchyma volume and the poor fill-factor of the coil. Shallower coils should be constructed for the smaller breasted woman, to increase the fill factor. Similarly, larger coils will be needed for women with breast tumours, especially stage 4 tumours.

It was shown in Section 9.2 that the level of PDE was consistently higher than the PME level. Glaholm *et al* [1989] have suggested that PME can be used as an indicator of tumour condition, since it may reflect the level of cell membrane synthesis and thus the rate of cell replication. The combination of the two peaks "provides a window through which to observe phospholipid biosynthesis in cells" [Cohen, 1988 p1203]. PMEs are reported to have a low concentration in nonproliferating tissu[illegible] *et al*, 1987]. With PME on the synthesis side and PDE on the degradation side of phospholipid metabolism, it is likely that the PDE/PME ratio will drop in tumours which are proliferating. Both this ratio and the absolute concentrations of phospholipids could be used in monitoring the phospholipid metabolism of tumours.

This study has shown that it is possible to correlate a breast spectrum with NMR images of the breast, and thus to normalize spectra according to the volume of breast components. It is hoped that similar techniques will be used in the future to produce calibrated normal-metabolite-concentration reference spectra for the breast and other organs through a combination of spatial localization, surface coil inhomogeneity correction, relaxation time measurement and NMR imaging.

REFERENCES

Abragam , A *The Principles of Nuclear Magnetism*, Clarendon Press, Oxford, 1961.

Abramowicz, M and I A Stegun, *Handbook of mathematical functions*, Dover 1965.

Aue, W P, S Muller, T A Cross and J Seeling, "Volume selective excitation. A novel approach to topical NMR", J. Magn. Reson. **56**:2, 350 (1984).

Bendall, M R, "Elimination of high-flux signals near surface coils and field gradient sample localization using depth pulses", J. Magn. Reson. **59**, 406 (1984).

Bendall, M R and D T Pegg, "Uniform sample excitation with surface coils for *in vivo* spectroscopy by adiabatic rapid half passage", J. Magn. Reson.**67**, 376 (1986).

Bendall, M R and R E Gordon, "Depth and refocussing pulses designed for multipulse NMR with surface coils", J. Magn. Reson.**53**, 365 (1983).

Bottomley, P A, T B Foster and R D Darrow,"Depth-resolved surface-coil spectroscopy (DRESS) for *in vivo* ^{1}H, ^{31}P and ^{13}C NMR", J. Magn. Reson. **59**, 338 (1984).

Bovey , F A, *Nuclear Magnetic Resonance Spectroscopy*, Academic Press, New York, 1969.

Cohen, J S, "Phospholipid energy metabolism of cancer cells monitored by ^{31}P magnetic resonance spectroscopy: possible clinical significance", Mayo Clin. Proc. **63**, 1199 (1988).

Corio, P L, *Structure of High-Resolution NMR Spectra*, Academic Press, New York, 1967.

Daly, P F, R C Lyon, P J Faustino and J S Cohen, "Phospholipid metabolism in cancer cells monitored by ^{31}P spectroscopy", J. Biol. Chem., **262**:31, 14875 (1987).

Dash, N., A R Lupetin, R H Daffner, Z L Deeb, R J Sefczek and R L Shapiro, "Magnetic resonance imaging in the diagnosis of breast disease", AJR **146**, 119 Jan (1986).

Durham, R M, *Human Physiology*, Wm C Brown, Iowa, 1989.

Edelstein, W A, J M S Hutchison, G Johnson and T W Redpath, "Spin warp NMR imaging and applications to human whole body imaging", Phys. Med. Biol. **25**, 751 (1980).

Edminster, J A, *Electromagnetics*, McGraw Hill, USA, 1979.

Ernst, R R, G Bodenhausen and A Wohaun, *Principles of Nuclear Magnetic Resonance in One and Two Dimensions*, Oxford Science Pubs., 1987.

Farrar, T C and E D Becker, *Pulse and Fourier transform NMR*, Academic Press, 1971.

Fox, S I, *Human Physiology*, Wm C Brown, Iowa, 1984.

Fullerton, G D, "Physiologic basis of magnetic relaxation" in *Magnetic Resonance Imaging*, D D Stark and W G Bradley eds, 37, C V Mosby Co., 1988.

Gallagher, H S et al eds, *The Breast*, C V Mosby Co, St Louis, 1978.

Garroway, A N, P K Grannel and P Mansfield, "Image formation in NMR by a selective irradiative process", J.Phys.C 7:24 , L457 (1974).

Glaholm,J, M O Leach, D J Collins, J Mansi, J C Sharp, A Madden, I E Smith and V R McCready,"*In vivo* ^{31}P magnetic resonance spectroscopy for monitoring treatment response in breast cancer", The Lancet, June 10 (1989).

Gordon, R E, P E Harley and D Shaw, "Topical magnetic resonance", Proc. Nucl. Magn. Resonance Spectrosc. **15**:1-2, 1 (1982).

Haas, A and J Frahm , "Multiple chemical-shift-selective NMR imaging using stimulated echoes", J. Magn. Reson. **64**, 94 (1985).

Hahn, E L, "Spin echoes", Phys. Rev. **80**, 580 (1950).

Harpen, M D, "Sample noise with circular surface coils", Med. Phys. **14**, 4 Jul/Aug (1987).

Hendrick, R E, "Image contrast and noise" in *Magnetic Resonance Imaging*, D D Stark and W G Bradley eds, 67, C V Mosby Co., 1988.

Heywang, S H, G Fenzl, D Hahn, I Krischke, M Edmaier, W Eiermann and R Bassermann, "MR imaging of the breast: comparison with mammography and ultrasound", J. Comput. Assist. Tomogr., **10**, 4 (1986).

Hinshaw, W S," Spin mapping: the application of moving gradients to NMR", Phys. Lett. **A48**:2, 87 (1974).

Hinshaw, W S, " Image formation by nuclear magnetic resonance: the sensitive point method", J. Appl. Phys., **47**:8, 3709 (1976).

Hornak, J P, J Szumowski and R G Bryant," Elementary single turn solenoids used as the transmitter and receiver in magnetic resonance imaging", Magnetic Resonance Imaging, **5**, 233 (1987).

Hoult, D I and R E Richards," The signal-to-noise ratio of the nuclear magnetic resonance experiment", J. Magn. Reson., **24**, 71 (1976).

Jardetzky, O and G C K Roberts, *NMR in Molecular Biology*, Academic Press, Florida, 1981.

Johnson, G, J M S Hutchison, T W Redpath and L M Eastwood, " Improvements in performance time for simultaneous three-dimensional NMR imaging", J. Magn. Reson., **54**, 374 (1983).

Kroeker, R M, C A Stewart, M J Bronskill and R M Henkelman, "Continuous distributions of NMR relaxation times applied to tumors before and after therapy with x-rays and Cyclophosphamide", J.Magn.Reson.,**6**, 24 (1988).

Lauterbur, P C, "Image formation by induced local interactions:examples employing nuclear magnetic resonance", Nature **242**:5394, 190, 1973.

Lorrain, P, D R Corson and F Lorrain, *Electromagnetic Fields and Waves*, 3rd ed., W H Freeman, New York, 1987.

Luyten, P R and J A den Hollander, "^{1}H MR spatially resolved spectroscopy of human tissues *in situ* ", Magn. Resonance Imaging, **4**:3, 237 (1986).

Mansfield, P and P K Grannel, "NMR 'diffraction' in solids", J. Phys. C **6**:22, L422 (1973).

McOwan, P W and T W Redpath," A specialised receiver coil for NMR imaging of female breasts", Phys. Med. Biol. **32**:2, 259 (1987).

Moon, R B and J H Richards," Determination of intracellular pH by ^{31}P magnetic resonance", J. Biological Chemistry, **248**:20, 7276 (1973).

Morris, P G,"NMR spectroscopy in living systems", in *Annual Reports on NMR Spectroscopy*, G A Webb ed., 20, Academic Press, London, 1988.

Ordidge, R J, A Connelly and J A B Lohman," Image-selected *in vivo* spectroscopy (ISIS). A new technique for spatially selective NMR spectroscopy",J.Magn.Reson., **66**, 283 (1986).

Partain, C L, M V Kulkarni, R R Price, A C Fleischer, D L Page, A W Malcolm, A C Winfield and A E James jr.," Magnetic resonance imaging of the breast: functional T_1 and three-dimensional imaging", Cardiovasc. Intervent. Radiol. **8**, 292 (1986).

Philips Medical Systems, *Operator's Manual: Gyroscan Release 5.6* , 1989.

Rehman, I, "Embryology and anatomy of the breast" in *The Breast*, H S Gallagher *et al* eds, C V Mosby Co, StLouis, 1978.

Romeo, F and D I Hoult," Magnetic field profiling: analysis and correcting coil design", Magnetic Resonance in Medicine,1, 44 (1984).

Russo, J and I H Russo, "Devolopment of the human mammary gland" in *The Mammary Gland*, M C Neville and C W Daniel Eds, Plenum Press, New York and London, 1987.

Sijens, P E, H K Wijderman, M A Moerland, C J G Bakker, J W A H Vermeulen and P R Luyten,"Human breast cancer *in vivo* ^{1}H and ^{31}P MR spectroscopy at 1.5T",Radiology, **169**, 615 (1988).

Silver, M S, R I Joseph, C-N Chen, V J Sank and D I Hoult, " Selective population inversion in NMR", Nature, **310**:5979, 681 (1984).

Statistics Canada, Health Division, *Cancer in Canada 1983*, Ministry of Supply and Services, 82, 1988 catalogue.

Stelling, C B, P C Wang, A Lieber, S W S Mattingly, W O Griffen and D E Powell, "Prototype coil for magnetic resonance imaging of the female breast", Radiology, **154**, 457 (1985).

Tortora, G J and N P Anagnostakos, *Principles of Anatomy and Physiology* , 5th ed, Harper and Row, New York, 1987.

Turner, R, " A target field approach to optimal coil design", J.Phys.D:Appl.Phys.**19**, L147 (1986).

Tycko, R, E Schneider and A Pines, "Broadband population inversion in solid-state NMR", J.Chem.Phys. **81**:2, 680 (1984).

Ugurbil, K, M Garwood and M R Bendall, " Amplitude and frequency-modulated pulses to achieve 90^o plane rotations with inhomogeneous B_1 fields", J. Magn. Reson., **72**, 177 (1987).

Vorherr, H, *The Breast:Morphology, Physiology and Lactation*, Academic Press, New York, 1974.

Wehrli, F W, "Principles of magnetic resonance" in *Magnetic Resonance Imaging*, D D Stark and W G Bradley eds, 9, C V Mosby Co., 1988.

Wiener, J I, A C Chako, C W Merten, S Gross, E L Coffey and H L Stein, " Breast and axillary tissue MR imaging: correlation of signal intensities and relaxation times with pathologic findings", Radiology, **160**, 299 (1986).

Wilson, K J W, *Ross and Wilson's Anatomy and Physiology in Health and Illness*, 6th edition, Churchill Livingstone, 1987.

Wolfman, N T, R W Williams, B E Wall, P R Moran and N Karstaedt, "Design modification of dedicated MR breast coil", J. Comput. Assis. Tomogr. **10**, 5 (1986).

Appendix A

The COIL program.

This section describes the use of the COIL program, which enables a calculation of the field pattern from an arbitrary shaped coil to be calculated.

1. The coil description file.

This file consists of a series of arcs and lines which are used to describe the geometry of the coil. It also contains optional parameters which are used in the drawing and calculation of the field. This file is a simple text file so that editing can be done with any text editor. Each line is terminated with a carriage return <CR>. When you use the load command in the coil menu the text file is loaded into a text array, and the parameters replace the program default parameters.

Arcs and Lines

Lines are described by the word 'line' placed at the start of the textfile line and arcs by the word 'arc'. Next follow in both cases the start and end points of the line or arc. The order is important since the current flows from the start point to the end point. In addition, arcs have an extra point which defines the centre of curvature of the arc.

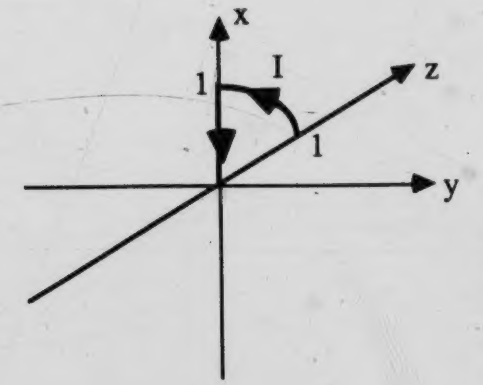

As an example the coil sections on the left would be described by

arc 001100000<CR>
line 100000<CR>
end<CR>
end<CR>

The format for the arcs and lines is

arc

'arc' - blank - start x - blank - start y - blank - start z - blank
- end x - blank - end y - blank - end z - blank
- centre x - blank - centre y - blank - centre z - blank - <CR>

line

'line' - blank - start x - blank - start y - blank - start z - blank
- end x - blank - end y - blank - end z - blank - <CR>

blank can be any number of spaces. Start x, etc must be in a format like:

123 123.4E-12 -123. .456 3e9 -0

Coil description part

The coil description part consists of a series of lines and arcs terminated by the line 'end' <CR>. In addition there may be comments which are lines which have an asterisk at the start. These are ignored when the coil data is loaded. The coil description part must be terminated by 'end' <CR>, and if there is no parameter part, there must be an additional 'end' <CR>. The following description would draw a circle in the xz plane.

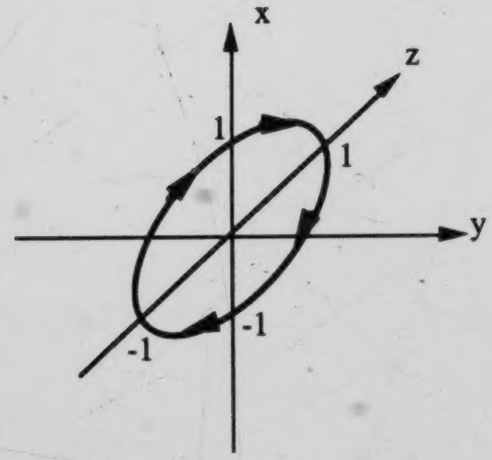

```
*circle in the XZ plane <CR>
arc 100 001 000<CR>
arc001-100 000 <CR>
arc-100 00-1 000 <CR>
arc00-1 100 000 <CR>
end <CR>
end <CR>
```

N.B. The maximum angle subtended by an arc is 90°. If this is exceeded the error message 'angle too big' will be given. There is no limit to the length of a line.

Parameters

The parameters set the position and scale of the coil drawing. They also set where the title is printed, and the segment length that each arc and line are divided into when drawing and calculating.

Position

The position that the coil is drawn on the screen is defined by the four parameters topleftx, toplefty, bottomrightx, bottomrighty.

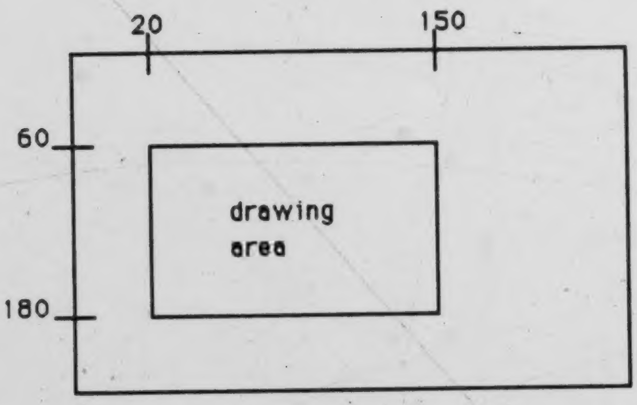

example (parameter section)

```
end<CR>
------------
topleftx=20<CR>
toplefty=60<CR>
bottomrightx=150<CR>
bottomrighty=180<CR>
end<CR>
-------------
```

These parameters control the size of the picture. The range of x,y and z plotted are set by xmax, ymax, zmax.

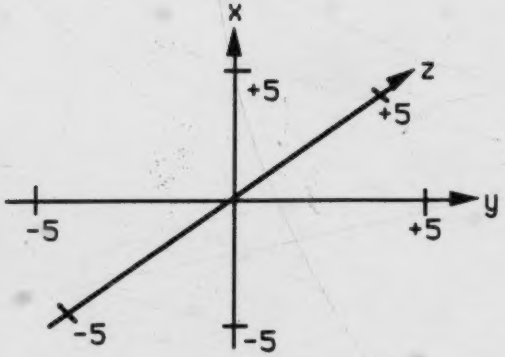

```
example(parameter section)
end<CR>
----------
xmax=5<CR>
ymax=5<CR>
zmax=5<CR>
end<CR>
----------
```

The title is controlled by three parameters which describe what it says and where it is printed.

```
example (parameter section)
end <CR>
----------
title=example title <CR>
titlex=20 <CR>
titley=20 <CR>
end <CR>
----------
```

The length of the segment is controlled by the parameter seglength. A large value of seglength can be used for rough drawing and calculation, and a small value for accurate drawing and calculation.

example (parameter section)

```
end <CR>
seglength=0.1 <CR>
end <CR>
```

Default values of the parameters

When loading a coil description which contains no values for a parameter, its value is set to its default value below:

topleftx	50
toplefty	50
bottomrightx	350
bottomrighty	350
title	<name of the coil file>
titlex	30
titley	30
seglength	0.1
xmax	2
ymax	2
zmax	2
zangle	0.53

The field data files

The output of the COIL program is in the form of three data files, for the x, y and z components of the magnetic field. These files are in Cricket Graph format with the first four lines not used. These are available for comments. The data is in units of 10^{-8}T. The files are named by the basename with the extensions .x, .y and .z. The format of these files is

```
*<CR>
 <CR>
 <CR>
 <CR>
 a <tab> b <tab> .............z <CR>
 a' <tab> b' <tab> ..............z' <CR>
 .
 .
 .
 A <tab> B <tab> ............... Z <CR>
```

where the array $\begin{bmatrix} a & b & ----- & z \\ a' & b' & ----- & z' \\ - & - & ------ & - \\ A & B & ----- & Z \end{bmatrix}$

describes one component of the field over a two dimensional plane.

Calculation parameters

The calculation parameters dialogue tells the COIL program where to calculate the field, and where to put the data. The data is stored in three field files which have a common basename and the extensions .x, .y and .z. The data is stored in Cricket Graph data format, and the first direction vector is in the columns direction, with the second direction vector in the rows direction. If you choose that the number of steps in a direction is 1, then no direction vector is necessary.

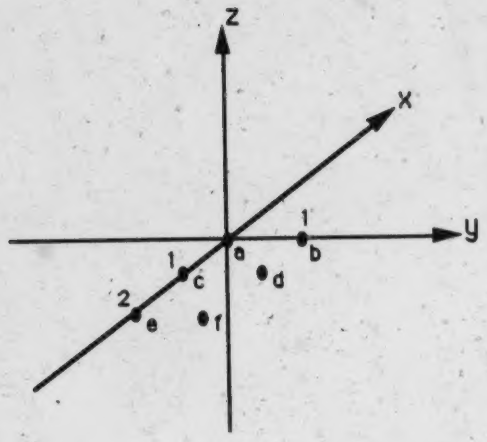

example

basefilename=data
basepoint=0 0 0
steps in first direction=2
direction vector1=0 1 0
steps in second direction=3
direction vector2=1 0 0

data.x	data.y	data.z
$B_{xa}B_{xb}$	$B_{ya}B_{yb}$	$B_{za}B_{zb}$
$B_{xc}B_{xd}$	$B_{yc}B_{yd}$	$B_{zc}B_{zd}$
$B_{xe}B_{xf}$	$B_{ye}B_{yf}$	$B_{ze}B_{zf}$

Once you have selected the parameters the program draws the plane that you have chosen on the coil drawing. You can modify the parameters any number of times before you calculate.

Appendix B

Correction of Spectra

Correcting the signal received by an inhomogeneous surface coil

The tip angle experienced by a spin on resonance and in the magnetic field in front of a surface coil varies with the position of the spin, since the field of a surface coil is very inhomogeneous. It is this tip angle variation which causes the banding seen on images in which the transmitter is a surface coil. Where the RF pulse transforms the magnetization completely into the xy plane, the signal is most intense, as the receiver is sensitive only to that part of the magnetization in the xy plane. In the regions where the RF pulse transforms the magnetization incompletely into the xy plane, the received signal intensity is below maximum, and where the magnetization has no component in the xy plane, the received signal intensity is zero.

Since the spin is originally in the z direction due to the B_0 field of the magnet, a rotation of $\pi/2$ radians would bring the spin into the xy plane, which is orthogonal to z. A rotation of $3\pi/2$, $5\pi/2$ etc would have the same effect, so a maximum signal is observed when the spin rotation is $(2n+1)\pi/2$ radians. If the rotation is π, 2π,3π etc there is no xy plane component, and so an $n\pi$ rotation gives a minimum signal.

The tip angle is varying continuously in the region in front of the surface coil, and so a volume will experience a range of tip angles. Since the signal is proportional to the sine of the tip angle (which has a maximum at $(2n+1)\pi/2$ and a minimum at $n\pi$ as required above) the received signal is given by

$$I \; \alpha \int_V \frac{2\beta}{\pi} \sin\beta \, S \, dV \qquad \text{(B - 1)}$$

where β is the tip angle bounded by the maximum tip angle producable by the coil in the volume, S is the spin density, and V is the volume measured.

Assuming that the spin density is constant over the volume of interest (VOI), the above equation can be simplified to

$$I \; \alpha \; S \int_V \beta \sin\beta \, dV \qquad \text{(B - 2)}$$

This is for the case of a simple experiment in which the signal is acquired directly after the RF pulse. In a spin echo experiment in which a second pulse refocusses the spin, equation (B - 2) is modified to

$$I \; \alpha \; S \int_V \beta \sin^3\beta \, dV \qquad \text{(B - 3)}$$

When depth pulses [Bendall, 1984] are used to remove the signal from some bands from the region near the surface coil, equation (B - 3) becomes

$$I \; \alpha \; S \int_V \beta \cos\beta/3 \, \cos\beta/5 \, \sin^3\beta \, dV \qquad \text{(B - 4)}$$

for the case of a sequence with two depth pulses, $\beta/3$ and $\beta/5$.

Since we are trying to find S in the above equations, the received signal I can be corrected by

$$S \alpha \frac{I}{\int_V \beta \cos(\beta/3) \cos(\beta/5) \sin^3\beta \, dV} \quad . \qquad (B-5)$$

Calculation of the Correction Factors

The correction factor to be applied to a spectrum acquired from a volume was calculated as follows. The magnetic field was calculated for a single plane perpendicular to the plane of the coil using the COIL program. These data were stored and used to find the field at any point within one diameter of the centre of the coil, using the symmetry of the coil (see Figure AppB.1). The algorithm used to convert the discrete data set into the field (B_x,B_y,B_z) at some point (x,y,z) was:

```
xx=|x|; yy=|y|; zz=|z|
if z=0 then $\theta=0$
if x=0 then $\theta=\pi/2$
$\theta=\tan^{-1}(z/x)$
i=round(samples_in_1_radius*yy/a)+1
j=round(30*$\sqrt{xx^2+zz^2}$)+1
$B_x$=I*radial_data[j,i]*cos($\theta$)
$B_y$=I*axial_data[j,i]*cos($\theta$)
$B_z$=0
if x<0 then $B_x$=-1*$B_x$
B=($B_x$,$B_y$,$B_z$)
```

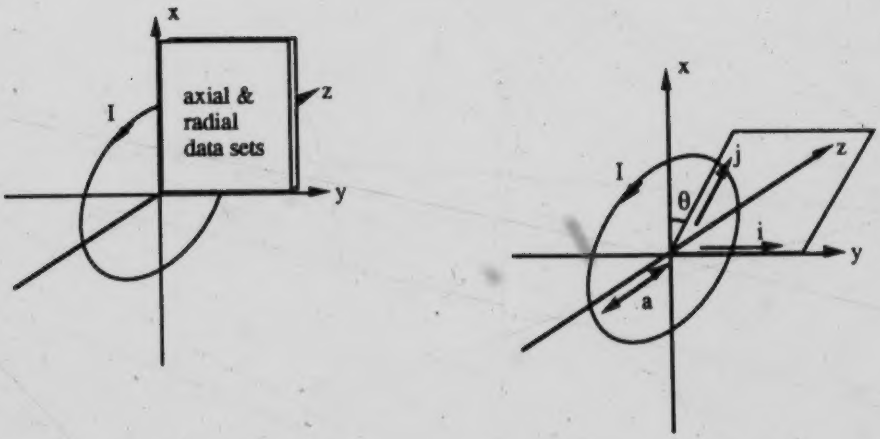

Figure AppB.1 The field data was calculated for the xy plane (a), and this data was used to find the field in an arbitrary plane through the origin (b) using the algorithm above.

Numerical integration required by equation (B - 5) above was performed using the Newton-Cotes formulae, of which Simpson's 3/8 rule is a particular case for the integration of a function given 4 points [Abramowicz and Stegun, 1965, p886].

These formulae have the general form: $\int_{x_0}^{x_N} f(x)\,dx \approx kh \sum_{n=0}^{N} a_n f(x_n)$

where h is the interval between x_i and x_{i+1}, and k, a_n are constants [Abramowicz and Stegun, 1965, p886].

Example Numerical integration of $\int_0^{\pi} \sin^2 x\,dx = \pi/2$

number of samples	result	%error
4	1.767	12.5
5	1.536	2.2
6	1.552	1.2
7	1.573	0.1
8	1.572	0.07
9	1.571	0.005
10	1.571	0.003

This technique can be extended to three dimensions, by applying the summation and weighting factors to each dimension in turn [Abramowicz and Stegun, 1965 p892].

$$\int_V f(x,y,z)\,dV \approx kh \sum_{i=0}^{N} a_i \sum_{j=0}^{N} a_j \sum_{k=0}^{N} a_k\, f(x_i,y_j,z_k)$$

$$= kh \sum_i \sum_j \sum_k a_{ijk}\, f(x_i,y_j,z_k) \qquad \text{where } a_{ijk} = a_i a_j a_k$$

Calculation of the 90 degree tip angle position.

When this technique of spectrum correction is used, it is very important to set the 90° tip angle at the correct place relative to the coil. The simplest way to do this is using a column profile perpendicular to the coil, but this does not give the true position. This section describes how to find the true position.

The tip angle at some position where the field is B_{xy} is given by

$$\theta = \frac{\pi}{2}\frac{B_{xy}}{B_{90xy}}$$, where B_{90xy} is the field that gives a 90° tip angle.

The components of the signal in the rotating frame can be found from simple geometry (see Figure AppB.2)

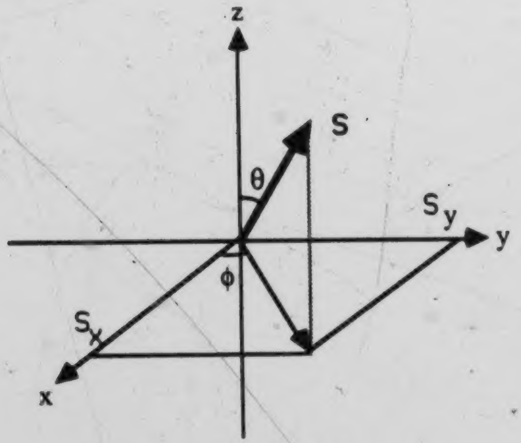

Figure AppB.2 Geometry for signal component evaluation.

The transverse magnetization components from a unit spin density sample at the field point of tip angle θ are given by:

$$S_x = \cos(\phi)\,\sin\left(\frac{\pi\,B_{xy}}{2B_{90xy}}\right)$$

$$S_y = \sin(\phi)\,\sin\left(\frac{\pi\,B_{xy}}{2B_{90xy}}\right) \text{ where } \phi = \tan^{-1}\left(\frac{S_y}{S_x}\right)$$

The induced signal in the receiver is therefore weighted by the coil sensitivity and is given by:

$$R_x = \frac{B_{xy}}{B_{90xy}}\cos(\phi)\sin\left(\frac{\pi\,B_{xy}}{2B_{90xy}}\right)$$

$$R_y = \frac{B_{xy}}{B_{90xy}}\sin(\phi)\,\sin\left(\frac{\pi\,B_{xy}}{2B_{90xy}}\right)$$

When a 2D profile is used to position the 90° tip angle in a spectroscopy experiment, a problem arises in that the position of the maximum of the 90° band does not coincide with the position of the true 90° tip angle in the sample. This arises since the surface coil reception drops off with distance, and this distorts the 90° band, bringing the maximum closer to the coil. It should be noted that the position of 180° tip angle where the received signal is zero is not affected by surface coil receiver variation, so this position should be used where possible, and then the pulse length halved to give a 90° pulse (see Figure AppB.3).

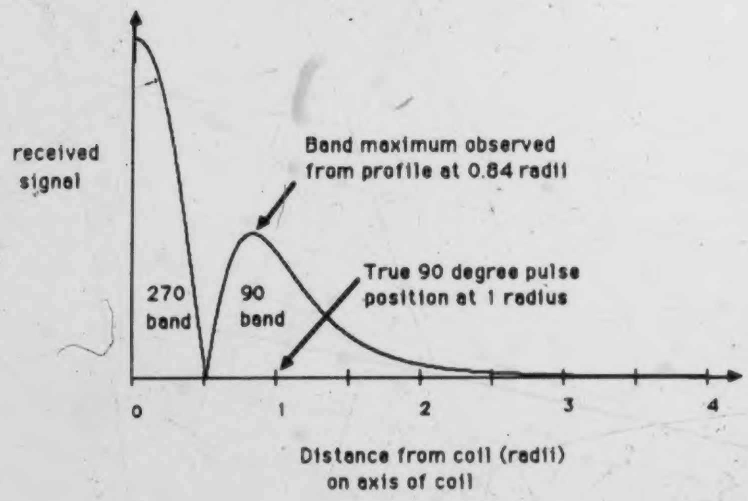

Figure AppB.3 Demonstrating the discrepancy between the profile band maximum and the true 90° tip angle position.

The position of the profile band maximum and its relationship to the true tip angle can be calculated for a circular coil as below, where the pulse sequence is assumed to be a simple 90-acquire sequence.

$$\text{Received signal, } S = \frac{1}{B_{90}} \frac{\mu_0}{2} \frac{a^2}{(y^2+a^2)^{3/2}} \sin \frac{\mu_0}{2} \frac{a^2}{(y^2+a^2)^{3/2}} \frac{\pi}{2B_{90}} \qquad \text{(B - 6)}$$

where B_{90} is the field required to give a 90° tip angle,
a is the radius of the coil,
y is the distance along the coil axis

To find the position in y of the maximum, differentiate (B - 6) with respect to y, and set the result to zero.

$$\frac{dS}{dy} = -\frac{\mu_0}{2B_{90}}\frac{3/2\,a^2\,2y}{(y^2+a^2)^{5/2}}\sin\left(\frac{\mu_0}{2}\frac{a^2}{(y^2+a^2)^{3/2}}\frac{\pi}{2B_{90}}\right)$$
$$-\frac{\mu_0}{2B_{90}}\frac{a^2}{(y^2+a^2)^{3/2}}\cdot\frac{3\mu_0\cdot y}{2}\cdot\frac{a^2}{(y^2+a^2)^{5/2}}\cdot\frac{\pi}{2B_{90}}\cos\left(\frac{\mu_0}{2}\frac{a^2}{(y^2+a^2)^{3/2}}\frac{\pi}{2B_{90}}\right) = 0$$

$$\therefore \sin\left(\frac{\mu_0}{2}\frac{a^2}{(y^2+a^2)^{3/2}}\frac{\pi}{2B_{90}}\right) = -\frac{a^2}{(y^2+a^2)^{3/2}}\cdot\frac{\pi\mu_0}{4B_{90}}\cos\left(\frac{\mu_0}{2}\frac{a^2}{(y^2+a^2)^{3/2}}\frac{\pi}{2B_{90}}\right)$$

$$\therefore \tan\left(\frac{\mu_0}{2}\frac{a^2}{(y^2+a^2)^{3/2}}\frac{\pi}{2B_{90}}\right) = -\frac{a^2}{(y^2+a^2)^{3/2}}\cdot\frac{\pi\mu_0}{4B_{90}} \qquad \text{(B - 7)}$$

now the first solution of tan x = -x is x = 2.03 and this corresponds to 90° maximum, so

$$\frac{a^2}{(y^2+a^2)^{3/2}}\cdot\frac{\pi\mu_0}{4B_{90}} = 2.03. \qquad \text{(B - 8)}$$

Now if we define y_{90} as the depth at which the field is B_{90}, we know that

$$B_{90} = \frac{\mu_0}{2}\frac{a^2}{(y_{90}^2+a^2)^{3/2}} \qquad \text{(B - 9)}$$

Substituting equation (B - 9) in equation (B - 8) gives $\left[\dfrac{\left(\frac{y_{90}}{a}\right)^2+1}{\left(\frac{y}{a}\right)^2+1}\right]^{3/2} = 2.03$

which reduces to

$$(y/a)^2 = \frac{(y_{90}/a)^2 - 0.19}{1.19} \quad . \qquad \text{(B - 10)}$$

This gives real solutions for $y_{90}/a > 0.44$ which is the depth at which the peak on the 90° band first appears. Figure AppB.4 shows the function of equation (B - 10).

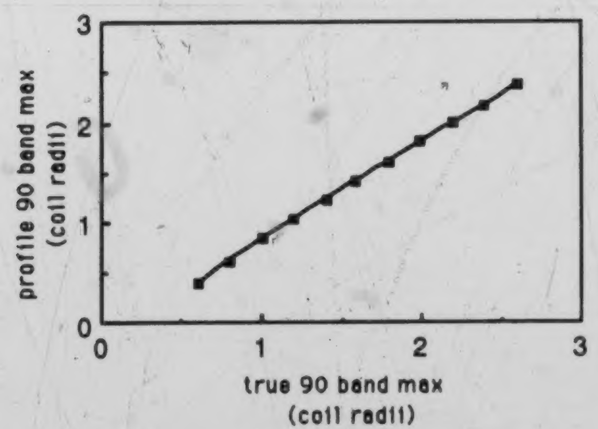

Figure AppB.4 The relationship between the peak of the 90° band observed from a profile and the true position of the 90° tip angle.

The Correction Factors Program

The purpose of Correction Factors is to calculate the correction factor which needs to be applied to a spectrum from a volume to be able to compare it directly to a spectrum obtained from another volume elsewhere in the field from a surface coil. It can be used with any type of coil, once the field has been calculated using the COIL program. It needs to have the B_x and B_y components of the field available in separate files and in the Cricket graph format. (see the formats for the COIL program field data files in Appendix A).

The procedure readfile is called to translate the field data from the text file format and place it into two arrays dat1 and dat2. It uses the function convert to change a number in string format into an integer. Note that readfile ignores the first four lines of the data files.

Once the data is present in memory a dialogue begins with the user to determine the parameters of the calculation. These include the position and size of the volume and the field required for a 90° tip angle (e.g. 22.2×10^{-8}T for 1 radius from 1m radius surface coil). The program then splits up the volume given into further sub-volumes whose separation corresponds to the separation of data points in the data file, so that the integration can be performed. For each subvolume in turn B_{xy} and thus the tip angle is calculated, given the pulse sequence specified. These tip angles are then combined using the Newton-Cotes method for numerical integration in three dimensions (see Calculation of Correction Factors in this Appendix).

The correction factor obtained is used to convert the volume spectral data to the level it would be if it had no field variation across it. Further, simple, correction would be needed for comparing different volumes. The operation of the Correction Factor program is shown diagrammatically in Figure AppB.5.

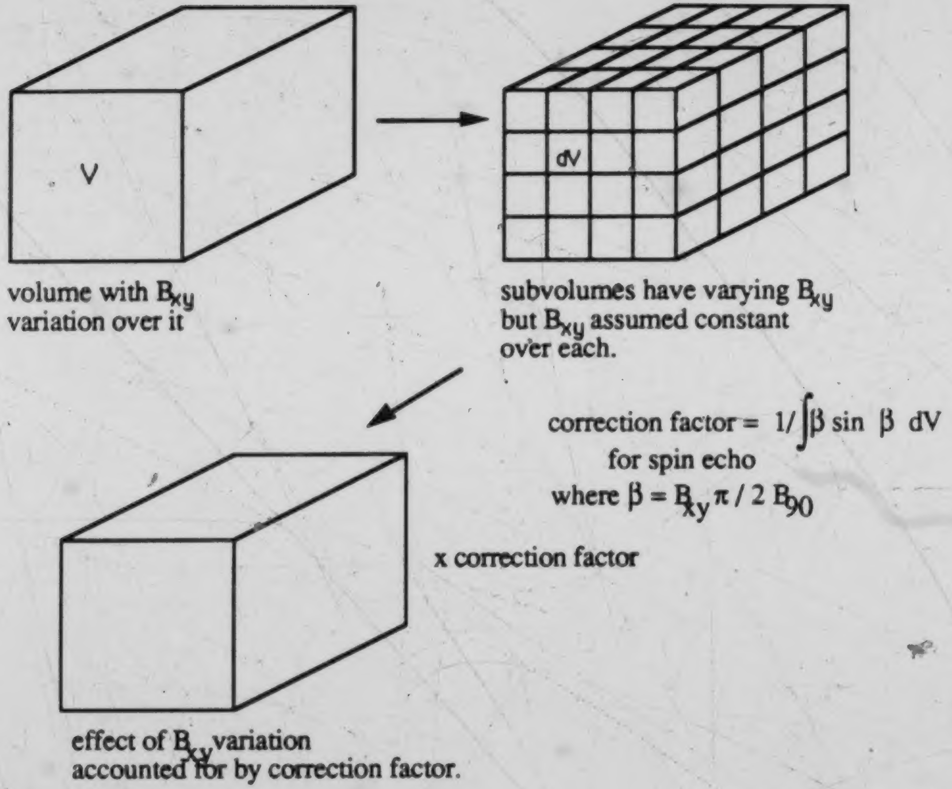
V
dV
volume with B_{xy}
variation over it
subvolumes have varying B_{xy}
but B_{xy} assumed constant
over each.
correction factor = $1/\int \beta \sin \beta \, dV$
for spin echo
where $\beta = B_{xy} \pi / 2 B_{90}$
x correction factor
effect of B_{xy} variation
accounted for by correction factor.

Figure App.B.5 The use of the Correction Factor program

```
program correction_factors;
{ Calculates the correction to be applied to a spectrum }

uses memtypes,quickdraw,sane;

 const
  diskname='gradients';
  directory='field data';            {directory containing field data}
  radstep = 60;                      {number of data points in the radial direction}
  axstep =60;                        {number of data points in the axial direction}
  samples_in_1_radius=30;
  current=1;
  theta_by_3_depth=true;              {depth pulses on?}
  theta_by_5_depth=true;
  spin_echo=true;                    {spin echo experiment? default is 90 acquire}

 type
  dataarray = array[1..60, 1..60] of integer;
  str10 = string[10];
  str20 = string[20];
  longstring=string[60];

 var
  an:array[4..10,0..9] of real;                                 {newton cotes factors}
  kf:array[4..10] of real;           {constant factors  sum=kf[n] sigma an[n,m] x[m]}
  axialdata,radialdata:string[60];                             {names of the datafiles}
  dat1, dat2 : dataarray;                                     {arays for the field data}
  xsteps,ysteps,zsteps:integer;           {number of steps to sum in the 3 dimensions}
  xint,yint,zint:extended;                       {sampling interval in 3 dimensions}
  xex,yex,zex:extended;                        {extents of the volume in 3 dimensions}
  counter,i,j,k:integer;                                   {miscellaneous counters}
  a:extended;                                          {the radius of the surface coil}
  x,y,z:extended;                                   {coordinates of centre of volume}
  xbase,ybase,zbase:extended;                       {coordinates of corner of volume}
  b90:extended;                           {field which gives 90 pulse units 10E-9 T}
  correction_factor:extended;


 procedure readfile (var whicharray : dataarray;
       filename : longstring);
 var
  row, col : integer;
  f : text;
  line : string[255];

 procedure getaline;

  var
   thisstring:str20;
   thischar:char;
```

```
function convert(str:str10):integer;

var
   value,sign:extended;
   leftofpoint,numbers,len,counter:integer;
   pointflag:boolean;

begin
   len:=length(str);
   numbers:=0;
   leftofpoint:=0;
   value:=0;
   sign:=1;
   pointflag:=false;
   for counter:=1 to len do
   begin
      if (ord(str[counter])>47) and (ord(str[counter])<58) then
      begin
         value:=value+(ord(str[counter])-48)/xpwri(10,numbers+1);
         numbers:=numbers+1
      end
      else
      begin
       if (str[counter]='.') then
      begin
         leftofpoint:=numbers;
         pointflag:=true;
      end;
       if (str[counter]='+') then sign:=1;
       if (str[counter]='-') then sign:=-1
      end;
   end;
   if pointflag=false then leftofpoint:=numbers;
   convert:=round(10*value*xpwri(10,leftofpoint)*sign);
end;

 begin
  col:=1;
  thischar:=chr(0);
  while not(thischar=chr(13)) do
  begin
     thischar:=chr(0);
      thisstring:='';
     while ((not(thischar=chr(9))) and (not(thischar=chr(13)))) do
     begin
        read(f,thischar);
        thisstring:=thisstring+thischar
     end;
     whicharray[col,row]:=convert(thisstring);
     col:=col+1
  end;
```

```
end;

begin
 reset(f, filename);
 readln(f, line);{first 4 lines are blank}
 readln(f, line);
 readln(f, line);
 readln(f,line);
 readln(f, line);
 row := 1;
 while (eof(f) = false) do
  begin
   getaline;
   row := row + 1;
  end;
 close(f);
end;

procedure make_arrays_of_newton_cotes_factors;

var
   i,j:integer;

begin
   for i:=4 to 10 do
     for j:=0 to 9 do an[i,j]:=0;
   an[4,0]:=1; an[4,1]:=3;  an[4,2]:=3; an[4,3]:=1;
   an[5,0]:=7; an[5,1]:=32; an[5,2]:=12;an[5,3]:=32; an[5,4]:=7;
   an[6,0]:=19;an[6,1]:=75; an[6,2]:=50;an[6,3]:=50; an[6,4]:=75;
   an[6,5]:=19;
   an[7,0]:=41;an[7,1]:=216;an[7,2]:=27;an[7,3]:=272;an[7,4]:=27;
   an[7,5]:=216;an[7,6]:=41;
   an[8,0]:=751;an[8,1]:=3577;an[8,2]:=1323;an[8,3]:=2989;
   an[8,4]:=2989;an[8,5]:=1323;an[8,6]:=3577;an[8,7]:=751;
   an[9,0]:=989;an[9,1]:=5888;an[9,2]:=-928;an[9,3]:=10496;
   an[9,4]:=-4540;an[9,5]:=10496;an[9,6]:=-928;an[9,7]:=5888;
   an[9,8]:=989;
   an[10,0]:=2857;an[10,1]:=15741;an[10,2]:=1080;an[10,3]:=19344;
   an[10,4]:=5778;
   an[10,9]:=2857;an[10,8]:=15741;an[10,7]:=1080;an[10,6]:=19344;
   an[10,5]:=5778;
   kf[4]:=8;kf[5]:=90;kf[6]:=288;kf[7]:=840;kf[8]:=17280;
   kf[9]:=28350;kf[10]:=89600;

end;

function
correction(x,y,z,a:extended;xsteps,ysteps,zsteps:integer;b90:extended):extended;

var
   i,j,k:integer;
   total:extended;
   dummytip:extended;

function tip_angle_factor(x,y,z,a,b90:extended):extended;

var
   tip_angle:extended;
   Bx,By,Bz:extended;
   bxy:extended;
   dummytip:extended;

procedure calculate_xyz_components_of_field(x,y,z,a:extended);

 var
   xx,yy,zz:extended;
   i,j:integer;
   theta:extended;

 begin
   xx:=abs(x);
   yy:=abs(y);
   zz:=abs(z);
   if z=0 then theta:=0 else
   if x=0 then theta:=3.1416/2 else
   theta:=arctan(z/x);
   i:=round(30*yy/a)+1;
   j:=round(30*sqrt(sqr(xx)+sqr(zz))/a)+1;
   Bx:=current*dat2[j,i]*cos(theta);
   By:=current*dat1[j,i];
   Bz:=0;
   if x<0 then Bx:=-1*Bx;
   if z<0 then Bz:=-1*Bz
  end;

begin
   calculate_xyz_components_of_field(x,y,z,a);
   bxy:=100*sqrt(sqr(By/100)+sqr(Bx/100));
   tip_angle:=(bxy*(pi/2)/(10*b90));
   dummytip:=abs(sin(tip_angle)*bxy/(10*b90));
   if theta_by_3_depth then
      dummytip:=dummytip*cos(tip_angle/3);
   if theta_by_5_depth then
      dummytip:=dummytip*cos(tip_angle/5);
   if spin_echo then
      dummytip:=dummytip*sqr(sin(tip_angle));
   tip_angle_factor:=dummytip;
end;

begin
 total:=0;
     for i:=0 to xsteps-1 do
```

```
      for j:=0 to ysteps-1 do
      for k:=0 to zsteps-1 do
      begin
        dummytip:=tip_angle_factor(xbase+i*xint,
                          ybase+j*yint,
                          zbase+k*zint,
                          a,
                          b90);
        total:=total+an[xsteps,i]
                *an[ysteps,j]
                *an[zsteps,k]
                *dummytip;
        writeln(xbase+i*xint,' ',
              ybase+j*yint,' ',
              zbase+k*zint,' ',
              dummytip,' ',
             total);
      end;
      total:=(total/(kf[xsteps]*kf[ysteps]*kf[zsteps]));
      correction:=1/total;
end;

begin
 writeln('axial data');
 readln(axialdata);
 writeln('radial data');
 readln(radialdata);
 axialdata:=diskname+':'+directory+':'+axialdata;
 radialdata:=diskname+':'+directory+':'+radialdata;
 readfile(dat1, axialdata);
 writeln('read the first file');
 readfile(dat2, radialdata);
 writeln('read the second file');
 a:=999;
 make_arrays_of_newton_cotes_factors;
 xint:=1/samples_in_1_radius;
 yint:=1/samples_in_1_radius;
 zint:=1/samples_in_1_radius;
 if spin_echo then writeln('spin echo experiment')
   else writeln('90 acquire experiment');
 if theta_by_3_depth then writeln('theta/3 depth pulse');
 if theta_by_5_depth then writeln('theta/5 depth pulse');
 while not(a=0) do
 begin
    writeln('radius of coil =');
    readln(a);
    if a>0 then
    begin
      writeln('coords of base point (x<cr>y<cr>z<cr>)');
      readln(x,y,z);
      writeln('size of volume (in x<cr>in y<cr>in z<cr>)');
    readln(xex,yex,zex);
     writeln('b90');
    readln(b90);
    xsteps:=round(xex/(xint*a));
    ysteps:=round(yex/(yint*a));{      find no of steps           }
    zsteps:=round(zex/(zint*a));
      writeln('steps in x,y,z = ',xsteps,' ',ysteps,' ',zsteps);
    xbase:=x-xex/2;
    ybase:=y-yex/2;        {      find corner of volume       }
    zbase:=z-zex/2;
      writeln('corner of volume is ',xbase,' ',ybase,' ',zbase);
    correction_factor:=correction(x,y,z,a,xsteps,ysteps,zsteps,b90);
    writeln('correction factor required is ',correction_factor);
  end;
end;
readln
end.
```

Appendix C

16 bit to 8 bit image conversion with contrast enhancement

```
{this programme is used to convert 16 bit images which have
 been transferred from the Vax to the Mac into 8 bit images,
 scaling the gray levels of the image into the range 0 - 255

 written by Ian Thomas in TurboPascal in june 1989}


program convert_16_to_8_bit;

const
   noofimages=1;
{this is the number of images strung together
              in the input text file}


var
   infile,outfile:text;
   thischar1,thischar2:char;
   data:real;
   i,j,counter:integer;
   max,min:real;
   inputfilename,outputfilename:string[60];

 function trim(x:real):real;

 begin
   if (x>256) then trim:=256;
   if (x<0) then trim:=0
 end;

 begin
   writeln('enter the name of the input file');
   readln(inputfilename);
   writeln('enter the name of the output file');
   readln(outputfilename);
   reset(infile,inputfilename);
   writeln('opened ',inputfilename);
 {
        This part finds the maximum and minimum of first image
 }
   counter:=0;
   max:=0;
   min:=1000000;
   writeln('cleared maxmin');
```

```
  begin
    for i:=1 to 256 do
    begin
      writeln(i);
      for j:=1 to 256 do
      begin
        read(infile,thischar1);
        read(infile,thischar2);
        data:=ord(thischar2)*256+ord(thischar1);
        if (data>max) then max:=data;
        if (data<min) then min:=data;
      end;
    end;
  end;
  close(infile);
{
      Now convert from 16 bit to 8 bit
}
  reset(infile,inputfilename);
  writeln('reset the input file');
  counter:=0;
  while (not(eof) and (counter<noofimages)) do
  begin
    rewrite(outfile,outputfilename);
{
      This header assumes 256x256 images
}
    write(outfile,#255);
    write(outfile,#0);
    write(outfile,#255);
    write(outfile,#0);

    for i:=1 to 256 do
    begin
      for j:=1 to 256 do
      begin
        read(infile,thischar1);
        read(infile,thischar2);
        data:=ord(thischar2)*256+ord(thischar1);
        write(outfile,chr(trunc(data/256)));
      end;
       writeln('file ',counter,'line ',i);
    end;
    counter:=counter+1;
    close(outfile);
  end;
  close(infile);
end.
```

Appendix D

Image correction programs

Sensitivity Maps

This program is used to combine two field data files (B_x and B_y) into coil sensitivity maps. There are three possible outputs. Using the procedure contour a contour map can be produced, as shown in Figure 6.2.4. The value of the variable x which is passed to the procedure contour is the level at which the contour line is to be drawn, so a contour map requires several calls to this procedure. This contour map is drawn on the screen of the Mac. It can then be copied to a file, or printed. The second possible output is a simple grayscale image produced on the screen of the Mac using the procedure gray. The parameter for this procedure defines the level above which all is black. The third output is a text file sensitivity map which can be printed using an image processing package, and is also an input for the image correction program. Figure 8.4.2 shows sensitivity maps produced using this program. The output file is named 'correction file'.

Image Correction

This program accepts a correction file from the sensitivity maps program, and multiplies it onto a region of a given image, as shown in Figures 8.4.3 and 8.4.4. Figure AppD.1 shows the parameters used to align the correction array onto the image. A simple gray scale image of the correction file is plotted, and then the input image in corrected form is plotted. The output corrected image is placed in a file named 'corrected image'.

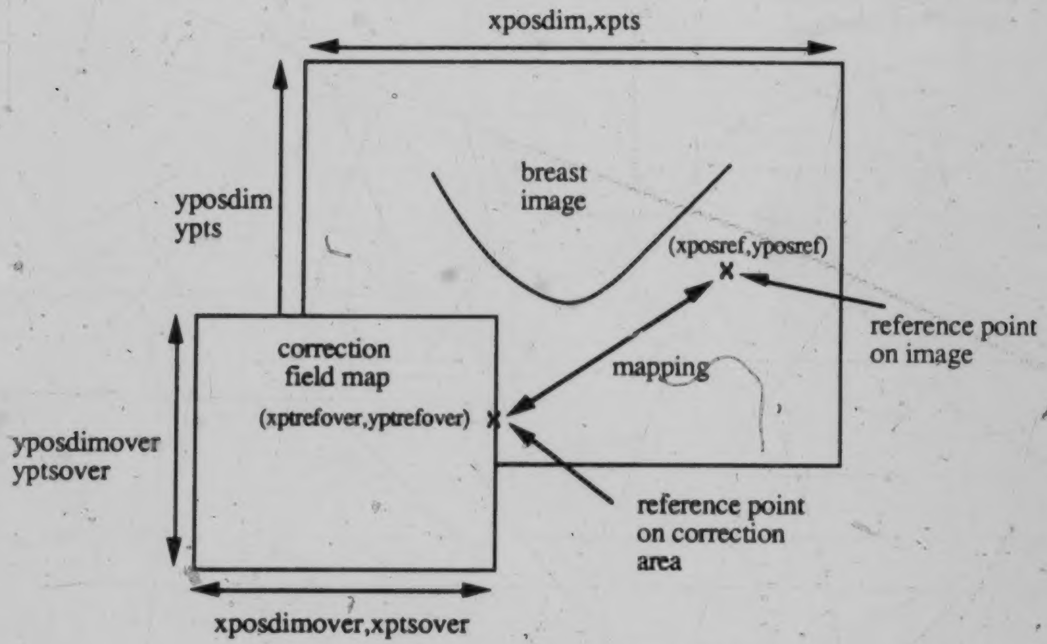
xposdim,xpts
yposdim
ypts
breast
image
(xposref,yposref)
reference point
on image
correction
field map
mapping
(xptrefover,yptrefover)
yposdimover
yptsover
reference point
on correction
area
xposdimover,xptsover

Figure AppD.1 Parameters used in the Image Correction program.

```
program sensitivity_maps;
{ produces sensitivity maps from field files }
{ both gray scale and contour line maps available }
{ written in turbo pascal fo the Macintosh }

uses memtypes,quickdraw;

 const
  diskname='coil';
  directory='field_data';                              {directory for the field data files}
  xstart = 200; ystart = 320;                       {position of image on Mac screen}
  xstep = 3; ystep = 3;                                        {points per pixel on screen}
  radstep =41; axstep =41;                {number of data points in two dimensions}
  reflect=false;                                                  {reflect the image or not}

 type
  dataarray = array[1..60, 1..60] of integer;
  str10 = string[10];
  str20 = string[20];
  ptarray = array[1..5] of record
    x : integer;
    y : integer
   end;
  longstring=string[60];

 var
  b90:real;                                                                    {b90 field (x10-8T)}
  f:text;
  axialdata,radialdata:string[60];
  axfile,rafile:str20;
  pt : ptarray;
  dat, dat1, dat2 : dataarray;
  counter, i, j,k, pn,loop : integer;
  a, b, c, d, x, r, theta,dummy1,dummy2,dummy3 : real;
  tip_angle:real;
  mypicture:grafport;

procedure contour (x : real);
{  draws a contour line at the level x on the screen  }

 var
  i, j : integer;
begin
 for i := 1 to radstep - 1 do
  begin
   for j := 1 to axstep - 1 do
    begin
     c := dat[i, j]; d := dat[i + 1, j]; a := dat[i, j + 1]; b := dat[i + 1, j + 1];
     pn := 0;
     if (x >= a) and (x < c) then
      begin
```

```
          pn := pn + 1; pt[pn].x := xstart + (i - 1) * xstep;
          pt[pn].y := ystart - (j) * ystep + trunc(ystep * (x - a) / (c - a))
         end;
        if (x < a) and (x >= c) then
         begin
          pn := pn + 1; pt[pn].x := xstart + (i - 1) * xstep;
          pt[pn].y := ystart - (j - 1) * ystep - trunc(ystep * (x - c) / (a - c));
         end;
        if (x >= a) and (x < b) then
         begin
          pn := pn + 1; pt[pn].x := xstart + (i - 1) * xstep + trunc(xstep * (x - a) / (b - a));
          pt[pn].y := ystart - j * ystep;
         end;
        if (x < a) and (x >= b) then
         begin
          pn := pn + 1; pt[pn].x := xstart + (i) * xstep - trunc(xstep * (x - b) / (a - b));
          pt[pn].y := ystart - j * ystep;
         end;
        if (x >= b) and (x < d) then
         begin
          pn := pn + 1; pt[pn].x := xstart + (i) * xstep;
          pt[pn].y := ystart - j * ystep + trunc(ystep * (x - b) / (d - b));
         end;
        if (x < b) and (x >= d) then
         begin
          pn := pn + 1; pt[pn].x := xstart + (i) * xstep;
          pt[pn].y := ystart - (j - 1) * ystep - trunc(ystep * (x - d) / (b - d));
         end;
        if (x >= c) and (x < d) then
         begin
          pn := pn + 1; pt[pn].x := xstart + (i - 1) * xstep + trunc(xstep * (x - c) / (d - c));
          pt[pn].y := ystart - (j - 1) * ystep;
         end;
        if (x < c) and (x >= d) then
         begin
          pn := pn + 1; pt[pn].x := xstart + (i) * xstep - trunc(xstep * (x - d) / (c - d));
          pt[pn].y := ystart - (j - 1) * ystep;
         end;
        if (pn > 1) then
         begin
            moveto(pt[1].x, pt[1].y);  lineto(pt[2].x, pt[2].y);
          if reflect=true then
          begin
            moveto(2 * xstart - pt[1].x, pt[1].y); lineto(2 * xstart - pt[2].x, pt[2].y)
          end;
         end;
       end;
     end;
   end;
```

```
procedure gray(x:real);
{ plots a gray scale image on the screen }

 var
  i, j : integer;
  ave:real;
  little:rect;
 begin
  for i := 1 to radstep - 1 do
   begin
    for j := 1 to axstep - 1 do
     begin
        c := dat[i, j]; d := dat[i + 1, j]; a := dat[i, j + 1]; b := dat[i + 1, j + 1];
        ave:=(a+b+c+d)/4;
        setrect(little, xstart+ (i - 1) * xstep
                 ,ystart - j * ystep,xstart+i*xstep,ystart-(j-1)*ystep);
        penpat(white);
        if ave>x/4 then penpat(ltgray);
        if ave>x/2 then penpat(dkgray);
        if ave>3*x/4 then penpat(black);
        paintrect(little);
        if reflect=true then
        begin
          setrect(little, xstart - (i ) * xstep,ystart - j * ystep
                   ,xstart-(i-1)*xstep,ystart-(j-1)*ystep);
          paintrect(little);
        end;
      end;
    end;
 end;

function convert(str:str10):integer;
{ converts a number in string form into an integer }

var
    value,sign:real;
    leftofpoint,numbers,len,counter:integer;
    pointflag:boolean;

function power10(i:integer):real;

begin
    if (i=0) then power10:=1
    else power10:=10*power10(i-1)
end;

begin
    len:=length(str);
    numbers:=0; leftofpoint:=0; value:=0; sign:=1;
    pointflag:=false;
  for counter:=1 to len do
  begin
     if (ord(str[counter])>47) and (ord(str[counter])<58) then
     begin
        value:=value+(ord(str[counter])-48)/power10(numbers+1);
        numbers:=numbers+1
     end
     else
     begin
      if (str[counter]='.') then
     begin
        leftofpoint:=numbers; pointflag:=true;
     end;
      if (str[counter]='+') then sign:=1;
      if (str[counter]='-') then sign:=-1
     end;
   end;
   if pointflag=false then leftofpoint:=numbers;
   convert:=round(10*value*power10(leftofpoint)*sign);
end;

 procedure readfile (var whicharray : dataarray;
       filename : longstring);
{ reads a data file into an array }

  var
   row, col : integer;
   f : text;
   line : string[255];

 procedure getaline;

  var
    thisstring:str20;
    thischar:char;

  begin
    col:=1; thischar:=chr(0);
    while not(thischar=chr(13)) do
    begin
       thischar:=chr(0); thisstring:='';
       while ((not(thischar=chr(9))) and (not(thischar=chr(13)))) do
       begin
          read(f,thischar); thisstring:=thisstring+thischar
       end;
       whicharray[col,row]:=convert(thisstring); col:=col+1
    end;
  end;

 begin
  reset(f, filename); row := 1;
 while (eof(f) = false) do
  begin
   getaline;  row := row + 1;
  end;
 close(f);
end;

begin
 initgraf(@theport);  openport(@mypicture);
 initport(@mypicture); setport(@mypicture);

{ get the programme parameters }
 writeln('axial data'); readln(axfile);
 writeln('radial data'); readln(rafile);
 writeln('b90'); readln(b90);

{ load the field data into arrays }
 axialdata:=diskname+':'+directory+':'+axfile;
 radialdata:=diskname+':'+directory+':'+rafile;
 readfile(dat1, axialdata); writeln('read the first file');
 readfile(dat2, radialdata); writeln('read the second file');

{ calculate the sensitivity, here for a spin echo }
 for i := 1 to radstep  do
  for j := 1 to axstep  do
   begin
     tip_angle:=sqrt(sqr(dat1[i,j]/10)+sqr(dat2[i,j]/10))*(3.14159/2)/(b90);
     dat[i,j]:=round(20*abs(sin(tip_angle)*sqr(sin(tip_angle))*tip_angle));
{ Note correction file scaled so b90 corresponds to 32  }
   end;
   writeln('transformed the data');

{ draw a frame around picture }
if reflect=true then
begin
 moveto(xstart - (radstep - 1) * xstep, ystart);
 lineto(xstart - (radstep - 1) * xstep, ystart - (axstep - 1) * ystep);
 lineto(xstart + (radstep - 1) * xstep, ystart - (axstep - 1) * ystep);
 lineto(xstart + (radstep - 1) * xstep, ystart);
 lineto(xstart - (radstep - 1) * xstep, ystart)
end
else
begin
  moveto(xstart , ystart);
 lineto(xstart , ystart - (axstep - 1) * ystep);
 lineto(xstart + (radstep - 1) * xstep, ystart - (axstep - 1) * ystep);
 lineto(xstart + (radstep - 1) * xstep, ystart);
 lineto(xstart , ystart)
end;

{ draw the picture }
```

```
gray(100);
penpat(black);
contour(20); contour(40); contour(60); contour(80); contour(100);

{ write the sensitivity map into a text file }
rewrite(f,'coil:correctionfile');
write(f,chr((radstep)-1),chr(0),chr((axstep)-1),chr(0));
for i:=1 to radstep do
begin
  for j:=axstep downto 1 do
  begin
    write(f,chr(dat[j,i]));
  end;
end;
close(f);
readln
end.
```

```
program image_correction;
{ applies a correction to region of an image }
{ written in turbo pascal for the Macintosh }

uses memtypes,quickdraw;

const
   xposdim=250.0; yposdim=250.0;              {size of image to be corrected (mm)}
   xpts=256;  ypts=256;                      {no. of points in image to be corrected}
   xposdimover=140.0;  yposdimover=140.0;      {size of correction overlay (mm)}
   xptsover=41; yptsover=41;                  {no. of points in correction overlay}
   xposref=199.0; yposref=103.0; {reference posn.on image to be corrected (mm)}
   xptrefover=41; yptrefover=18;            {reference point on correction overlay}
   maxcorrection=4;                                 { maximum correction to use }
   scalsdown=0.75;                            { scaling factor for corrected image}

var
   f,c,g:text;
   i,j,k,xpt,ypt,xc,yc,dummy:integer;
   xpos,ypos,dummyr:real;
   name:string[60];
   myport:grafport;
   ch:char;
   corr:array[1..41,1..41] of real;

begin
   initgraf(@theport); openport(@myport);
   setrect(myport.portrect,1,1,400,300); setport(@myport);
   penpat(white);
   paintrect(myport.portrect);
   reset(c,'coil:correctionfile');
   pensize(3,3);

   { draw a frame }
   moveto(259,49); lineto(381,49); lineto(381,171); lineto(259,171); lineto(259,59);

   { plot gray scale map of correction data }

   for k:=1 to 4 do read(c,ch);{skip header}
   for i:=1 to yptsover do for j:=1 to xptsover do
   begin
      penpat(white);
      read(c,ch); dummy:=ord(ch);
      if not(dummy=0) then
      begin
         corr[i,j]:=32/dummy;{correction file was scaled to b90 is 32 }
      end else corr[i,j]:=32;
      if corr[i,j]>maxcorrection then corr[i,j]:=maxcorrection;
      dummy:=trunc(corr[i,j]);
      penpat(white);
      if dummy>0.5 then penpat(ltgray); if dummy>1 then penpat(gray);
```

```
    if dummy>5 then penpat(dkgray);
    moveto(260+3*(j-1),50+3*(i-1)); line(0,0)
  end;
  close(c);
  moveto(20,20); drawstring('name of file'); readln(name);
  reset(f,name); rewrite(g,'correctedimage');

{transfer header}
  for k:=1 to 4 do
  begin
    read(f,ch); write(g,ch)
  end;

{ draw box around area to correct }
  pensize(1,1);
  penpat(black);
  moveto(trunc(xposref-xptrefover*xposdimover/xptsover)
         ,trunc(yposref-yptrefover*yposdimover/yptsover));
  lineto(trunc(xposref-xptrefover*xposdimover/xptsover)
         ,trunc(yposref+(yptsover-yptrefover)*yposdimover/yptsover));
  lineto(trunc(xposref+(xptsover-xptrefover)*xposdimover/xptsover)
         ,trunc(yposref+(yptsover-yptrefover)*yposdimover/yptsover));
  lineto(trunc(xposref+(xptsover-xptrefover)*xposdimover/xptsover)
         ,trunc(yposref-yptrefover*yposdimover/yptsover));
  lineto(trunc(xposref-xptrefover*xposdimover/xptsover)
         ,trunc(yposref-yptrefover*yposdimover/yptsover));

  { create corrected image }
  for i:=1 to ypts do
  for j:=1 to xpts do
  begin
    read(f,ch);
    dummy:=ord(ch);
     xpt:=j;ypt:=i;
    xpos:=xpt*xposdim/xpts; ypos:=ypt*yposdim/ypts;
    xc:=round(xptrefover+(xpos-xposref)*xptsover/xposdimover);
    yc:=round(yptrefover+(ypos-yposref)*yptsover/yposdimover);
    if ((xc>=1) and (xc<=41) and (yc<=41) and(yc>=1))
    then dummyr:=dummy*corr[yc,xc]else dummyr:=dummy;
    dummyr:=dummyr*scaledown; dummy:=0;
    if dummyr>255 then dummy:=255;
    if dummyr<1 then dummy:=1;
    if ((dummyr>=1) and (dummyr<=255)) then dummy:=round(dummyr);
    write(g,chr(dummy));
    penpat(white);
    if dummy>200 then penpat(black); if dummy>150 then penpat(dkgray);
    if dummy>100 then penpat(gray); if dummy>50 then penpat(ltgray);
    moveto(j,i); line(0,0)
  end;
  close(f); close(g);readln;
end.
```

Appendix E

Image transfer

Images from the Philips Gyroscan system are in the format

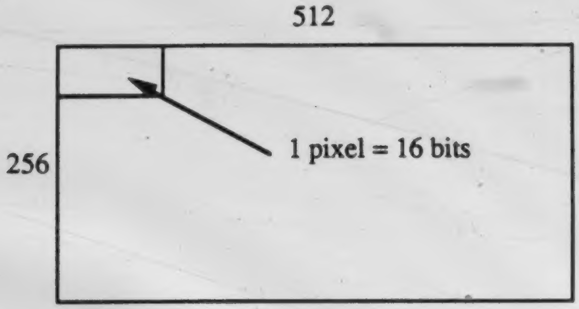

There are 256 records, each of 512 x 8 bits per image. When the file contains multiple images, these are strung together without a break, so that, for example, a file containing six images consists of 1526 records of 512 x 8 bits. The images were transferred from the VAX to the Macintosh microcomputer using the program Vax_to_Mac developed by Dr. Koles of Applied Sciences in Medicine. This program was used as it offers fast format-free transfer of data from the VAX to the Macintosh.

Once the data had been transferred, in a format-less state, it was prepared for printing using the package Image by two programs: Chop_into_Files and convert_16_to_8_bit (Appendix C) The first of these simply cuts the input file into blocks of 128 kbytes, which represent one image each, and the second puts a header onto the front of each file, converts each pixel into 8 bits, and scales the data so that the range of pixel values is 0 to 255. The images files are now in the correct format to be 'imported' into Image and printed on the laser writer.

The format in which the images end up is:

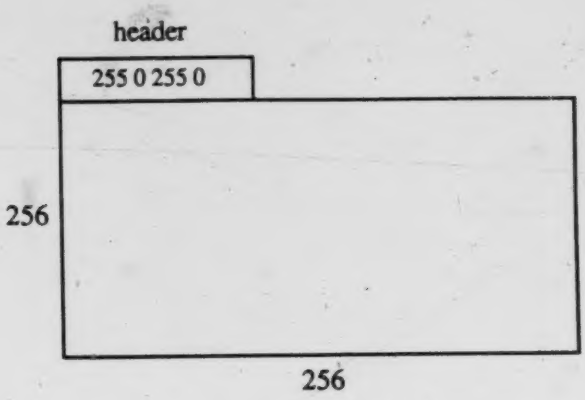
header
255 0 255 0
256
256

```
program Chop_into_Files;
{divides a multiple-image file into individual images}

const
    noofimages=6;{images in the input file}
   max=0;
   min=1;

var
   infile,outfile:text;
   thischar1,thischar2:char;
   data:real;
   i,j,counter:integer;
   maxmin:array[0..noofimages,0..1] of real;
   inputfilename,outputfilename:string[60];

function trim(x:real):real;

begin
   if (x>256) then trim:=256;
   if (x<0) then trim:=0
end;

begin
   writeln('enter the name of the input file');
   readln(inputfilename);
   writeln('enter the name of the output file');
   readln(outputfilename);
   reset(infile,inputfilename);
   writeln('opened ',inputfilename);
   counter:=0;
   while (not(eof) and (counter<noofimages)) do
   begin
      rewrite(outfile,outputfilename+chr(counter+70));
      for i:=1 to 128 do
      begin
         for j:=1 to 512 do
         begin
           read(infile,thischar1);
           read(infile,thischar2);
           write(outfile,thischar1);
           write(outfile,thischar2);
         end;
          writeln('file ',counter,'line ',i);
      end;
      counter:=counter+1;
      close(outfile);
   end;
   close(infile);

end.
```

Appendix F

Legendre Transform Program

This program is used to find the Legendre transform of a function, as described in Section 5.1.1. The functions pa and p generate the Legendre polynomials of degree 0 and 1. The function to be transformed is defined by the procedure makeshape. An example of the output of this program is given in Figure 5.1.1.3. The number of terms is set by the constant maxcoeffs, and the number of points in the function is set by the constant maxcount.

```
program legtrans;
{ Performs a Legendre transform }

uses
   memtypes,quickdraw,sane;
const
    maxcount=300;{ no. of points in the function }
    maxcoeffs=12; { no. of terms in the Legendre expansion used }

{$I spherical/ian:legendre_funcs}
{ pa(x,m,n) and p(x,n) }

var
   pic:grafport;
   myrect:rect;
   oldx,oldy,newx,newy,counter,counter2:integer;
   dummy:extended;
   coeffs:array[0..1,0 .. maxcoeffs] of extended;
   shape,remains:array[0..maxcount] of extended;
   scale,angle:extended;


procedure makeshape;
{ definition of function to be transformed}

var
   i:integer;
   total:extended;

begin
   total:=0;
   scale:=0;
   for i:=0 to maxcount do
   begin
      if i<100 then shape[i]:=-0.8;
      if i<50 then shape[i]:=1;
      if i>100 then shape[i]:=0;
      if i>200 then shape[i]:=1;
      if i>250 then shape[i]:=-0.8;
      shape[i]:=shape[i]*exp(-1*i*4/maxcount);
     total:=total+shape[i];
     if shape[i]>scale then scale:=shape[i];
   end;
   for i:=0 to maxcount do shape[i]:=shape[i]*total/maxcount;
   scale:=scale*total/maxcount;
end;
```

```
function sumsofar(x,y:integer):extended;

var
  i:integer;
  dummy:extended;

begin
  dummy:=0;
  for i:=0 to y do
  begin
    dummy:=dummy+coeffs[0,i]*pa(x*pi/maxcount,i,0);
  end;
  sumsofar:=dummy;
end;

procedure drawshape;

begin
    for counter:=0 to maxcount do
   begin
      if counter=0 then
      begin
        oldx:=100;
        oldy:=200-trunc(50*shape[counter]/scale)
      end;
      moveto(oldx,oldy);
      newx:=100+counter;
      newy:=200-trunc(50*shape[counter]/scale);
      lineto(newx,newy);
      oldx:=newx;
      oldy:=newy;
   end;
end;

procedure setup;

begin
      initgraf(@theport);
      setrect(myrect,60,20,400,300);
      openport(@pic);
      penpat(white);
      paintrect(myrect);
      penpat(black);
end;
```

```
begin

  setup;
  makeshape;
  remains:=shape;
  for counter2:=0 to maxcoeffs do
  begin
  dummy:=0;
  if counter2=0 then drawshape;
  for counter:=0 to trunc(maxcount) do
  begin
    angle:=counter*pi/maxcount;
    dummy:=dummy+remains[counter]*pa(angle,counter2,0)*sin(angle);
  end;
  coeffs[0,counter2]:=(dummy*pi*(2*counter2+1))/(2*maxcount);
  writeln(coeffs[0,counter2]);
  coeffs[1,counter2]:=0;
  if (counter2=maxcoeffs) then
  for counter:=0 to maxcount do
  begin
    if counter=0 then
    begin
      oldx:=100;
      oldy:=200-trunc(50*sumsofar(counter,counter2)/scale)
    end;
    moveto(oldx,oldy);
    newx:=100+counter;
    newy:=200-trunc(50*sumsofar(counter,counter2)/scale);
    lineto(newx,newy);
    oldx:=newx;
    oldy:=newy;
  end;
  end;
  readln;
  closeport(@pic);
end.
```

```
function pa(x:extended;m,n:integer):extended;
```

{ calculates the Legendre function $P_m^n(\cos x)$ }

```
var s,c:extended;

begin
s:=sin(x);
c:=cos(x);
if m < 13 then
 case m of
  0 :
   case n of
    0 : pa := 1;
    1 : pa := 0;
   end;
  1 :
   case n of
    0 : pa := c;
    1 : pa := s
   end;
  2 :
   case n of
    0 : pa := (3 * xpwri(c, 2) - 1) / 2;
    1 : pa := 3 * s * c;
    2 : pa := 3 * s * s
   end;
  3 :
   case n of
    0 : pa := (5 * xpwri(c, 3) - 3 * c) / 2;
    1 : pa := 1.5 * s * (5 * c * c - 1);
    2 : pa := 15 * s * s * c;
    3 : pa := 15 * s * s * s
   end;
  4 :
   case n of
    0 : pa := (35 * xpwri(c, 4) - 30 * xpwri(c, 2) + 3) / 8;
    1 : pa := 2.5 * s * (7 * xpwri(c, 3) - 3 * c);
    2 : pa := 7.5 * s * s * (7 * c * c - 1)
   end;
  5 :
   case n of
    0 : pa := (63 * xpwri(c, 5) - 70 * xpwri(c, 3) + 15 * c) / 8;
    1 : pa := 1.875 * s * (21 * xpwri(c, 4) - 14 * c * c + 1)
   end;
  6 :
   case n of
    0 : pa := (231 * xpwri(c, 6) - 315 * xpwri(c, 4) + 105 * xpwri(c, 2) - 5) / 16;
    1 : pa := 2.625 * s * (33 * xpwri(c, 5) - 30 * xpwri(c, 3) + 5 * c)
   end;
 7 :
  case n of
   0 : pa := (429 * xpwri(c, 7) - 693 * xpwri(c, 5)
                  + 315 * xpwri(c, 3) - 35 * c) / 16;
   1 : pa := s * (429 * 7 * xpwri(c, 6) - 693 * 5 * xpwri(c, 4)
                 + 315 * 3 * xpwri(c, 2) - 35) / 16;
  end;
 8 :
  case n of
   0 : pa := (6435 * xpwri(c, 8) - 12012 * xpwri(c, 6) + 6930 * xpwri(c, 4)
            - 1260 * xpwri(c, 2) + 35) / 128;
   1 : pa := s * (6435 * 8 * xpwri(c, 7) - 12012 * 6 * xpwri(c, 5)
            + 6930 * 4 * xpwri(c, 3) - 1260 * 2 * c) / 128;
  end;
 9 :
  case n of
   0 : pa := (12155 * xpwri(c, 9) - 25740 * xpwri(c, 7) + 18018 * xpwri(c, 5)
            - 4620 * xpwri(c, 3) + 315 * c) / 128;
   1 : pa := s * (12155 * 9 * xpwri(c, 8) - 25740 * 7 * xpwri(c, 6)
            + 18018 * 5 * xpwri(c, 4) - 4620 * 3 * xpwri(c, 2) + 315) / 128;
  end;
 10 :
  case n of
   0 :  pa := (46189 * xpwri(c, 10) - 109395 * xpwri(c, 8) + 90090 * xpwri(c, 6)
            - 30030 * xpwri(c, 4) + 3465 * xpwri(c, 2) - 63) / 256;
   1 :  pa := s * (46189 * 10 * xpwri(c, 9) - 109395 * 8 * xpwri(c, 7)
            + 90090 * 6 * xpwri(c, 5) - 30030 * 4 * xpwri(c, 3)
            + 3465 * 2 * c) / 256;
  end;
 11 :
  case n of
   0 :  pa := (88179 * xpwri(c, 11) - 230945 * xpwri(c, 9) + 218790 * xpwri(c, 7)
            - 90090 * xpwri(c, 5) + 15015 * xpwri(c, 3) - 693 * c) / 256;
   1 :  pa := s * (88179 * 11 * xpwri(c, 10) - 230945 * 9 * xpwri(c, 8)
            + 218790 * 7 * xpwri(c, 6) - 90090 * 5 * xpwri(c, 4)
            + 15015 * 3 * xpwri(c, 2) - 693) / 256;
  end;
 12 :
  case n of
   0 :  pa := (676039 * xpwri(c, 12) - 1939938 * xpwri(c, 10)
            + 2078505 * xpwri(c, 8) - 1021020 * xpwri(c, 6)
            + 225225 * xpwri(c, 4)
            - 18018 * xpwri(c, 2) + 231) / 1024;
   1 :  pa := s * (676039 * 12 * xpwri(c, 11) - 1939938 * 10 * xpwri(c, 9)
            + 2078505 * 8 * xpwri(c, 7) - 1021020 * 6 * xpwri(c, 5)
            + 225225 * 4 * xpwri(c, 3) - 18018 * 2 * c) / 1024;
  end;
 end
else
 pa := ((2 * m - 1) * c * pa(x, m - 1, n) - (m + n - 1) * pa(x, m - 2, n)) / (m - n);
end;
```

```
function p (x : extended;n : integer) : extended;
{ calculate the function $P_m^0$(cos x) }
 begin
   p := pa(x, n, 0)
 end;
```

Appendix G

CROSS CANCER INSTITUTE
NORTHERN ALBERTA CANCER PROGRAM
ALBERTA CANCER BOARD

Consent Form for Normal Healthy Volunteers to Be Examined by Nuclear Magnetic Resonance Spectroscopy

Consent Form A - Normal Healthy Volunteers

I understand that in order to develop and perfect the application of Nuclear Magnetic Resonance (NMR) to the solution in medical diagnosis, it is necessary to carry out development work while using normal healthy volunteers as subjects. It has also been explained to me that, in addition to the development of the NMR technique, experimental clinical trials require normal healthy volunteers as control subjects in order to validate the findings on patients with a particular disease. I understand that I am being invited to act as a normal control subject for these purposes.

The NMR technique to be used for this study is called Nuclear Magnetic Resonance (NMR) Spectroscopy. This test involves placing the body within a magnetic field produced by a large electrical magnet. Radiofrequency waves are then produced and passed through the specific tissues to be examined. These waves are detected by small antennae located near the surface of the body. Changes in the radiofrequency waves can be measured. The alterations of the waves will depend upon the chemical composition of the body tissue. As a result, small amounts of various tissue components can be determined. This information may be helpful in advancing the understanding of cancer cells.

In this study, the human breast will be evaluated by NMR spectroscopy. Women with breast cancer will be studied as well as women without breast cancer, such as myself. A comparison of the results will be made on completion of the study.

My participation will involve the following steps for me:

1. Arrival at the NMR Suite at the arranged time
2. Interview with the research nurse just prior to the NMR examination
3. Measurement of breast dimensions by the research nurse
4. Positioning within the NMR machine
5. Completion of the NMR scan

I have read and understand the Patient Information Booklet which outlines this process in more detail.

I understand that the completion of these steps will take up to 1 1/2 hours of my time.

I understand that there are no known harmful effects of this technique when operated at magnetic field strengths that are within the limits set by federal regulation. I understand that the examination will be entirely non-invasive and painless. I have been warned to keep my eyes closed during the laser positioning part of the procedure and I agree to do so. Operating the NMR machine may be associated with a thumping noise and some people have experienced anxiety being in a confined space.

The dangers presented by metal objects when exposed to large magnetic fields have been made clear to me, and I can categorically state that:

Patient's Initials ____________

Consent Form for Normal Healthy Volunteers to Be Examined by Nuclear Magnetic Resonance Spectroscopy

(Please answer True or False, T/F)

_____ I will remove my hearing aid and false teeth, if I wear either.

_____ I do not wear a cardiac pacemaker, implanted neurostimulator, or implanted drug delivery system.

_____ I have never undergone a cardiac valve replacement.

_____ I have never had an operation on my head and can therefore exclude the possibility of metal clips adjacent to or within my brain.

_____ I have never had an operation on my chest and can therefore exclude the possibility of metal clips attached to my vascular system.

_____ I have never had any form of vascular surgery and can therefore exclude the possibility of metal clips attached to my vascular system.

_____ I have never had a bone fracture and can therefore exclude the possibility of metal pins and screws supporting my skeletal system.

_____ I have never undergone a joint replacement.

_____ I have never been injured by a metallic foreign objective which was not subsequently removed.

_____ I have never worked as a welder, lathe operator or sheet metal workers, or in a similar trade.

_____ I am not wearing an IUD contraceptive device.

_____ There is no possibility that I am pregnant.

It has been made clear to me that the information obtained while I am acting as a normal control subject will be of no value to me personally or to a physician treating any previously diagnosed condition of mine. Nevertheless, I have been assured that all information obtained while I am acting as a normal control subject will be kept confidential. I understand that I am free to withdraw from this study at any time.

The principal investigators in this study are Dr. D. S. Ernst, Dr. A.H.G. Paterson, Dr. S. McEwan and Ms. Carla Danbrook, research nurse. The information regarding this study has been explained to me. I have been given the opportunity to ask questions and the questions I have asked have been answered to my satisfaction. Should further questions or concerns arise in the future, I can discuss them with one of the investigators (Phone Number 492-8771)

Patient's Initials __________

Consent Form for Normal Healthy Volunteers to be Examined by Nuclear Magnetic Resonance Spectroscopy

In acknowledgement of the preceding statements, regarding participation in this project, and under no duress or compulsion, I hereby volunteer freely and willingly to undergo an NMR examination.

Consent to Participate in this Study:

Name: ______________________

Signature: ______________________

Date: ______________________

Witness: ______________________

Physician: ______________________

Apendix H

```
program multi_coil_field_from_sph_harms;

{ This programme calculates the field from an array of circular     }
{ coils coaxial with the y axis. The spherical harmonic series      }
{ expansion for the magnetic field is used. The data is then        }
{ stored in a file called sph_harm_field_data.                      }

uses memtypes,sane;

const
   no_of_terms_used=16;                   {series truncation parameters}
   terms_to_average=4;
   give_details=true;                                  {debugging aid}
   lowerlimit=0.6;                          {transformation limits as}
   upperlimit=1.4;                     {fraction of coil dist. from origin}
   pi=3.1415926535;
   maxy=21;                                {points in x and y over which}
   maxx=21;                                   {to calculate the field}
   nloops=1;                               {number of circular coils}

var
   r_requested,theta_requested,f_requested,alpha_requested:extended;
   r,theta,f,alpha:extended;
   i:extended;
   br,btheta,btot,bacc:extended;
   x,y:extended;
   j:integer;
   transformed_r,transformed_theta,transformed_f,transformed_alpha:extended;
   transformed:boolean;
   counter,counter2,counter3:integer;
   outfile:text;
   loopars:array[1..2,1..nloops] of extended;{these are the coil parameters}

   { loopars[1,n] is fn  and loopars[2,n] is αn }

{$I spherical/ian:legendre_funcs}
          {function pa(x:extended;m,n:integer):extended;}
          {function p (x : extended;n : integer) : extended;}
{$I spherical/ian:transform_if_nec}
          {procedure transform_if_necessary;}

 procedure calculate_br_and_btheta( r,theta,alpha,f,i : extended);
 {this is the implementation of equation (5-27)}

 var
   n : integer;
   brd, brdt,btd,btdt : extended;
   bx,by:extended;
```

```
begin

 brd := 0;brdt:=0;
 btd:=0;btdt:=0;

 for n := 0 to no_of_terms_used do
  begin
   if r<=f then
    begin
     if r=0 then r:=0.01;
     brd := brd - 0.0000001 * 2 * i*pi
           * ((cos(alpha) * p(alpha, n+1)- p(alpha, n))
           * (n+1) * xpwri(r, n) * p(theta, n+1))
           / (xpwri(f, n+1));
     btd := btd + 0.0000001 * 2 * i*pi*
           (
            {((p(alpha,n)-p(alpha,n+2)))

            + }(cos(alpha) * p(alpha, n+1)- p(alpha, n))
              * xpwri(r, n+1)/ xpwri(f, n+1)
            )
           * pa(theta, n+1, 1);
    end
   else
    begin
     brd := brd + 0.0000001 * 2 * i*pi
           * ((cos(alpha)*p(alpha, n)- p(alpha, n+1))
           * (n+1) * xpwri(f, n+1) * p(theta, n))
           / (xpwri(r, n+2));
     btd := btd + 0.0000001 * 2 * i*pi
           * ((cos(alpha) * p(alpha, n)- p(alpha, n+1))
           * xpwri(f, n+1) * pa(theta, n, 1))
           / (xpwri(r, n+2));
    end;

   {average the cumulative sum}
  if n > no_of_terms_used - terms_to_average then
   begin
    brdt:=brdt+brd;
    btdt:=btdt+btd
   end;
 end;
 br:=brdt/terms_to_average;
 btheta:=btdt/terms_to_average;
 if r<=f then btheta:=btheta/r;
 by:=br*cos(theta)-btheta*sin(theta);
 bx:=br*sin(theta)+btheta*cos(theta);
  {writeln('by:=',100000000*by:1:4,' bx=',100000000*bx:1:4);}
```

```
{transformation of the field back to the original coordinates}
if transformed then
begin
   by:=br*cos(theta)-btheta*sin(theta);
   bx:=br*sin(theta)+btheta*cos(theta);
   br:=by*cos(theta_requested)+bx*sin(theta_requested);
   btheta:=bx*cos(theta_requested)-by*sin(theta_requested);
   if ((abs(theta_requested)<0.1) or (abs(theta_requested)>3.04)) then
   begin
      btheta:=0;
    end;
 end;
btot:=sqrt(sqr(num2extended(br))+sqr(num2extended(btheta)));
{if give_details then
     begin
         write('br is ', 100000000*br: 1 : 6);
         writeln('  bt is ', 100000000*btheta: 1 : 6)
     end;}

end;


begin
   {coil parameters}
   loopars[1,1]:=0.0703;
   loopars[2,1]:=1.14;
   {loopars[1,2]:=0.0527;
   loopars[2,2]:=1.48;
   loopars[1,3]:=0.0433;
   loopars[2,3]:=2.35;}
   i:=1;

   {prepare the data file}
   rewrite(outfile,'spherical/ian:sph_harm_field_data');
   writeln(outfile);
   writeln(outfile);

 {outer loop for y direction}
 for counter:=0 to maxy do
 begin
   writeln(counter);

    {inner loop for x direction}
   for counter2:=0 to maxx do
   begin
       {make positions at which to calculate the field}
     y:=0.14*counter/maxy-0.07;
     x:=0.14*counter2/maxx-0.07;
      if counter2=0 then writeln('y=',y);
      if y=0 then theta_requested:=3.1416/2
      else theta_requested:=arctan(x/y);
      if ((x>=0) and (y<0)) then
         theta_requested:=theta_requested+pi;
      if ((x<0) and (y<0)) then
         theta_requested:=theta_requested-pi;
       writeln('      x=',x,' theta=',theta_requested);
      r_requested:=sqrt(sqr(x)+sqr(y));
      bacc:=0;

        {this is the coils loop}
      for counter3:=1 to nloops do
      begin
         f_requested:=loopars[1,counter3];
         alpha_requested:=loopars[2,counter3];
         transform_if_necessary;
         if not(transformed) then
         begin
            r:=r_requested;
            theta:=theta_requested;
            alpha:=alpha_requested;
            f:=f_requested
         end
         else
         begin
            r:=transformed_r;
            theta:=transformed_theta;
            alpha:=transformed_alpha;
            f:=transformed_f;
         end;
         calculate_br_and_btheta(r,theta,alpha,f,i);
         bacc:=bacc+btot;
      end;

        {now to write the data}
      if counter2<maxx then write(outfile,bacc*1000000:2:1,chr(9))
      else write(outfile,bacc*1000000:2:1);
   end;
   writeln(outfile);
   end;
   close(outfile);
   readln;
end.
```